RESONANT SUBSTRUCTURE IN $\overline{K}\pi\pi\pi$ DECAYS OF D MESONS

Thesis by

Don Frederic DeJongh

In Partial Fulfillment of the Requirements

for the Degree of

Doctor of Philosophy

California Institute of Technology

Pasadena, California

1990

(Submitted May 16, 1990)

Abstract.

We determine the resonant substructure of $D \to \overline{K}\pi\pi\pi$ decays using a five-dimensional maximum likelihood technique to extract the relative fractions and phases of the amplitudes contributing to the $K^-\pi^+\pi^+\pi^-$, $\overline{K}^0\pi^+\pi^+\pi^-$, $K^-\pi^+\pi^+\pi^0$ and $\overline{K}^0\pi^+\pi^-\pi^0$ final states. We find that two-body decay modes account for about 75% of these decays. We obtain branching ratios for $D \to \overline{K}a_1$, $D \to \overline{K}^*\rho$, $D \to \overline{K}_1(1270)\pi$, $D \to \overline{K}_1(1400)\pi$ and $D^0 \to \overline{K}^0\omega$ decay modes, as well as several three and four-body decay modes. In the case of $D \to \overline{K}a_1$ and $D \to \overline{K}^*\rho$, we obtain the branching ratios for all three possible isospin combinations, enabling us to extract the isospin 1/2 and 3/2 amplitudes. This allows us to eliminate the ambiguity due to phase shifts between the isospin amplitudes when comparing our results with theoretical models. We find that the isospin 3/2 amplitudes are suppressed relative to the isospin 1/2 amplitudes, confirming that an understanding of the lifetime difference of the D^0 and D^+ depends on an understanding of two-body hadronic decays.

For the $D \to \overline{K}^*\rho$ decay modes, we obtain detailed information on the polarization of the $\overline{K}^*$ and ρ. This enables us to obtain information on form-factors for $D \to \overline{K}^*$ and $D \to \rho$ transitions, within the context of the factorization hypothesis. Comparison of our results on $D \to \overline{K}^*\rho$ decays with recent results on semileptonic decays allows us to test the factorization hypothesis.

Acknowledgements.

The work in this thesis is made possible by the efforts and achievements of the many members of the Mark III Collaboration who built the detector, acquired the data, and developed the basic analysis techniques.

I am especially grateful to my advisor, David Hitlin, for providing guidance and support, while still encouraging a high level of independence.

The work on the $K^-\pi^+\pi^+\pi^-$ final state was done in collaboration with Allen Mincer. Tom Browder, Bill Lockman, Rafe Schindler and Bill Wisniewski also made many contributions.

I benefited from my collaboration with Janine Adler, Tim Bolton, Gregory Dubois, Gerald Eigen, Tim Freese, Peter Kim, Jon Labs, Chris Matthews, Bijan Nemati, Larry Parrish, Walter Toki, Steve Wasserbaech, Yanong Zhu, and many others.

Finally, I would like to thank my wife, Lynette Greenwood, and all the other members of my family for their love and support as I carried out this work.

Table of Contents.

Abstract. ii

Acknowledgements. iii

Table of Contents. iv

List of Tables. viii

List of Figures. x

1

Introduction. 1

1.1 The Lifetimes of the D Mesons. 2

1.2 Semileptonic Decays. 4

1.3 The Effective Weak Hamiltonian. 7

1.4 Two-Body Hadronic Decays. 11

1.5 An Overview of the Analysis of the $D \to \overline{K}\pi\pi\pi$ Final States. 20

1.6 Summary. 22

2

The Mark III Detector. 24

2.1 An Overview. 24

2.2 The Drift Chambers. 25

2.3 Time of Flight. 32

2.4 Shower Counters. 32

2.5 The Trigger. 35

3

Event Selection. 37

3.1 The Data Set. 37

3.2 Initial Event Selection. 38

3.3 The Recoil Mass Plot. 40

3.4 The Monte Carlo Simulation. 41

3.5 $D^0 \to K^-\pi^+\pi^+\pi^-$. 41

3.6 $D^+ \to \overline{K}^0\pi^+\pi^+\pi^-$. 43

3.7 $D^+ \to K^-\pi^+\pi^+\pi^0$. 45

3.8 $D^0 \to \overline{K}^0\pi^+\pi^-\pi^0$. 50

4

The Fitting Technique. 53

4.1 The Phase Space. 54
4.2 The Likelihood Function. 55
4.3 Finding the Maximum of the Likelihood. 57
4.4 The Normalization of the Fractions. 58
4.5 The Sum of a Subset of Amplitudes. 58
4.6 The Relative Efficiency. 59
4.7 Making Projections. 59
4.8 Notation. 59
4.9 Error Propagation. 60
4.10 The Amplitudes. 61
4.11 The Decision on Which Amplitudes to Include in the Fit. 70
4.12 General Discussion of Systematic Errors and Upper Limits. 71
4.13 Guidelines for Reproducing the Distributions in Phase Space. 74

5
$D^0 \to K^-\pi^+\pi^+\pi^-$. 75

6
$D^+ \to \overline{K}^0\pi^+\pi^+\pi^-$. 86

7
$D^+ \to K^-\pi^+\pi^+\pi^0$. 96

8
$D^0 \to \overline{K}^0\pi^+\pi^-\pi^0$. 104

9

Conclusions. 113

9.1 Isospin Decompositions. 113

9.2 Three and Four Body Decay Modes, and Upper Limits. 118

9.3 Form-factors. 120

9.4 Conclusions. 123

References 125

List of Tables.

1.1 Branching ratios for $\overline{K}\pi$, $\overline{K}\rho$, and $\overline{K}^*\pi$ decay modes. 3

1.2 Isospin decomposition for $D \to PP$ and $D \to PV$ modes. 4

1.3 Results from E691 on $D^+ \to \overline{K}^{*0}e^+\nu$. 7

1.4 Branching ratios for $\overline{K}\pi$, $\overline{K}\rho$, and $\overline{K}^*\pi$ decay modes. 17

1.5 D^0 decay modes proportional a single isospin amplitude. 19

1.6 Fractions of decay modes to the final states. 21

1.7 Features of hadronic decays of D^0 and D^+ mesons. 22

3.1 D^0 decay modes in the Monte Carlo model. 42

3.2 D^+ decay modes in Monte Carlo model. 42

4.1 Lorentz invariant amplitudes. 62

5.1 Results for $D^0 \to K^-\pi^+\pi^+\pi^-$. 80

5.2 Upper limits for $D^0 \to K^-\pi^+\pi^+\pi^-$. 81

5.3 $K^-\pi^+\pi^+\pi^-$ decay chains. 82

5.4 Fractions of $D^0 \to K^-\pi^+\pi^+\pi^-$ as observed by different experiments. ... 82

5.5 Systematic Uncertainties on the fractions. 85

6.1 Results for $D^+ \to \overline{K}^0\pi^+\pi^+\pi^-$. 93

6.2 $\overline{K}^0\pi^+\pi^+\pi^-$ decay chains. 93

6.3 Limits for $D^+ \to \overline{K}^0\pi^+\pi^+\pi^-$. 94

6.4 Systematic uncertainties for $\overline{K}^0\pi^+\pi^+\pi^-$. 95

7.1 Results for $D^+ \to K^-\pi^+\pi^+\pi^0$. 100

7.2 Limits for $D^+ \to K^-\pi^+\pi^+\pi^0$. 101

7.3 $K^-\pi^+\pi^+\pi^0$ decay chains. 102

7.4 Systematic uncertainties for $K^-\pi^+\pi^+\pi^0$. 103

8.1 Results for $D^0 \to \overline{K}^0\pi^+\pi^-\pi^0$. 110

9.1 $\overline{K}a_1$ Branching Ratios (%). 114

9.2 $\overline{K}a_1$ Branching Ratios (%), with the constraint $\cos\delta < 1$. 114

9.3 $\overline{K}^*\rho$ Branching Ratios (%). 115

9.4 Limits on P-wave $\overline{K}^*\rho$ Branching Ratios (%). 116

9.5 $\overline{K}_1(1270)\pi$ Branching Ratios (%). 117

9.6 $\overline{K}_1(1400)\pi$ Branching Ratios (%). 117

9.7 Isospin Decompositions. 118

9.8 Branching Ratios for Three-body Decay Modes. 118

9.9 Branching Ratios for Four-body Decay Modes. 119

9.10 Upper Limits. 119

9.11 Form-factors in the BSW model. 120

9.12 Branching ratios (%) in BSW model, using form-factors from E691. 120

9.13 Partial wave breakdown for $\overline{K}^*\rho$ decays in BSW model. 122

List of Figures.

1.1 Effective Hamiltonian. 8

1.2 One-loop gluon corrections. 8

1.3 External W emission diagram. 12

1.4 Internal W emission diagram. 12

1.5 W annihilation and W exchange diagrams. 12

1.6 Final state interactions. 13

2.1 Axial view of the Mark III detector. 26

2.2 Side view of the Mark III detector. 26

2.3 Layer 1 of the Drift Chambers. 28

2.4 Distribution of layer 1 time sum. 29

2.5 A cell in layer 2 of the drift chamber. 30

2.6 Layer 2 pulse height versus momentum. 30

2.7 A cell in the outer layers of the drift chamber. 31

2.8 Resolution of left–right ambiguity. 31

2.9 The time–of–flight system. 33

2.10 Time–of–flight versus momentum. 33

2.11 The barrel shower counter. 34

2.12 The endcap shower counter. 34

2.13 Trigger track finding and logic. 36

3.1 Signal for $D^0 \to K^-\pi^+\pi^+\pi^-$. 44

3.2 Signal for $D^+ \to \overline{K}^0\pi^+\pi^+\pi^-$. 44

3.3 Signal for $D^+ \to K^-\pi^+\pi^+\pi^0$, without isolated shower requirement. 46

3.4 Signal for $D^+ \to K^-\pi^+\pi^+\pi^0$, with isolated shower requirement. 46

3.5 $K^-\pi^+\pi^+\pi^0$ Recoil Mass, Monte Carlo background. 47

3.6 Signal for $D^0 \to \overline{K}^0\pi^+\pi^-\pi^0$. 51

3.7 $\overline{K}^0\pi^+\pi^-\pi^0$ Recoil Mass, Monte Carlo background. 51

4.1 a_1 width versus mass. 69

4.2 $K_1(1400)$ width versus mass. 69

5.1 Signal for $D^0 \to K^-\pi^+\pi^+\pi^-$. 76

5.2 Projections of $\mathcal{F}_B$ onto events outside of the signal region. 77

5.3 Projections of $\mathcal{F}$ onto events in the signal region. 78

5.4 Illustration of $K^-a_1^+$ amplitude. 79

5.5 Illustration of the transverse polarization of the $\overline{K}^{*0}\rho^0$ amplitude. 79

5.6 χ^2 from the fit to the data. 84

5.7 χ^2 from the fit to the Monte Carlo. 84

6.1 Signal for $D^+ \to \overline{K}^0\pi^+\pi^+\pi^-$. 87

6.2 Scatter plots for data events. 88

6.3 Scatter plots for mc events. 88

6.4 Illustration of $\overline{K}^0a_1^+$ amplitude. 89

6.5 Illustration of $\overline{K}_1(1400)^0\pi^+$ amplitude. 89

6.6 Scatter plots for data events. 90

6.7 Scatter plots for mc events. 90

6.8 Projections of $\mathcal{F}_B$ onto sideband events. 91

6.9 Projections of $\mathcal{F}_S$ onto events in the signal region. 92

6.10 χ^2 from the fit to the data. 94

7.1 Signal for $D^+ \to K^-\pi^+\pi^+\pi^0$. 97

7.2 Projections of $\mathcal{F}_B$ onto sideband events. 98

7.3 Projections of $\mathcal{F}_S$ onto events in the signal region. 99

7.4 Illustration of $\overline{K}^{*0}\rho^+$ amplitude. 100

7.5 χ^2 for fits to data. 101

8.1 Signal for $D^0 \to \overline{K}^0\pi^+\pi^-\pi^0$. 105

8.2 Scatter-plot of $(K^-\pi^+)_1$ mass vs. $(\pi^+\pi^-)_{\text{high}}$ mass. 107

8.3 Projections of $\mathcal{F}_B$ onto sideband events. 108

8.4 Projections of $\mathcal{F}_S$ onto events in the signal region. 109

8.5 Efficiency as a function of $\overline{K}^0\omega$ amplitude. 110

8.6 χ^2 for fits to data. 111

1
Introduction.

The fundamental parameters of the Standard Model apply to charm decays at the bare quark level, while experiments detect the final state hadrons and leptons. To extract the values of these parameters, it is necessary to understand the strong interaction effects, including short distance corrections to the weak Hamiltonian and long distance hadronization. A great deal of experimental information on semileptonic and hadronic D decays has been accumulated. Measurements are reaching a high level of detail and sophistication and are challenging theoretical models on several fronts.

Measurements of hadronic D decays have produced information on a large number of exclusive decay modes which nearly account for the total hadronic width.[1,2] Most of these decay modes are to two, three, and four-body final states. Detailed studies of three-body final states[3–6] have shown these final states are dominated by contributions from two-body decay modes involving broad intermediate resonances. In this thesis, we obtain the first detailed results on the resonant substructure of the $D \to \overline{K}\pi\pi\pi$ final states.

1.1 The Lifetimes of the D Mesons.

The lifetimes of the D^0, D^+, and D_s have been measured very precisely:[7]

$$\begin{aligned} \tau(D^0) &= (4.28 \pm 0.11) \times 10^{-13}\ sec \\ \tau(D^+) &= (10.69^{+0.34}_{-0.32}) \times 10^{-13}\ sec \\ \tau(D_s^+) &= (4.36^{+0.38}_{-0.32}) \times 10^{-13}\ sec \end{aligned} \tag{1.1}$$

In the simplest model of charm decay, the charm quark decays as a free quark, unaffected by the accompanying light quark which is referred to as the "spectator" quark. The lifetimes of the charmed mesons are therefore expected to be equal. However, $\tau(D^+)$ is about 2.5 times $\tau(D^0)$ and $\tau(D_s)$. The spectator quark therefore has a large effect on the decay of the charm quark, and this simplest spectator model fails.

The inclusive semileptonic branching ratios of the charmed mesons have all been measured:[7]

$$\begin{aligned} B(D^0 \to e^+X) &= (7.7 \pm 1.1)\% \\ B(D^+ \to e^+X) &= (19.2^{+2.3}_{-1.6})\% \\ B(D_s^+ \to e^+X) &= (5.0 \pm 5.0 \pm 2.0)\%^{[8]} \end{aligned} \tag{1.2}$$

Using the measured lifetimes, the semileptonic widths of the three charmed mesons are consistent with being equal. Subtracting the measured semileptonic widths from the total widths for the D^0 and D^+, we obtain the ratio of the hadronic widths:

$$\frac{\Gamma_H(D^0)}{\Gamma_H(D^+)} \cong 3.5 \tag{1.3}$$

Thus, the solution to the lifetime problem will be found in an understanding of the hadronic decays.

The difference in the hadronic width of the D^0 and D^+ is already reflected in branching ratios of Cabibbo-allowed decays to two pseudoscalar mesons (PP) and

Table 1.1 Branching ratios for $\overline{K}\pi$, $\overline{K}\rho$, and $\overline{K}^*\pi$ decay modes.

Mode	Branching Ratio (%)	Ref.
$K^-\pi^+$	$4.2 \pm 0.4 \pm 0.4$	10
$\overline{K}^0\pi^0$	$1.9 \pm 0.4 \pm 0.2$	11
$\overline{K}^0\pi^+$	$3.2 \pm 0.5 \pm 0.2$	10
$K^-\rho^+$	$10.8 \pm 0.4 \pm 1.7$	5
$\overline{K}^0\rho^0$	$0.8 \pm 0.1 \pm 0.5$	5
$\overline{K}^0\rho^+$	$6.9 \pm 0.8 \pm 2.3$	5
$K^{*-}\pi^+$	$5.3 \pm 0.4 \pm 1.0$	5
$\overline{K}^{*0}\pi^0$	$2.6 \pm 0.3 \pm 0.7$	5
$\overline{K}^{*0}\pi^+$	$5.9 \pm 1.9 \pm 2.5$	5

to a pseudoscalar and a vector meson (PV). This can be seen by considering decays of the D to $\overline{K}\pi$, $\overline{K}\rho$, and $\overline{K}^*\pi$. The branching ratios for these modes are listed in Table 1.1. For these decays, one of the mesons has isospin 1/2 and the other isospin 1. All Cabibbo-allowed decays of the D^+ are of this type. The ratio of hadronic widths from these decay modes is:

$$\frac{\Gamma_H(D^0)}{\Gamma_H(D^+)} = 4.0 \pm 1.0 \tag{1.4}$$

in agreement with equation (1.3). Thus, it seems possible that an understanding of the lifetime difference will depend on an understanding of two-body decays. However, the decay modes in Table 1.1 account for only one third of the total of hadronic D decays. Since the $\overline{K}\pi\pi\pi$ final states account for another one third to one half of hadronic decays, an understanding of the decay modes to these final states is necessary to understand equation (1.4).

The amplitudes for decays for which one of the mesons has isospin 1/2 and the

Table 1.2 Isospin decomposition for $D \to PP$ and $D \to PV$ modes.

Mode	$\lvert A_{1/2}/A_{3/2}\rvert$	$\delta_{1/2} - \delta_{3/2}$
$\overline{K}\pi$	3.67 ± 0.27	$77° \pm 11°$
$\overline{K}\rho$	3.12 ± 0.4	$0° \pm 26°$
$\overline{K}^*\pi$	3.22 ± 0.97	$84° \pm 13°$

other isospin 1 can be written in terms of isospin 1/2 and 3/2 components:

$$\begin{aligned} A(D^+ \to |+1/2;+1>) &= \sqrt{3}A_{3/2}e^{i\delta_{3/2}} \\ A(D^0 \to |-1/2;+1>) &= \sqrt{\frac{1}{3}}\left(A_{3/2}e^{i\delta_{3/2}} + \sqrt{2}A_{1/2}e^{i\delta_{1/2}}\right) \\ A(D^0 \to |+1/2;\ \ 0>) &= \sqrt{\frac{1}{3}}\left(\sqrt{2}A_{3/2}e^{i\delta_{3/2}} - A_{1/2}e^{i\delta_{1/2}}\right) \end{aligned} \tag{1.5}$$

If all three isospin states of a decay mode are measured, $|A_{1/2}/A_{3/2}|$ and $\delta_{1/2} - \delta_{3/2}$ can be extracted for that mode. In the Mark III paper on resonant substructure in $\overline{K}\pi\pi$ decays of D mesons,[5] this was done for $D \to \overline{K}\pi$, $\overline{K}\rho$, and $\overline{K}^*\pi$, as shown in table 1.2. The ratios of isospin amplitudes for these modes are about 3.5, which reflects the ratio of the hadronic widths of the D^0 and D^+, and the isospin phase shifts can be sizeable.

1.2 Semileptonic Decays.

In the spectator model, we can naively estimate the semileptonic branching ratio by assuming the W from the charm quark decays equally to each of five possible final states: $\mu\nu_\mu$, $e\nu_e$, and three colors of $u\bar{d}$. We therefore expect $B(c \to e^+X) = 20\%$. The semileptonic branching ratio of the D^+ agrees with this simplest spectator model, while that of the D^0 and D_s are different. However, this simple expectation could be modified by the presence of strong interactions and large final state meson masses.

Since much of the formalism for semileptonic decays is also applied to hadronic decays, we introduce some of the formalism here.[12] The matrix element for a semileptonic decay factorizes into a hadronic part and a leptonic part:

$$A(D \to me\nu) = \frac{G_F}{\sqrt{2}} V_{cq} L^\mu H_\mu \tag{1.6}$$

where V_{cq} is the Kobayashi-Maskawa (K-M) matrix element, L^μ is the leptonic current

$$L^\mu = e\gamma^\mu(1-\gamma^5)\nu \tag{1.7}$$

and H_μ is the hadronic current

$$H_\mu = < m|J_\mu|D > . \tag{1.8}$$

The matrix element for the hadronic current is constructed from Lorentz invariant form factors and the four-vectors in the problem.[13-15] In the case in which m is a vector meson, we have, in the notation of M. Bauer, B. Stech and M Wirbel (Ref. 14):

$$\begin{aligned} < V|J_\mu|D > = & \frac{2}{M_D + M_V} V(q^2)\epsilon_{\mu\nu\rho\sigma}\varepsilon^{*\nu}P^\rho k^\sigma \\ & + i(M_D + M_V)A_1(q^2)\varepsilon^*_\mu \\ & - \frac{i}{M_D + M_V} A_2(q^2)(\varepsilon^* \cdot P)(P+k)_\mu \\ & - \frac{2iM_V}{q^2} A_3(q^2)(\varepsilon^* \cdot P)q_\mu \\ & + \frac{2iM_V}{q^2} A_0(q^2)(\varepsilon^* \cdot P)q_\mu \end{aligned} \tag{1.9}$$

where P is the four-momentum of the D, k is the four-momentum of the V, $q = P - k$, and $V(q^2)$, $A_1(q^2)$, $A_2(q^2)$, $A_3(q^2)$, and $A_0(q^2)$ are the form-factors, which obey the relations

$$A_3(0) = A_0(0) \tag{1.10}$$

and

$$A_3(q^2) = \frac{M_D + M_V}{2M_V} A_1(q^2) - \frac{M_D - M_V}{2M_V} A_2(q^2). \tag{1.11}$$

Generally, the terms proportional to $A_3(q^2)$ and $A_0(q^2)$ are neglected in the limit of small lepton masses, as they enter into the decay rate as coefficients of terms proportional to the squares of those masses.

In the case in which m is a pseudoscalar meson, we have:

$$\begin{aligned} < P|J_\mu|D > = & \left(P + k - \frac{M_D^2 - M_P^2}{q^2} q \right)_\mu F_1(q^2) \\ & + \frac{M_D^2 - M_P^2}{q^2} q_\mu F_0(q^2) \end{aligned} \tag{1.12}$$

The form-factors are obtained theoretically by calculating the overlap between meson wave-functions, in the quark model, at one value of q^2, such as $q^2 = 0$ or $q^2 = q^2_{max}$, and extrapolating to other values of q^2 using some assumed functional dependance, such as a pole-dominance function. For example,

$$V(q^2) = \frac{h_V}{1 - q^2/M^2_{D_s^*}} \tag{1.13}$$

where h_V is the overlap integral at $q^2 = 0$.

The predictions[13–15] for $D^0 \rightarrow K^- e^+ \nu$ agree with the measured branching ratio of $3.5 \pm 0.5\%$.[16,17] The models also predict that the width for $D \rightarrow \overline{K}^* e\nu$ should be greater than that for $D \rightarrow \overline{K} e\nu$, and that the ratio of longitudinal to transverse polarization should be about one. However, recent measurements[18,19] show that $B(D^+ \rightarrow \overline{K}^{*0} e^+ \nu) = 4.5 \pm 0.7 \pm 0.5\%$ and $\Gamma_L/\Gamma_T = 2.4^{+1.7}_{-0.9} \pm 0.2$. Taking into account the D lifetimes, the width for $D^+ \rightarrow \overline{K}^{*0} e^+ \nu$ is about half that for $D^0 \rightarrow K^- e^+ \nu$.

Table 1.3 Results from E691 on $D^+ \to \overline{K}^{*0} e^+ \nu$.

	E691[a]	ISGW[b]	BSW[c]	GS[d]
$A_1(0)$	$0.50 \pm 0.05 \pm 0.05$	0.97	0.88	0.73
$A_2(0)$	$0.00 \pm 0.25 \pm 0.10$	1.00	1.15	0.55
$V(0)$	$0.93 \pm 0.40 \pm 0.09$	1.35	1.23	1.47
Γ_L/Γ_T	1.8 ± 0.5	1.09	0.91	1.2

[a] Reference 20 [b] Reference 13
[c] Reference 14 [d] Reference 15

A more sophisticated fit has been performed by the E691 collaboration to extract the form-factors for $D^+ \to \overline{K}^{*0} e^+ \nu$.[20] The results, shown in Table 1.3, are very preliminary, and are different from the predictions.

The disagreement with the data on $D^+ \to \overline{K}^{*0} e^+ \nu$ is a serious blow to the models. N. Isgur has stated that if these experimental results are confirmed, they will kill the ISGW model.[12] These models are expected to be most reliable for $b \to c$ decays, where both the initial and final mesons contain heavy quarks and thus have similar wave-functions, making the overlap integrals easy to calculate. However, it is important to have models that are reliable for $b \to u$ decays, in order to extract the V_{bu} K-M matrix element. If the models are not correct for $c \to s$ decays, they may also not be correct for $b \to u$ decays.

1.3 The Effective Weak Hamiltonian.

Quantum Chromodynamics (QCD) has been used to improve on the naive spectator model.[21] The lowest order Hamiltonian, represented in Fig. 1.1a can be written

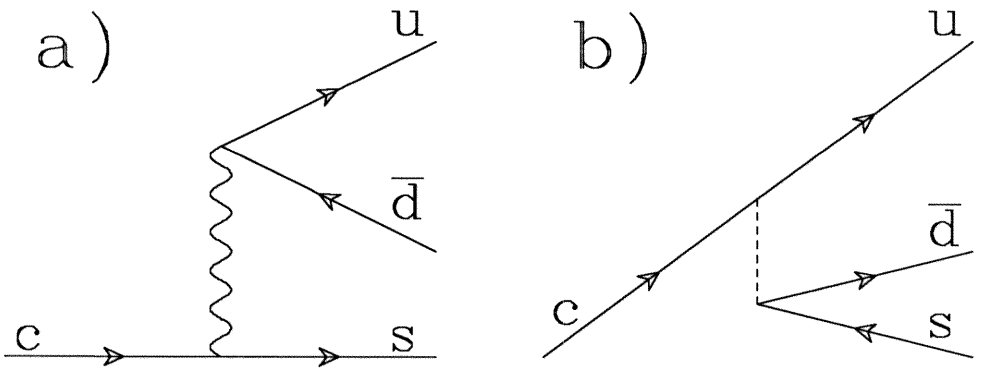

Figure 1.1 a) Effective charged current. b) Effective neutral current.

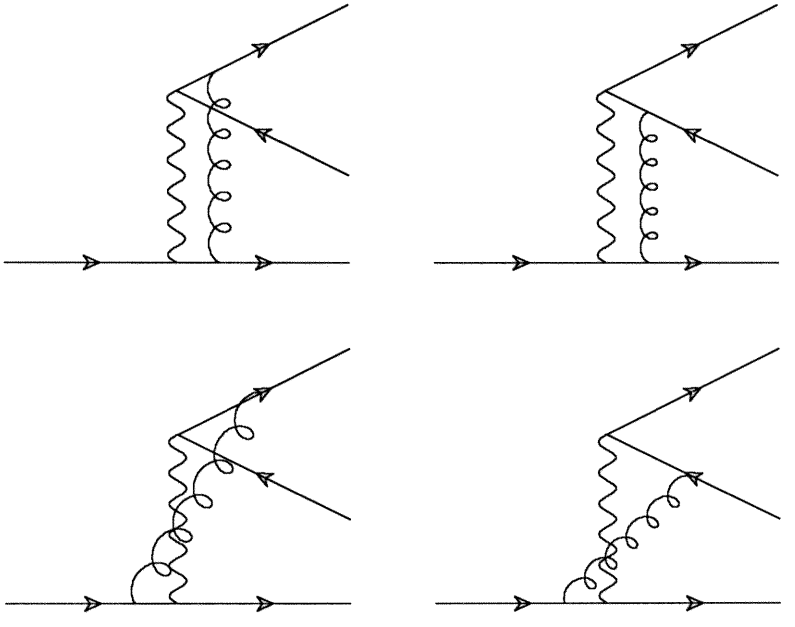

Figure 1.2 One-loop gluon corrections.

as

$$H^0 = \frac{G_F}{\sqrt{2}}(\overline{s}c)(\overline{u}d) \tag{1.14}$$

where

$$(\overline{q}_1 q_2) \equiv \overline{q}_1 \gamma^\mu (1-\gamma^5) q_2 V_{12} \tag{1.15}$$

and V_{12} is the K-M matrix element.

There are several order α_s gluon corrections that are absorbed into the renormalization of the physical masses and couplings. In addition there are four diagrams, shown in Fig. 1.2, in which the gluon connects fermions belonging to different vertices. New currents may therefore be introduced. The first order correction is:

$$H^1 = -\frac{G_F}{\sqrt{2}}\frac{3\alpha_s}{8\pi}\ln(\frac{M_W^2}{\mu^2})(\overline{s}\lambda^a c)(\overline{u}\lambda^a d) \tag{1.16}$$

Using the Fierz identity

$$[\gamma^\mu(1-\gamma^5)]_{\alpha\beta}[\gamma_\mu(1-\gamma^5)]_{\delta\epsilon} = -[\gamma^\mu(1-\gamma^5)]_{\alpha\epsilon}[\gamma_\mu(1-\gamma^5)]_{\delta\beta} \tag{1.17}$$

and the color algebra relation

$$\sum_{a=1}^{8} \lambda_{ij}^a \lambda_{kl}^a = -\frac{2}{3}\delta_{ij}\delta_{kl} + 2\delta_{il}\delta_{kj} \tag{1.18}$$

equation (1.16) can be rewritten:

$$(\overline{s}\lambda^a c)(\overline{u}\lambda^a d) = -\frac{2}{3}(\overline{s}c)(\overline{u}d) + 2(\overline{s}d)(\overline{u}c) \tag{1.19}$$

Therefore, the hard gluon exchanges not only modify the charged current, they induce an effective neutral current, as illustrated in Fig. 1.1b.

The Hamiltonian $H = H^0 + H^1$ is often written in terms of symmetric and

antisymmetric parts:

$$H = \frac{G_F}{\sqrt{2}}(c_+ O_+ + c_- O_-) \tag{1.20}$$

where

$$\begin{aligned} c_+ &= 1 + \frac{\alpha_s}{2\pi}\ln(\frac{M_W^2}{\mu^2}) \\ c_- &= 1 - \frac{\alpha_s}{\pi}\ln(\frac{M_W^2}{\mu^2}) \end{aligned} \tag{1.21}$$

and

$$O_\pm = \frac{1}{2}(\overline{s}c)(\overline{u}d) \pm \frac{1}{2}(\overline{s}d)(\overline{u}c) \tag{1.22}$$

Further QCD corrections have been made to c_+ and c_-. Renormalization group techniques have been used to sum corrections to all orders in perturbation theory in the leading log approximation. A calculation of the next-to-leading log terms in two-loop diagrams confirms that these corrections are small. Also, quark masses have been taken into account. At the scale $\mu = 1.5\,\mathrm{GeV}$ one obtains:

$$c_+ = 0.74 \qquad c_- = 1.8 \tag{1.23}$$

To estimate the QCD-corrected spectator model inclusive semileptonic branching ratio we rewrite the effective weak Hamiltonian in the form before the Fierz transformation:

$$H = \frac{G_F}{\sqrt{2}}\left[\frac{2c_+ + c_-}{3}(\overline{s}\delta_{ij}c)(\overline{u}\delta_{kl}d) + \frac{c_+ - c_-}{4}\ln(\frac{M_W^2}{\mu^2})(\overline{s}\lambda^a_{ij}c)(\overline{u}\lambda^a_{kl}d)\right] \tag{1.24}$$

where we have explicitly shown the color indices. This form has the advantage that the two terms have a different color structure, and their interference term is zero. To estimate the total hadronic width, we use the QCD corrected values for c_+ and c_-, and color factors for each term. To calculate the color factors, we sum over final

state colors and average over initial state colors. For the first term:

$$\frac{1}{3}\delta_{ij}\delta^{ij}\delta_{kl}\delta^{kl} = 3 \tag{1.25}$$

Using equation (1.18) to calculate the second term:

$$\frac{1}{3}\sum_{a,b}(\lambda_b)_{ij}(\lambda_a)^{ij}(\lambda^b)_{kl}(\lambda^a)^{kl} = \frac{32}{3}. \tag{1.26}$$

Squaring the coefficients of each term in equation (1.24) and multiplying by the color factors, we obtain

$$\Gamma_{Hadronic} = (2c_+^2 + c_-^2) \tag{1.27}$$

relative to the uncorrected semileptonic width

$$\Gamma_{Semileptonic} = 1. \tag{1.28}$$

So the semileptonic branching ratio is:

$$B(c \to sl^+\nu_l) = \frac{1}{2c_+^2 + c_-^2 + 2} = 16\%. \tag{1.29}$$

Estimates considering radiative gluon diagrams and using constituent quark masses lead to a slightly smaller branching ratio of 13 to 15%.

1.4 Two-Body Hadronic Decays.

Recent theoretical models for exclusive hadronic D decays have largely been limited to two-body decay modes.[22] With the assumption that hadronic D decays are dominated by two-body decay modes, these models indicate possible explanations for the charmed meson lifetimes.

For two-body decays of charmed mesons, there are two possible spectator diagrams, the external W emission diagram, as shown in Fig. 1.3, and the internal W

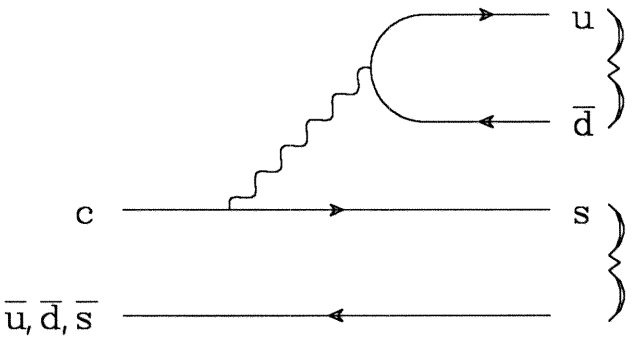

Figure 1.3 External W emission diagram.

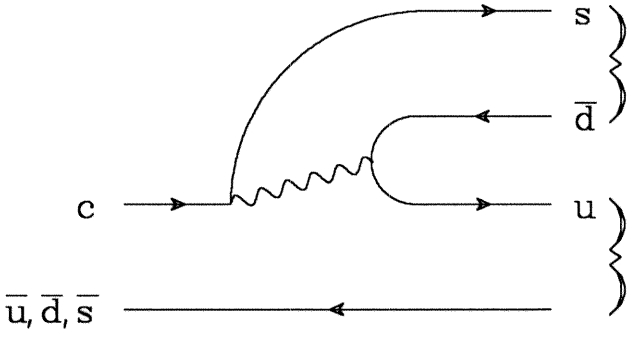

Figure 1.4 Internal W emission diagram.

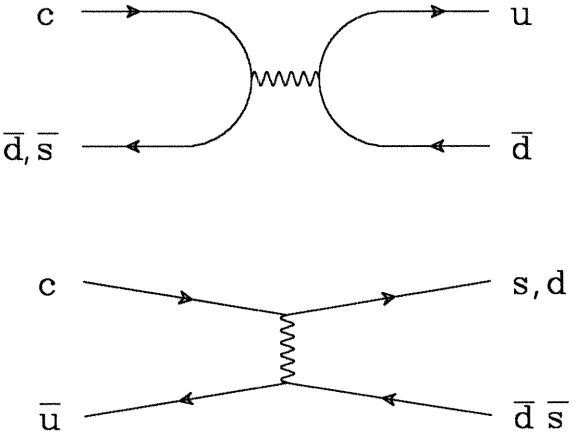

Figure 1.5 W annihilation and W exchange diagrams.

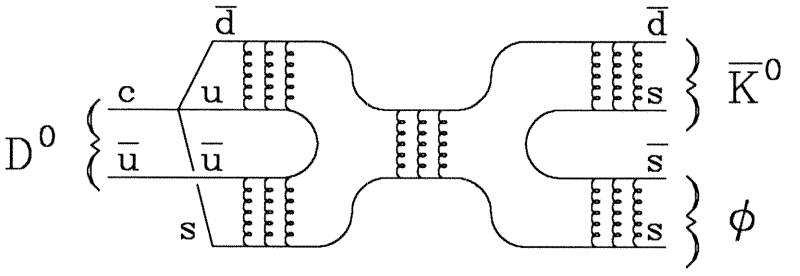

Figure 1.6 Final state interactions.

emission diagram, as shown in Fig. 1.4. In the case of Cabibbo-allowed decays of the D^+, there are two $\overline{d}$ quarks in the final state of each diagram; both diagrams therefor contribute to each decay mode. Thus, there is a possibility that these diagrams interfere destructively, decreasing the hadronic width, and increasing the lifetime. This would solve the lifetime problem, but an explanation would need to be found for why the semileptonic branching ratios are smaller than expected in the naive spectator model.

The W annihilation diagram for the D_s^+ and the D^+, and the W exchange diagram for the D^0 are shown in Fig. 1.5. Since the diagram for the D^+ is Cabibbo-suppressed, these diagrams increase the hadronic width and decrease the lifetimes of the D^0 and D_s, without affecting the D^+. Thus, this mechanism could also solve the lifetime problem, while yielding observed semileptonic branching ratios identical to those expected in the naive spectator model.

Establishing the magnitude of the W exchange and annihilation diagrams is

difficult. Most final states of the D^0 or D_s^+ can be obtained from both spectator and W exchange or W annihilation diagrams. The possibility of channel mixing further confuses the situation. The final state mesons from one decay mode may inelastically rescatter into a different final state. This process, called a final state interaction (FSI), is illustrated for the case of $D^0 \to \overline{K}^0\phi$ in Fig. 1.6. This decay mode can otherwise be produced only through the W exchange process.

The basic assumption of the model of Bauer, Stech, and Wirbel (BSW)[23] is that the short distance and long distance QCD contributions can be factorized. The short distance contributions are calculated perturbatively as described above to obtain the effective weak Hamiltonian. The long distance contributions are taken into account by taking the matrix element of the Hamiltonian between the initial charmed meson and two-body final states, using relativistic harmonic oscillator wave-functions for the mesons.

The Hamiltonian is rewritten, separating the charged and neutral current parts:

$$H = \frac{G_F}{\sqrt{2}}\left[c_1(\overline{s}c)(\overline{u}d) + c_2(\overline{s}d)(\overline{u}c)\right] \tag{1.30}$$

where

$$\begin{aligned} c_1 &= c_+ + c_- \\ c_2 &= c_+ - c_-. \end{aligned} \tag{1.31}$$

Applying this procedure to $D^0 \to K^{*-}\rho^+$ the matrix element is:

$$< K^{*-}\rho^+|H|D^0 >= \frac{G_F}{\sqrt{2}}a_1 < \rho^+|(\overline{u}d)|0 >< K^{*-}|(\overline{s}c)|D^0 > \tag{1.32}$$

where

$$a_1 = c_1 + \xi c_2 \tag{1.33}$$

and $\xi = 1/N_C$, where $N_C = 3$ is the number of colors. The first term in

equation (1.33) is from the effective charged current in Fig. 1.1a. The second term is a color-suppressed contribution from the effective neutral current in Fig. 1.1b. A Fierz transformation is applied to the neutral current matrix element, equation (1.19) and the resulting octet current is neglected. An annihilation term is also produced; it is ignored in the factorization approach because of the helicity suppression at the vertex with the two light quarks. In terms of an expansion in the parameter ξ,[24] the first term in equation (1.33) is of leading order in ξ, while the second term as well as the octet currents and FSI are of higher order in ξ, and thus color-suppressed.

Similarly, applying this procedure to $D^0 \to \overline{K}^{*0}\rho^0$ the matrix element is:

$$< \overline{K}^{*0}\rho^0|H|D^0 >= \frac{G_F}{\sqrt{2}} a_2 < \overline{K}^{*0}|(\overline{s}d)|0 >< \rho^0|(\overline{u}c)|D^0 > \tag{1.34}$$

where

$$a_2 = c_2 + \xi c_1 \tag{1.35}$$

This time, there is a direct contribution from the effective neutral current, and a color suppressed contribution from the effective charged current.

The decay $D^+ \to \overline{K}^{*0}\rho^+$ has terms proportional to both a_1 and a_2:

$$\begin{aligned} < \overline{K}^{*0}\rho^+|H|D^+ >= \frac{G_F}{\sqrt{2}} \Big[& a_1 < \rho^+|(\overline{u}d)|0 >< K^{*-}|(\overline{s}c)|D^+ > \\ & + a_2 < \overline{K}^{*0}|(\overline{s}d)|0 >< \rho^+|(\overline{u}c)|D^+ > \Big] \end{aligned} \tag{1.36}$$

The matrix elements $< V|J^\mu|D >$ are calculated as in equation (1.9). The vector and pseudoscalar couplings are defined as

$$\begin{aligned} < V|J_\mu|0 > &= \varepsilon_\mu F_V M_V \\ < P|J_\mu|0 > &= -i f_P q_\mu \end{aligned} \tag{1.37}$$

Due to the transversality condition for vector particles,

$$\varepsilon_{vector} \cdot p_{vector} = 0 \tag{1.38}$$

only the terms in equation (1.9) proportional to A_1, A_2, and V are non-zero for $\overline{K}^*\rho$ decays. Therefore, the matrix element for $D^0 \rightarrow K^{*-}\rho^+$, equation (1.32), involves exactly the same form-factors as that for $D^+ \rightarrow \overline{K}^{*0}e^+\nu$ decays. Thus, by measuring $\overline{K}^*\rho$ decays and comparing the results with semileptonic decays, we provide a test of the factorization hypothesis which is independent of the models used to calculate the form-factors.

Because of the unknown contributions from the color octet currents, the value of ξ is taken as a free parameter, and is determined by a fit to the measured branching ratios for the $D \rightarrow K\pi$ modes. Since the BSW model cannot predict the isospin phase shifts, the experimental values of the isospin phase shifts are used to compare the data with the model. The starting values $c_1 = 1.21$ and $c_2 = -0.42$ at the scale of the charm quark mass are assumed. Assuming $\xi = 3$, we expect $a_1 = 1.07$ and $a_2 = -0.02$. The values found in the BSW model are $a_1 = 1.2$ and $a_2 = -0.5$. Thus, they find that effectively $\xi \cong 0$. More precisely, if the errors in c_1 and c_2 due to the uncertainties in m_c and Λ_{QCD} are taken into account, $\xi = 0.1 \pm 0.15$.[25]

Furthermore, the relatively large negative value of a_2 results in a suppression of the D^+ hadronic width.

Table 1.4 shows the measured values and BSW predictions for the $\overline{K}\pi$, $\overline{K}\rho$, and $\overline{K}^*\pi$ decay modes. In the last column, the BSW predictions are recalculated using the experimental values of the isospin phase shifts. Although the predictions do not match the data for individual decay modes, especially for the D^+, they have matched the overall trend of the smaller hadronic width of the D^+. The conclusion from the

Table 1.4 Branching ratios for $\overline{K}\pi$, $\overline{K}\rho$, and $\overline{K}^*\pi$ decay modes.

Mode	Branching Ratio (%)	Ref.	BSW	BSW*
$K^-\pi^+$	$4.2 \pm 0.4 \pm 0.4$	10	6.1	4.8
$\overline{K}^0\pi^0$	$1.9 \pm 0.4 \pm 0.2$	11	0.8	2.1
$\overline{K}^0\pi^+$	$3.2 \pm 0.5 \pm 0.2$	10	3.7	3.7
$K^-\rho^+$	$10.8 \pm 0.4 \pm 1.7$	5	10.7	10.7
$\overline{K}^0\rho^0$	$0.8 \pm 0.1 \pm 0.5$	5	0.3	0.3
$\overline{K}^0\rho^+$	$6.9 \pm 0.8 \pm 2.3$	5	15.2	15.2
$K^{*-}\pi^+$	$5.3 \pm 0.4 \pm 1.0$	5	3.2	2.9
$\overline{K}^{*0}\pi^0$	$2.6 \pm 0.3 \pm 0.7$	5	1.0	1.4
$\overline{K}^{*0}\pi^+$	$5.9 \pm 1.9 \pm 2.5$	5	2.8	0.3

*Corrected for isospin phase shifts.

BSW model is therefore that the lifetime differences of the charmed mesons can be explained by interference in D^+ decays. However, there are only three observed Cabibbo allowed decay modes for which this hypothesis can be tested, and one of them was used in the fit to a_1 and a_2. Therefore, measuring more Cabibbo allowed hadronic D^+ decays is important for testing the size of interference.

The BSW predictions which will be tested in this thesis are, in units of $10^{10} sec^{-1}$:

$$\begin{aligned}
\Gamma(D^0 &\rightarrow K^{*-}\rho^+) = 34.05a_1^2 \\
\Gamma(D^+ &\rightarrow \overline{K}^{*0}\rho^0) = 18.45a_2^2 \\
\Gamma(D^+ &\rightarrow \overline{K}^{*0}\rho^+) = 34.59(a_1 + 1.04a_2)^2 \\
\Gamma(D^+ &\rightarrow \overline{K}^0 a_1^+) = 2.49a_1^2
\end{aligned} \tag{1.39}$$

Using the lifetimes:

$$
\begin{aligned}
B(D^0 \rightarrow K^{*-}\rho^+) &= 21\% \\
B(D^0 \rightarrow \overline{K}^{*0}\rho^0) &= 2.5\% \\
B(D^+ \rightarrow \overline{K}^{*0}\rho^+) &= 17\% \\
B(D^0 \rightarrow K^- a_1^+) &= 5.0\% \\
B(D^+ \rightarrow \overline{K}^0 a_1^+) &= 3.8\%
\end{aligned}
\tag{1.40}
$$

Blok and Shifman[26] (BS) have made predictions with QCD sum rules for $D \rightarrow PP$ and $D \rightarrow PV$ decays. This method takes into account non-factorizable contributions. They find that for most decays, the non-factorizable contributions have opposite signs from the color suppressed factorizable contributions, thus providing an explanation for why the effective value of ξ in the BSW model seems to be less than 1/3.

Non-factorizable contributions are particularly significant for modes with a weak annihilation contribution, where soft gluons may lift the helicity suppression at the light quark vertex. The QCD sum rule calculations indicate that 20% of the hadronic width of the D^0 is due to weak annihilation. In particular, the decay $D^0 \rightarrow \overline{K}^0\phi$ is predicted to proceed through W annihilation, with a branching ratio of 1.3%, compared with the measurement of $0.99 \pm 0.24 \pm 0.14\%$. Also, the branching ratio for $D_s^+ \rightarrow \rho^0\pi^+$ is predicted to be very small, although naively, it was expected to be large if annihilation is large. This prediction is in agreement with the limit[27]

$$
\frac{B(D_s^+ \rightarrow \rho^0\pi^+)}{B(D_s^+ \rightarrow \phi\pi^+)} < 0.08. \tag{1.41}
$$

The annihilation contributions in the BS model include contributions from FSI in Fig. 1.6, which are topologically identical to weak annihilation.

Table 1.5 contains decay modes of the D^0 which are proportional to a_2 only, and

Table 1.5 D^0 decay modes proportional a single isospin amplitude.

Mode	Measurement (%)*	BSW	BS
$\overline{K}^0\eta$	$1.6 \pm 0.6 \pm 0.4$	0.31	0.4
$\overline{K}^0\eta'$	$1.9 \pm 0.4 \pm 0.3$	0.12	1.2
$\overline{K}^0\omega$	$3.2 \pm 1.3 \pm 0.8$	0.32	1.5
$\overline{K}^{*0}\eta$	$2.5 \pm 0.8 \pm 1.0$	0.27	0.25
$\overline{K}^{*0}\eta'$	< 0.2	0.002	
$\overline{K}^{*0}\omega$	$2.0 \pm 0.5 \pm 0.3$	1.9	
$\phi\rho^0$	0.34 ± 0.11	0.09	

*See Ref. 2.

are proportional to a single isospin amplitude, and therefore cannot be increased by isospin phase shifts. Generally, the observed values are much higher than the factorization calculations of BSW, even with $a_2 = -0.5$. The predictions of Blok and Shifman are closer to the observed values.

An interesting test is to look at Cabibbo suppressed decays of the type $D \to \overline{K}K$. Weak annihilation is possible for both the D^0 and D^+, but there is no interference in the case of the D^+. Again, isospin phase shifts are possible, and an isospin decomposition can be written:

$$\begin{aligned} A(D^+ \to |+1/2;+1/2>) &= \sqrt{2}A_1 e^{i\delta_1} \\ A(D^0 \to |-1/2;+1/2>) &= A_1 e^{i\delta_1} + A_0 e^{i\delta_0} \\ A(D^0 \to |+1/2;-1/2>) &= A_1 e^{i\delta_1} - A_0 e^{i\delta_0} \end{aligned} \tag{1.42}$$

Using the measured values,

$$\begin{aligned} B(D^+ \to \overline{K}^0 K^+) &= 1.01 \pm 0.32 \pm 0.18 \\ B(D^0 \to K^- K^+) &= 0.51 \pm 0.09 \pm 0.06 \\ B(D^0 \to \overline{K}^0 K^0) &= 0.11^{+0.06}_{-0.04} \pm 0.02. \end{aligned} \tag{1.43}$$

We obtain, based on these modes, the ratio of hadronic widths:

$$\frac{\Gamma_H(D^0)}{\Gamma_H(D^+)} \cong 1.5 \tag{1.44}$$

which is smaller than the case for the Cabibbo-allowed decays, thus indicating that there is indeed a suppression due to interference in the D^+ Cabibbo-allowed decays.

1.5 An Overview of the Analysis of the $D \to \overline{K}\pi\pi\pi$ Final States.

We present herein an analysis of the resonant substructure of the following final states;[28]

$$\begin{aligned} D^0 &\to K^-\pi^+\pi^+\pi^- \\ D^+ &\to \overline{K}^0\pi^+\pi^+\pi^- \\ D^+ &\to K^-\pi^+\pi^+\pi^0 \\ D^0 &\to \overline{K}^0\pi^+\pi^-\pi^0 \end{aligned} \tag{1.45}$$

There are three more possible $\overline{K}\pi\pi\pi$ final states, which have too many neutral particles to detect efficiently:

$$\begin{aligned} D^0 &\to K^-\pi^+\pi^0\pi^0 \\ D^0 &\to \overline{K}^0\pi^0\pi^0\pi^0 \\ D^+ &\to \overline{K}^0\pi^+\pi^0\pi^0 \end{aligned} \tag{1.46}$$

This represents the first detailed study of the decay modes contributing to a four-body final state. We show that two-body decays are the principal component, and obtain branching ratios of decays to two vector mesons (VV), to a pseudoscalar and an axial vector meson (PA), and of nonresonant decay modes.

Table 1.6 shows the fraction of events that end up in each final state for several decay modes. There are four types of decay modes listed in the table: $\overline{K}a_1$, $\overline{K}^*\rho$,

Table 1.6 Fractions of decay modes to the final states.

	D^0		D^+		D^0		D^+
	K^- π^+ π^+ π^-	$\overline{K}^0$ π^+ π^- π^0	$\overline{K}^0$ π^+ π^+ π^-	K^- π^+ π^+ π^0	K^- π^+ π^0 π^0	$\overline{K}^0$ π^0 π^0 π^0	$\overline{K}^0$ π^+ π^0 π^0
$K^- a_1^+$	1/2				1/2		
$\overline{K}^0 a_1^0$		1					
$\overline{K}^0 a_1^+$			1/2				1/2
$K^{*-}\rho^+$		2/3			1/3		
$\overline{K}^{*0}\rho^0$	2/3	1/3					
$\overline{K}^{*0}\rho^+$				2/3			1/3
$K_1(1270)^-\pi^+$	0.34	0.48			0.05		
$\overline{K}_1(1270)^0\pi^0$		0.34			0.48	0.05	
$\overline{K}_1(1270)^0\pi^+$			0.48	0.34			0.05
$K_1(1400)^-\pi^+$	4/9	4/9			1/9		
$\overline{K}_1(1400)^0\pi^0$		4/9			4/9	1/9	
$\overline{K}_1(1400)^0\pi^+$			4/9	4/9			1/9
Number of events	1281	140	209	142			
Backgrounds	Low	High	Low	Med.			

$\overline{K}_1(1270)\pi$, and $\overline{K}_1(1400)\pi$. Each of these types comes in three isospin combinations.

The $D^0 \to K^-\pi^+\pi^+\pi^-$ final state has the most statistics, with low background. The $D^+ \to \overline{K}^0\pi^+\pi^+\pi^-$ and $D^+ \to K^-\pi^+\pi^+\pi^0$ final states have less statistics, but the backgrounds are still reasonable, and the resonant substructure is expected to be relatively simple, since few decay modes are expected to be involved. Furthermore, some decay modes contribute to both of these final states, allowing cross-checks between the analyses for these final states. Given that these three final states have

Table 1.7 Features of hadronic decays of D^0 and D^+ mesons.

D^0	D^+
W-exchange Cabibbo allowed	W-exchange Cabibbo suppressed
Large effects from isospin phase shifts	No effects from isospin phase shifts
Inelastic FSI	FSI through exotic I=3/2 channel only
	Interference between spectator diagrams

been analyzed, the $D^0 \to \overline{K}^0\pi^+\pi^-\pi^0$ final state provides information about the third isospin combination of many decay modes, allowing us to complete the pattern for these modes. However, the quality of the data for this final state is relatively poor. The statistics are low, the backgrounds high, and sensitivity is further reduced since we cannot tell if an individual candidate event consists of a D^0 decay or a $\overline{D}^0$ decay. Furthermore, the resonant substructure is potentially very complicated, with many decay modes contributing. However, using information from the other final states, it is possible to make useful measurements of the resonant substructure in this final state.

1.6 Summary.

Measurements of PP and PV decays indicate that the understanding of the D^0 and D^+ lifetimes lies in an understanding of two-body hadronic decay modes. However, this indication is based on measured branching ratios accounting for only about a third of the total hadronic widths, including only three Cabibbo-allowed D^+ decay modes.

Several features of hadronic charm decays have been discussed here. These are summarized in Table 1.7, listed separately for D^0 and D^+. Thus, we see that D^+

decays are considerably simpler than D^0 decays to interpret theoretically. We have also seen that there are indications that both weak annihilation and interference play a role in the lifetime difference.

In this thesis, a measurement of the resonant substructure of four $D \to \overline{K}\pi\pi\pi$ final states will allow us to extend the study of hadronic two-body decays to a much greater fraction of the total hadronic width. We will measure branching ratios for two important classes of decays, VV and PA. By measuring all three isospin combinations where possible, we will determine the effects of isospin phase shifts on the branching ratios. This will allow us to compare our results with the model of Bauer, Stech, and Wirbel.

For the decay modes $D \to \overline{K}^*\rho$, detailed information on the polarization of the $\overline{K}^*$ and ρ emerges naturally from our analysis technique, allowing us to obtain information on the form-factors for this decay. In the factorization hypothesis, these form-factors are the same as the ones for the decay $D^+ \to \overline{K}^{*0}e^+\nu$, for which recent results are not in agreement with models. By comparing our results with the results on semileptonic decays, we will be able to test the factorization hypothesis in a manner independent of these models.

2
The Mark III Detector.

2.1 An Overview.

The data for this thesis were collected with the Mark III detector at the SLAC e^+e^- storage ring SPEAR, which operates in the 3 to 5 GeV center-of-mass energy range. The design of the detector is optimized for complete reconstruction of hadronic final states. This requires high efficiency for both charged particles and photons down to very low energy, and particle identification. (For the final states studied in this thesis, charged particle momenta range from 0 to 0.75 GeV/c, peaking at 0.35 GeV/c, and photon energies range from 0 to 0.7 GeV, peaking at 0.15 GeV.) To accomplish this, the following design features were used:

- The drift chambers, used to track charged particles, cover 85% of the solid angle. The amount of material in front of and in the drift chambers is minimal, totaling 0.02 radiation lengths, in order to minimize ionization energy losses (dE/dx) and multiple Coulomb scattering for charged particles, and photon conversions.

- The shower counters are placed inside the magnet coil, in order to optimize detection efficiency and energy resolution for low-energy photons. The shower

counters cover 94% of the solid angle.

- The main source of particle identification is the time-of-flight (TOF) counters placed just inside the barrel shower counter. Layer 2 of the drift chambers also provides particle identification with dE/dx measurements. The shower counters can be used to discriminate pions from electrons. Muons can be identified with two layers of proportional tubes within and outside the magnet flux return steel.

Construction of the detector was completed in 1982. An axial view of the detector is shown in Fig. 2.1, and a side view in Fig. 2.2. In this chapter, the main features of the components used for the analysis in this thesis are briefly described. The overall detector is described in detail in Ref. 29. More detailed descriptions are available for the main drift chamber,[30] the TOF counters,[31] the barrel shower counters,[32] the endcap shower counters,[33] and the trigger.[34]

2.2 The Drift Chambers.

The drift chambers can be divided into three sections. The innermost, layer 1, is a small chamber in a container separate from the outer two sections, and is used for the initial trigger as well as tracking. The main drift chamber contains layer 2, used for energy loss measurements as well as tracking, and layers 3 through 8, which supply the bulk of the tracking. The solenoidal magnet coil provides a field of 0.4 T. At this field, tracks with transverse momentum greater than 0.08 GeV/c will reach the outside of the drift chambers. All the layers are axial except for layers 4 and 6, which have stereo angles of 7.7° and −9.0° in order to supply Z coordinate information, where the Z-axis is defined as the axis perpendicular to the plane of

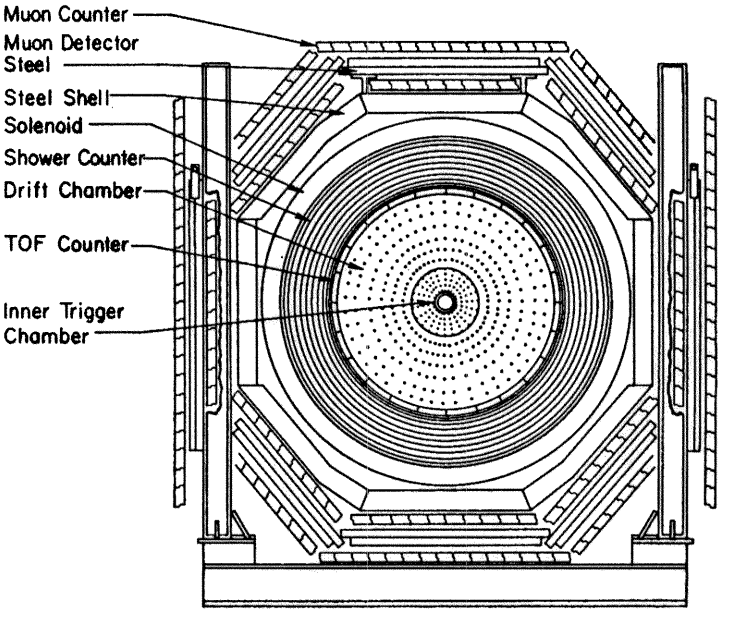

Figure 2.1 Axial view of the Mark III detector.

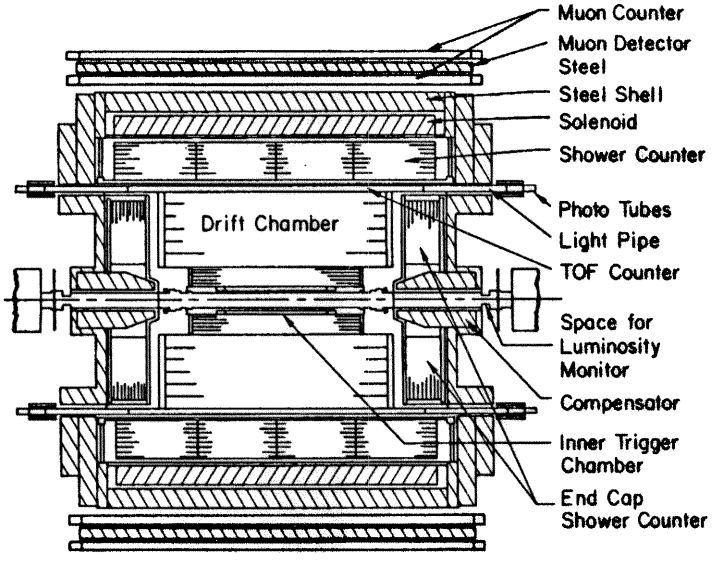

Figure 2.2 Side view of the Mark III detector.

Fig. 2.1. Z coordinate information is also obtained from charge division in layers 1, 3, 5, and 7, with resolution of about 2 cm. However, the Z positions obtained from the stereo layers have a much better resolution of about 0.2 cm, depending on the steepness of the track.

Layer 1, shown in Fig. 2.3, consists of four radial wire planes at radii between 0.098 and 0.134 m, and covers 98% of 4π steradians. Because of its small radius, layer 1 is useful both for tracking near the interaction region, and for triggering on tracks that come from the beam spot. Each wire plane in layer 1 is divided into 32 cells with one sense wire and one field wire each. Adjacent wire planes have a relative offset of one half cell. For tracks from the beam spot, the sum of the drift times from cells in adjacent layers is roughly constant, as shown in Fig. 2.4, while the sum of times from cosmic rays has a broader distribution.

Layer 2 is also divided into 32 cells azimuthally, with 12 sense wire planes each, as shown in Fig. 2.5. Pulse heights from each sense wire are measured, to obtain the dE/dx of the tracks. This system is effective for $K-\pi$ separation at low momentum, although some separation is possible up to $0.65\,\mathrm{GeV}/c$, as shown in Fig. 2.6.

For layers 3 through 8, the layers are divided into N x 16 cells azimuthally, with 3 sense wire planes each, as shown in Fig. 2.7. Within a cell, the sense wires from the three wire planes are staggered relative to each other by ± 0.4 mm. This makes it possible to determine to which side of the sense wires the track lies, as shown in Fig. 2.8.

A novel program is used to reconstruct tracks in the drift chambers.[35] First, the pattern of hit cells is compared to a dictionary of 12,832 possible patterns, and hits are assigned to tracks. Then, a fit to a circle performed to provide an initial

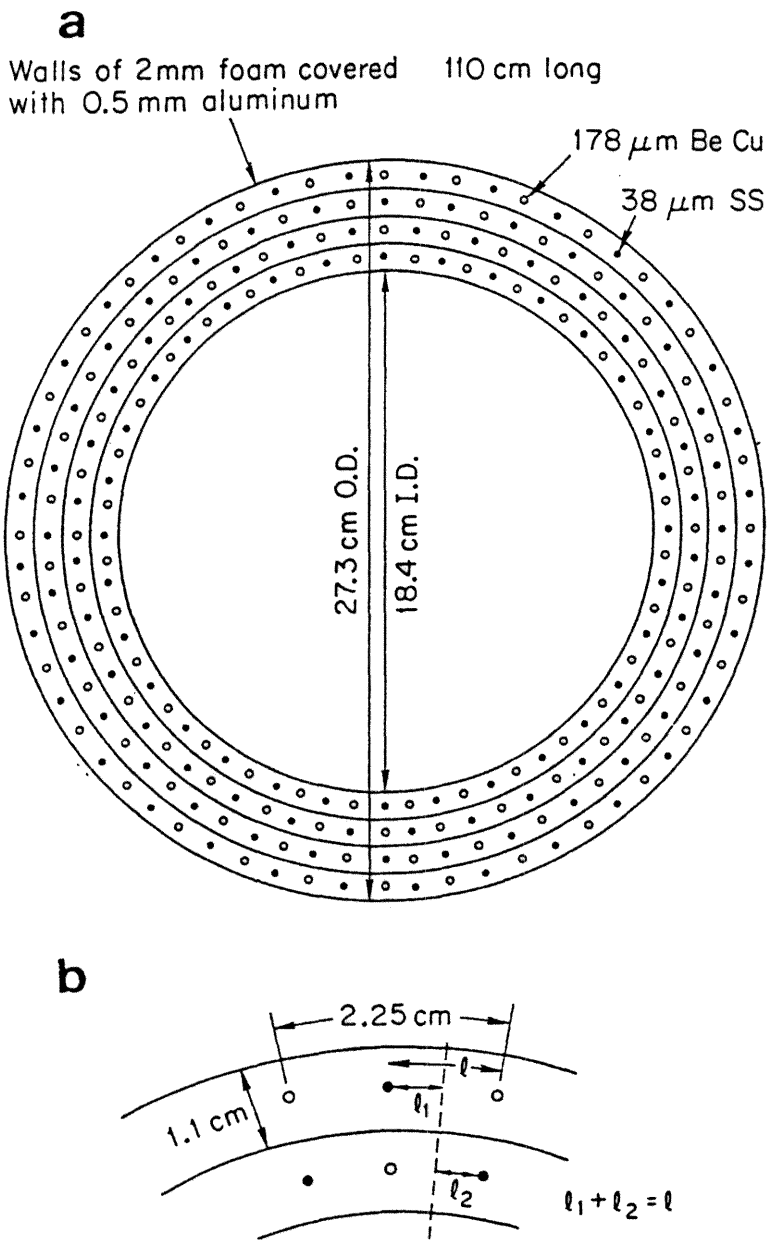

Figure 2.3 (a) End view of Layer 1. (b) End view showing the offset between wire planes.

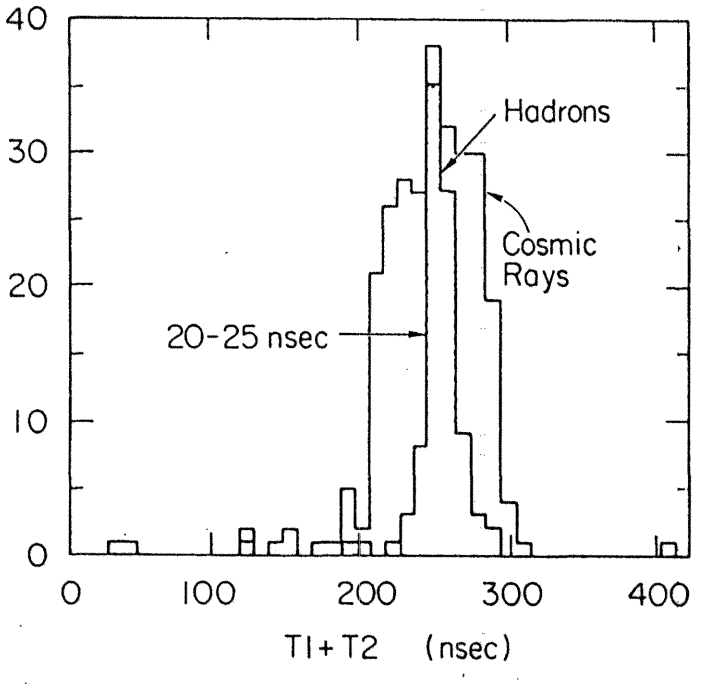

Figure 2.4 Distribution of layer 1 time sum.

starting point for the final track fit, and to resolve any ambiguities about assigning hits to tracks. A final fit is performed, taking into account energy loss and Coulomb scattering, details of the magnetic field, details of the drift chamber geometry and response, and the variation of the X-Y position of the stereo layers with Z.

For 75% of the tracks, Z information is obtained from the two stereo layers. If information from one or more of the stereo layers is missing, the event vertex, charge division, or information from the shower counter may be used for Z information instead.

Track parameters are determined to a typical precision of:

$$\frac{\delta p}{p} = 0.015\sqrt{1+p^2} \tag{2.1}$$

$$\delta\phi = 0.002 \text{ radians} \tag{2.2}$$

$$\delta\tan\lambda = 0.011 \tag{2.3}$$

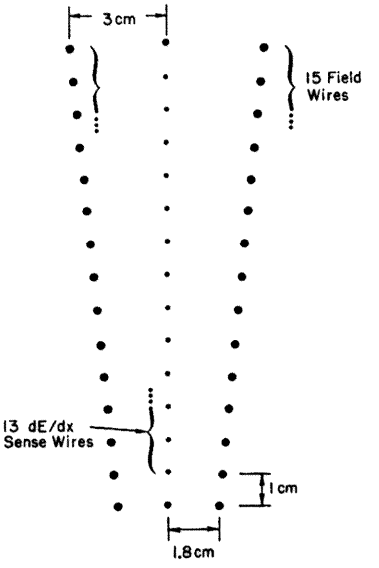

Figure 2.5 A cell in layer 2. Field wires are shown as large dots, guard wires as medium dots, and sense wires as small dots. The middle sense wire is used as a guard wire.

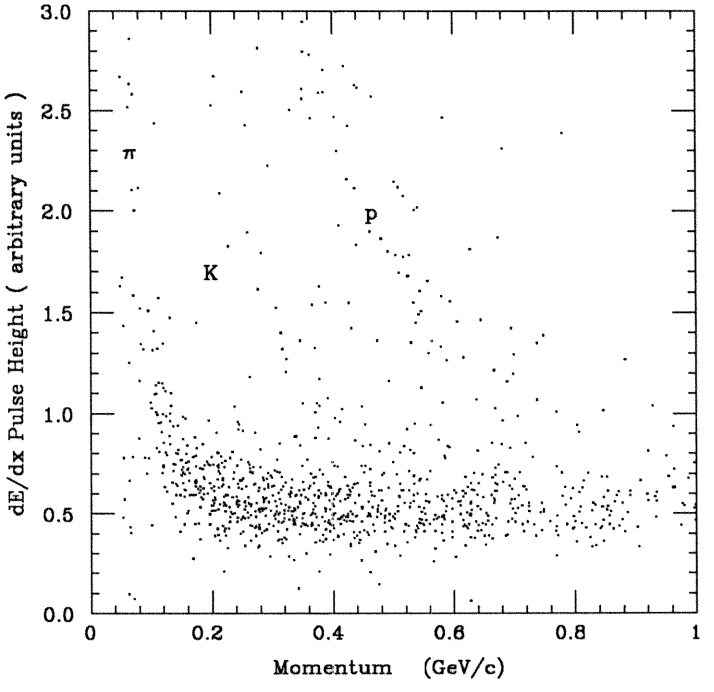

Figure 2.6 Layer 2 pulse height versus momentum.

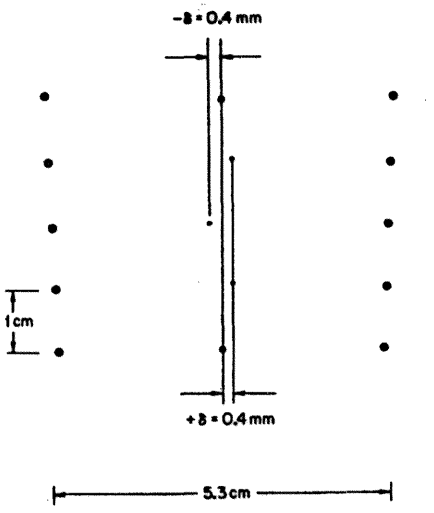

Figure 2.7 The sense wires are staggered azimuthally in each cell.

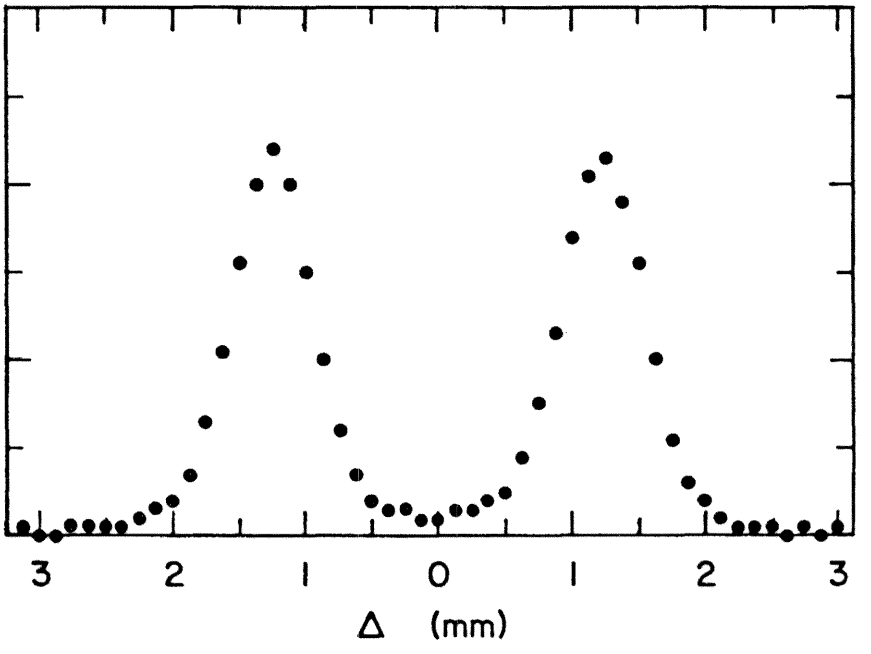

Figure 2.8 Time differences for offset wires of layer 3 showing resolution of the left–right ambiguity.

where p is the momentum in GeV, ϕ is the azimuthal angle, and λ is the dip angle.

2.3 Time of Flight.

The time-of-flight (TOF) system, the main system used for charged particle identification, is shown in Fig. 2.9. It consists of 48 scintillation counters 5 cm thick, mounted parallel to the beam axis at a radius of 1.18 m, and covering 80% of the solid angle. The mean resolution is 170-190 psec, depending on particle type, and provides $\pi - K$ separation up to 1.2 GeV/c, as shown in Fig. 2.10.

2.4 Shower Counters.

The barrel and endcap shower counters are shown in Fig. 2.11 and Fig. 2.12. Together, they cover 94% of 4π. In order to provide efficient photon detection with good resolution, the barrel shower counter is mounted inside the coil, to minimize the amount of material in front of the first sampling layer. There are 24 sampling layers, consisting of proportional tubes axially mounted and interleaved with 0.5 radiation length lead sheets. The lead sheets are alloyed with 6% antimony and clad with 0.64 mm aluminum for mechanical strength. The first six layers are read out individually, while the outer layers are read out in groups of three. Both pulse height and charge division are measured, in order to obtain the energy of the shower as well as its position. The energy resolution is

$$\frac{\sigma_E}{E} = \frac{18\%}{\sqrt{E}} \tag{2.4}$$

where E is in GeV. The azimuthal and polar angle resolutions are $\sigma_\phi = 7$ mr, and $\sigma_\theta = 20$ mr. The efficiency approaches 100% at 0.1 GeV, falling to roughly 50% at 0.05 GeV.

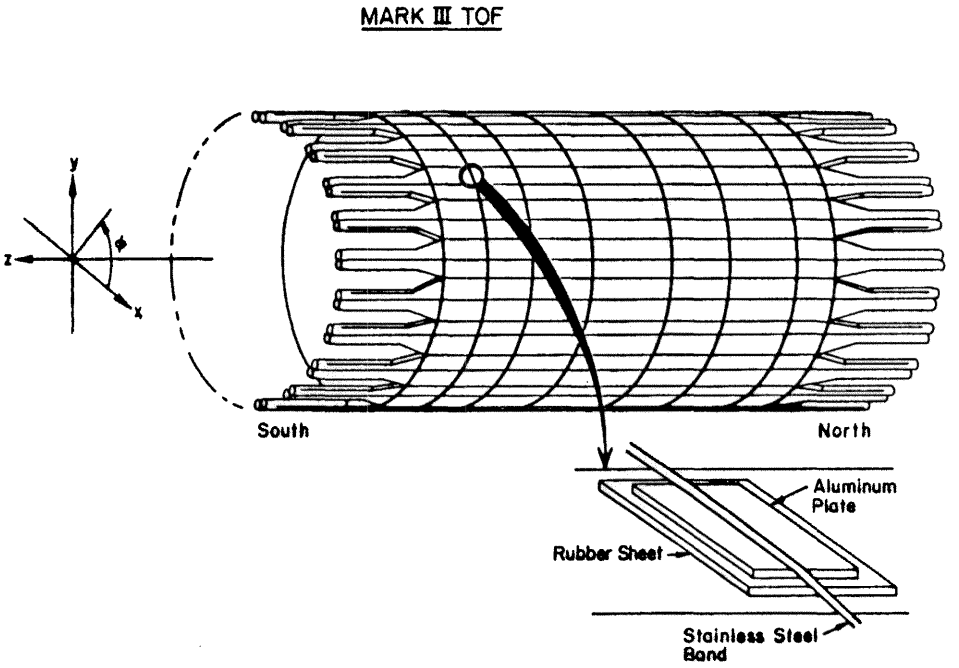

Figure 2.9 Scintillators and light guides mounted on the outside of the main drift chamber.

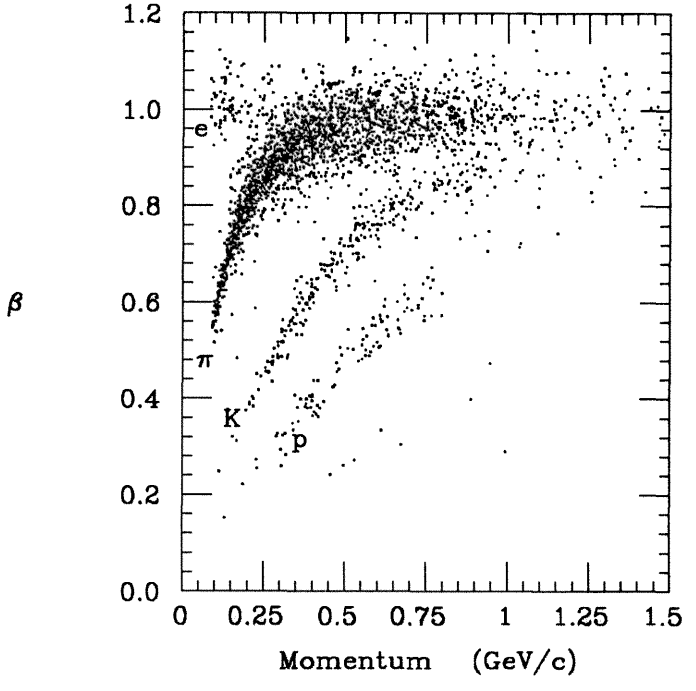

Figure 2.10 TOF versus momentum.

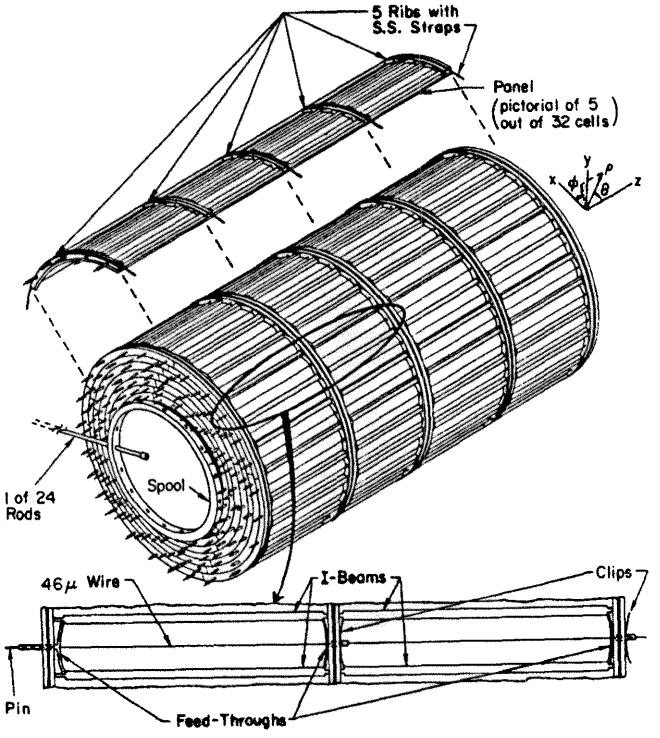

Figure 2.11 The barrel shower counter.

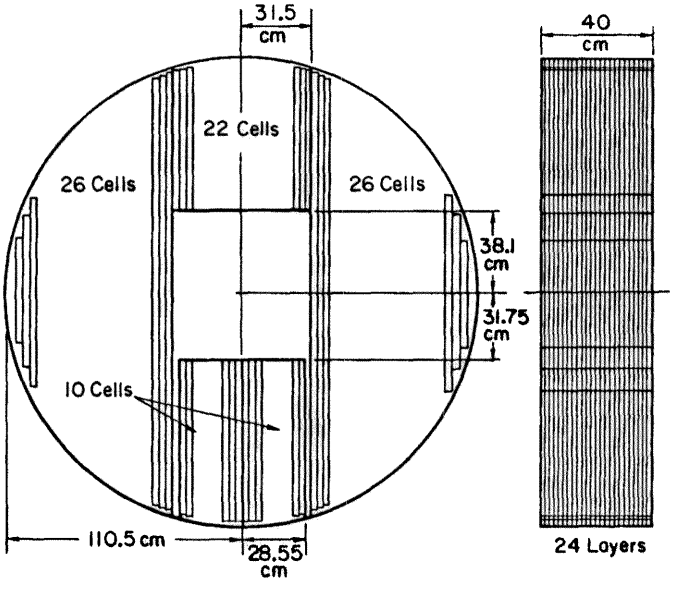

Figure 2.12 The endcap shower counter.

2.5 The Trigger.

Collisions at SPEAR occur every 780 ns, while read-out of the Mark III detector takes approximately 30 ms. A trigger has been developed that is nearly 100% efficient for interesting events, while providing significant rejection against cosmic rays and beam-gas events. Since the initial trigger decision is made in less than one beam-crossing, dead-time is reduced to 10% or less, depending on luminosity and beam energy.

The trigger is divided into two stages. The first stage requires less than one beam-crossing to make its decision. If the first stage is satisfied, the second stage requires another beam-crossing. Each stage may be satisfied by a number of different criteria. Up to six trigger sequences may be simultaneously operating, each requiring a different set of criteria for each stage.

The first stage of the trigger may be satisfied two different ways. A valid time sum is looked for in layer 1, as described in the drift chamber section, or a TOF hit may be required. The second stage looks at hit cells in layers 1,2,3, and 5, and determines whether there are one, two or more track candidates. Fig. 2.13 shows some possible patterns of hit cells.

At the $\psi(3770)$, two different trigger sequences were used. The first required two drift chamber tracks, and the second required one drift chamber track and a TOF hit. The trigger rate for the first stage was 4 to 10 KHz, reduced to 4 Hz at the second stage.

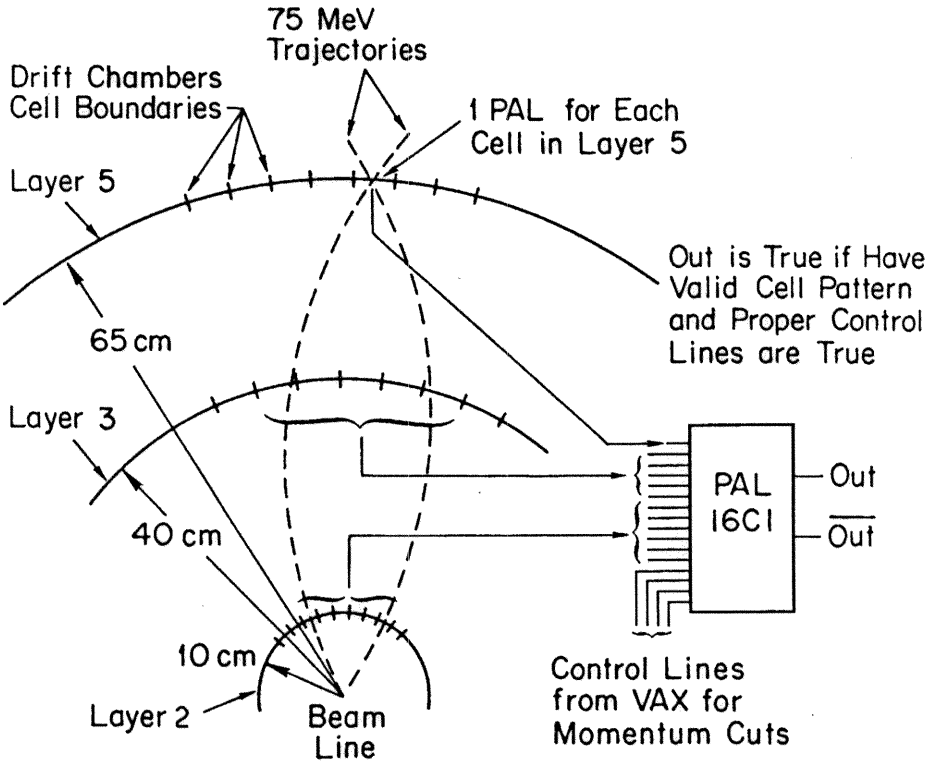

Figure 2.13 Trigger track finding and logic in the second stage.

3
Event Selection.

The starting point for the resonant substructure analyses is the signals for the final states being studied. Signals for several $\overline{K}\pi\pi\pi$ final states been previously observed in the Mark III data.[11] The procedures and cuts used to select events containing the signals are mostly standard, and a standard program, called the "tag package," is used to select events for all the final states studied herein except for $D^0 \to \overline{K}^0\pi^+\pi^-\pi^0$. This chapter summarizes these procedures and cuts, describes in detail the final event selection criteria which are particular to this analysis, and presents the signals for each final state. More details of the procedures may be found in Ref. 11.

3.1 The Data Set.

The data were collected in three separate runs, during fall of 1982, spring of 1983, and spring of 1984. The center-of-mass energy was between 3.758 and 3.778 GeV/c^2, near the peak of the $\psi(3770)$ resonance. The total integrated luminosity has been determined from Bhabha and dimuon events to be 9.56 pb^{-1}, with a 5% systematic error.

The $\psi(3770)$ lies below $D^*\overline{D}$ threshold, and decays predominantly to $D\overline{D}$. Thus, D mesons are produced with a unique momentum. Also, the observation of one D in an event implies the presence of a second. This property has been exploited to determine absolute branching ratios for D decays, and cross-sections for D production.[36,37] The cross-sections are $\sigma_{D^0} = 5.8 \pm 0.5 \pm 0.6$ nb and $\sigma_{D^+} = 4.2 \pm 0.6 \pm 0.3$ nb.

3.2 Initial Event Selection.

For each reconstructed track in the drift chamber, there are five track parameters and an associated error matrix. These parameters are the azimuthal angle of the track at the distance of closest approach to the Z axis, the tangent of the polar angle of the track, the distance of closest approach to the Z axis, and the Z position at this distance of closest approach.

To improve the momentum resolution of the tracks, information about the interaction point for the event can be used. Two types of fits have been developed to do this, the *vertex fit* and the *beam fit*. dE/dx and multiple scattering corrections are done for the track parameters and error matrices, according to the particle hypothesis assigned to the track. The vertex fit constrains all charged tracks in the event to come from a single point, which is required to be in the beam interaction region. New error matrices are calculated, but correlations induced between the parameters of different tracks are ignored. This type of fit is used in the tag package. The beam fit simply constrains each individual track to originate from the beam spot. Again, the error matrices are recalculated. This type of fit is used for the $D^0 \to \overline{K}^0\pi^+\pi^-\pi^0$ final state.

Given a mass hypothesis for a charged track, the expected time-of-flight (TOF) can be calculated. If information from the TOF system is available, charged tracks are classified as pions or kaons according to which expected time from the two mass hypotheses is closer to the observed time. Also, the time is required to be within 5σ of the expected time. If TOF information is not available, dE/dx information is used in a similar manner.

$\overline{K}^0$ candidates are detected through the decay $\overline{K}^0 \rightarrow K_s \rightarrow \pi^+\pi^-$. To select K_s candidates, the crossing points in the X-Y plane of pion pairs are determined. The track parameters and error matrices are recalculated for this secondary vertex. Cuts can then be imposed on the invariant mass of the pion pairs, the distance of the secondary vertex from the center of the beam spot, and the probability that the position of the secondary vertex aligns with the K_s momentum vector. Tracks from K_s candidates are excluded from the vertex fit, and are not subjected to a beam fit.

Neutral pion candidates are detected through the decay $\pi^0 \rightarrow \gamma\gamma$. In order to be accepted as photon candidates, neutral showers are required to originate within the first six layers of the shower counter, and to contain hits in at least two layers of the shower counter. The cosine of the angle from the photon to the nearest charged track must be less than 0.95, at the entrance to the calorimeter. Photon pairs are then subjected to a kinematic constraint in which the energies and positions of the photons are varied within errors, with the constraint that the invariant mass of the photon pair be the π^0 mass. In order for the photon pair to be accepted as a π^0 candidate, the χ^2 of the fit is required to be less than 6 per degree of freedom, and the fit photon energies are required to be greater than 50 MeV.

Fiducial cuts are often placed on tracks, requiring the tracks to be detected in regions where the detector efficiency is best understood. These cuts are: $|\cos\theta| <$

0.75 for kaons identified by TOF, $|\cos\theta| < 0.85$ for other charged tracks, and $|\cos\theta| < 0.95$ for photons, where θ is the polar angle. For final states with low statistics, these cuts may be relaxed, at the price of additional systematic uncertainty in the detection efficiency.

3.3 The Recoil Mass Plot.

In the Mark III $\psi(3770)$ data sets, D mesons are produced in the reaction $e^+e^- \rightarrow \psi(3770) \rightarrow D\bar{D}$. For each $\overline{K}\pi\pi\pi$ combination, an effective recoil mass can be calculated using $E_{\rm recoil} = E_\psi - E_{\overline{K}\pi\pi\pi}$ and $P_{\rm recoil} = -P_{\overline{K}\pi\pi\pi}$. For a real $D \rightarrow \overline{K}\pi\pi\pi$ event, both the invariant mass and the recoil mass of the $\overline{K}\pi\pi\pi$ combination will be near the D mass. For each $\overline{K}\pi\pi\pi$ combination, we perform a kinematic fit in which the mass of the combination is constrained to the D mass and the recoil mass is allowed to vary. The signal can then be seen in the recoil mass plot as a peak at the D mass. With this type of constraint, all events have the same amount of phase space for the decay throughout the recoil mass plot. This has the advantage that the kinematic boundaries of the phase space for the 4-body decay are the same in the sideband regions and the signal regions of the recoil mass plot. The recoil mass plot is fit with a polynomial and an error function cutoff at high mass for the background, and a Gaussian for the signal.

$\overline{K}^0$ candidates are detected through the decay $\overline{K}^0 \rightarrow K_s \rightarrow \pi^+\pi^-$. Thus, for final states in which the kaon is neutral, the constraint that the invariant mass of the two pions be the neutral kaon mass is added to the kinematic fit. Similarly, π^0 candidates are detected through their decay to two photons. In final states with a π^0, the constraint that the invariant mass of the two photons be the π^0 mass is

added to the kinematic fit. The kinematic fit is performed by adjusting the track parameters within their errors. A probability for the fit can then be calculated from the χ^2 of the fit and the number of degrees of freedom.

3.4 The Monte Carlo Simulation.

A Monte Carlo simulation is used to determine the efficiencies of the analyses in this thesis. A large number of events (about 120,000) are generated for each $\overline{K}\pi\pi\pi$ final state. For the $D \rightarrow \overline{K}\pi\pi\pi$ decay, the Monte Carlo program randomly generates 4-vectors according to the density of states in 4-body phase space. The decay of the other D is generated according to a model, which consists of a list of decay modes and branching ratios, shown in Tables 3.1 and 3.2. The generated tracks are then propagated through a detailed detector simulation, and raw data is generated in the same format as in real events. The same reconstruction and analysis programs are then used for both real and Monte Carlo data.

3.5 $D^0 \rightarrow K^-\pi^+\pi^+\pi^-$.

The recoil mass plot for the $D^0 \rightarrow K^-\pi^+\pi^+\pi^-$ final state is shown in Fig. 3.1. There are 1281 ± 45 events above background. For this final state, the $K^-\pi^+\pi^+\pi^-$ combinations provided in the tag package are used with no further selection other than a requirement that the probability of the kinematic fit be greater than 0.01. The branching ratio has previously been determined by Mark III to be $(9.1\pm0.8\pm0.8)\%$.[37]

Table 3.1 D^0 decay modes in the Monte Carlo model.

Decay Mode,	Branching Ratio (%)	Decay Mode,	Branching Ratio (%)
$K^-\pi^+$	4.200	$\overline{K}^0\pi^0$	1.900
K^-K^+	0.510	$\overline{K}^0K^0$	0.255
$\pi^-\pi^+$	0.140	$\pi^0\pi^0$	0.014
$\overline{K}^0\eta$	1.500	$\pi^0\eta$	0.008
$\eta\eta$	0.016	$\overline{K}^0\eta'$	0.061
$\pi^0\eta'$	0.004	$K^-\rho^+$	8.450
$\overline{K}^0\rho^0$	0.860	$\overline{K}^0\phi$	0.860
$K^{*-}\pi^+$	5.230	$\overline{K}^{*0}\pi^0$	1.060
$\phi\pi^0$	0.026	$\overline{K}^0\omega$	3.200
$K^{*-}K^+$	0.860	$K^-\pi^+\pi^0$	2.470
$\overline{K}^0\pi^+\pi^-$	2.000	$\overline{K}^0\pi^0\pi^0$	0.800
$K^-2\pi^+\pi^-$	9.100	$K^-\pi^+2\pi^0$	14.900
$2\pi^+2\pi^-$	1.470	$\overline{K}^0\pi^+\pi^-\pi^0$	9.800
$\overline{K}^03\pi^0$	0.750	$\overline{K}^02\pi^+2\pi^-$	0.850
$K^-3\pi^+2\pi^-$	2.350	$K^+K^-\overline{K}^0$	0.850
$\phi\pi^+\pi^-$	0.170	$K^+K^-\pi^+\pi^-$	0.072
$\overline{K}^0K^-\pi^+$	0.870	$\pi^+\pi^-\pi^0$	1.110
$K^-2\pi^+\pi^-2\pi^0$	0.650	$K^-2\pi^+\pi^-\pi^0$	8.280
$K^-\pi^+3\pi^0$	3.400	$K^-e^+\nu$	3.400
$K^-\mu^+\nu$	3.400	$K^{*-}e^+\nu$	3.400
$\pi^-e^+\nu$	0.300	$\pi^-\mu^+\nu$	0.300
$\rho^-e^+\nu$	0.300		

Table 3.2 D^+ decay modes in Monte Carlo model.

Decay Mode,	Branching Ratio (%)	Decay Mode,	Branching Ratio (%)
$\overline{K}^0\pi^+$	3.200	$\overline{K}^0K^+$	1.010
$\pi^0\pi^+$	0.100	$\pi^+\eta'$	0.080
$\overline{K}^{*0}\pi^+$	3.670	$\rho^+\overline{K}^0$	7.540
$\phi\pi^+$	0.770	$\overline{K}^{*0}K^+$	0.440
$K^-\pi^+\pi^+$	6.650	$\overline{K}^0\pi^+\pi^0$	1.440
$K^+K^-\pi^+$	0.540	$\pi^+\pi^+\pi^-$	0.380
$\overline{K}^0\pi^+\pi^+\pi^-$	6.600	$K^-\pi^+\pi^+\pi^0$	6.200
$\overline{K}^0\pi^+\pi^0\pi^0$	5.000	$K^-3(\pi^+)\pi^-$	4.960
$\overline{K}^0\pi^+2(\pi^+\pi^-)$	1.000	$K^-2\pi^+2(\pi^+\pi^-)$	3.300
$\overline{K}^0\pi^+3(\pi^+\pi^-)$	0.500	$K^-2\pi^+2\pi^0$	3.820
$\overline{K}^02\pi^+\pi^-\pi^0$	5.800	$\overline{K}^0\pi^+3\pi^0$	10.200
$\overline{K}^0e^+\nu$	8.100	$\overline{K}^0\mu^+\nu$	8.100
$\overline{K}^{*0}e^+\nu$	7.500	$\pi^0e^+\nu$	0.600
$\pi^0\mu^+\nu$	0.600	$\rho^0e^+\nu$	0.600

3.6 $D^+ \rightarrow \overline{K}^0\pi^+\pi^+\pi^-$.

For the $\overline{K}^0\pi^+\pi^+\pi^-$ final state, the $\overline{K}^0\pi^+\pi^+\pi^-$ combinations provided in the tag package are used with no further selection other than a requirement that the probability of the 2-C kinematic fit be greater than 0.02. The recoil mass plot is shown in Fig. 3.2. There are 209 ± 20 events above background. The branching ratio has previously been determined by Mark III to be $B(D^+ \rightarrow \overline{K}^0\pi^+\pi^+\pi^-) = (6.6 \pm 1.5 \pm 0.5)\%$.[37]

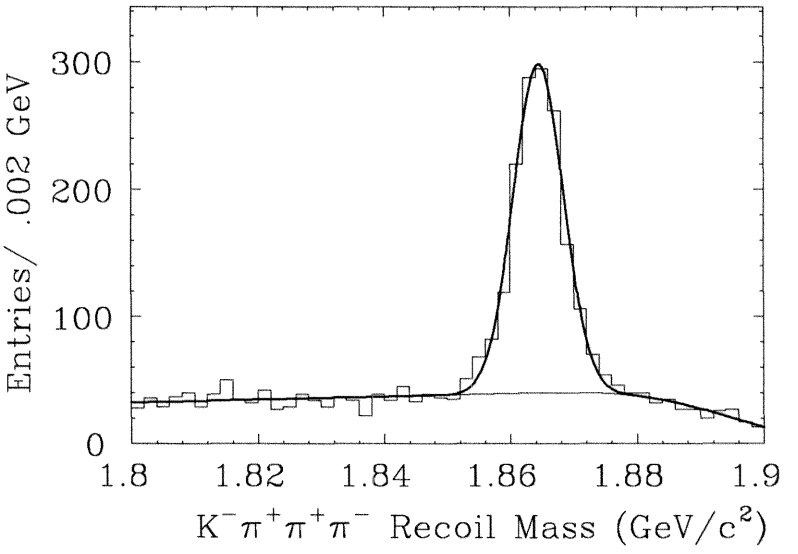

Figure 3.1 Signal for $D^0 \to K^-\pi^+\pi^+\pi^-$.

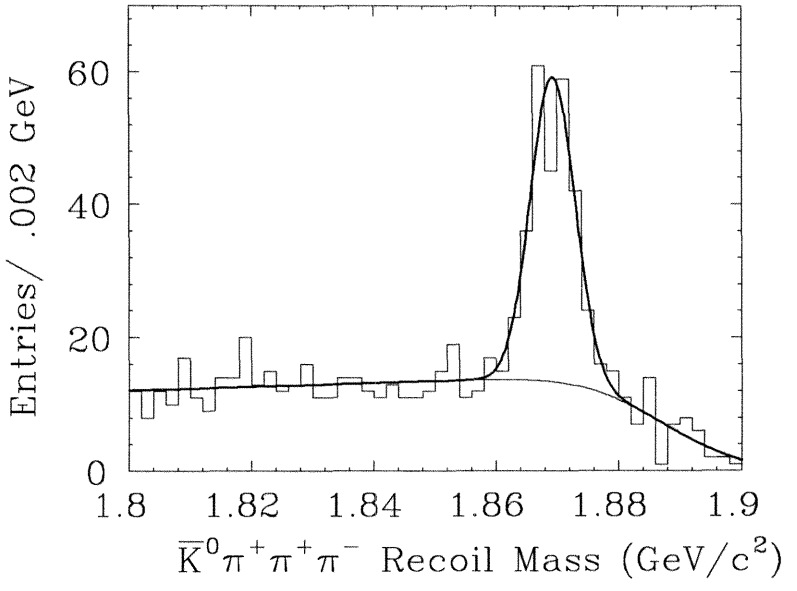

Figure 3.2 Signal for $D^+ \to \overline{K}^0\pi^+\pi^+\pi^-$.

3.7 $D^+ \to K^-\pi^+\pi^+\pi^0$.

For the $K^-\pi^+\pi^+\pi^0$ final state, we start with the $K^-\pi^+\pi^+\pi^0$ combinations provided in the tag package and apply the following additional selection criteria:

- 2-C fit probability > 0.02.
- 2-C fit photon energy > 0.05 GeV.
- cosine of π^0 decay angle < 0.7. (Measured in the π^0 rest frame, with respect to the direction of the lab frame.)
- Less than 2 isolated showers in the recoil, where an isolated shower is defined as a neutral shower for which the cosine of the angle to the nearest charged track is less than 0.97 at the entrance to the shower counter, and whose measured energy is greater than 0.08 GeV.

The first three requirements are standard in Mark III analysis. The recoil mass plot obtained using only these three requirements, shown in Fig. 3.3, has 233 ± 34 signal events. The last requirement is new, and is very effective at decreasing combinatorial background for decay modes with photons. The recoil mass plot obtained using this requirement, shown in Fig. 3.4, has 142 ± 21 signal events, with an improved signal to background ratio. For both of these fits, the mass and width of the signal were held fixed to 1.8693 and .0045 GeV, where the width was determined from Monte Carlo. To check that the background shape obtained in these plots is reasonable, we analyzed a set of Monte Carlo events in which D^0 and D^+ pairs were generated according to the model. The result, shown in Fig. 3.5, is consistent with the background shape in both plots.

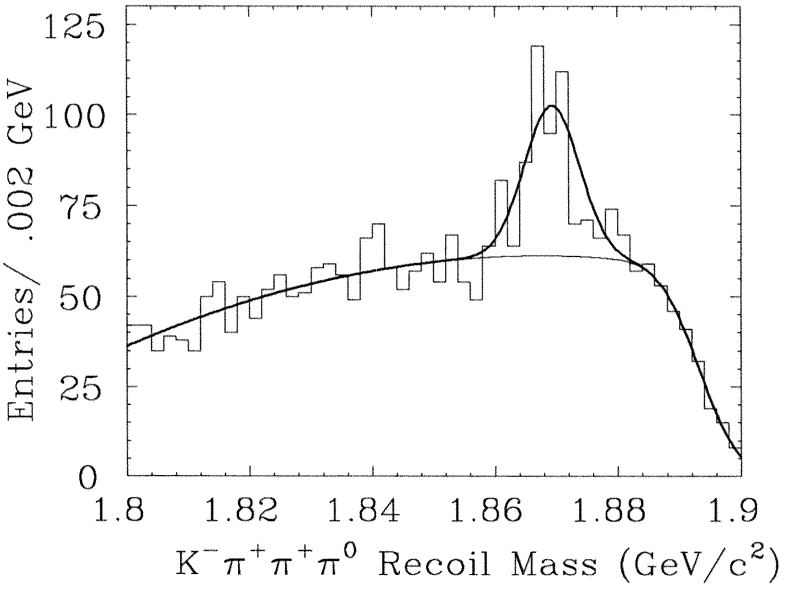

Figure 3.3 Signal for $D^+ \to K^-\pi^+\pi^+\pi^0$, without isolated shower requirement.

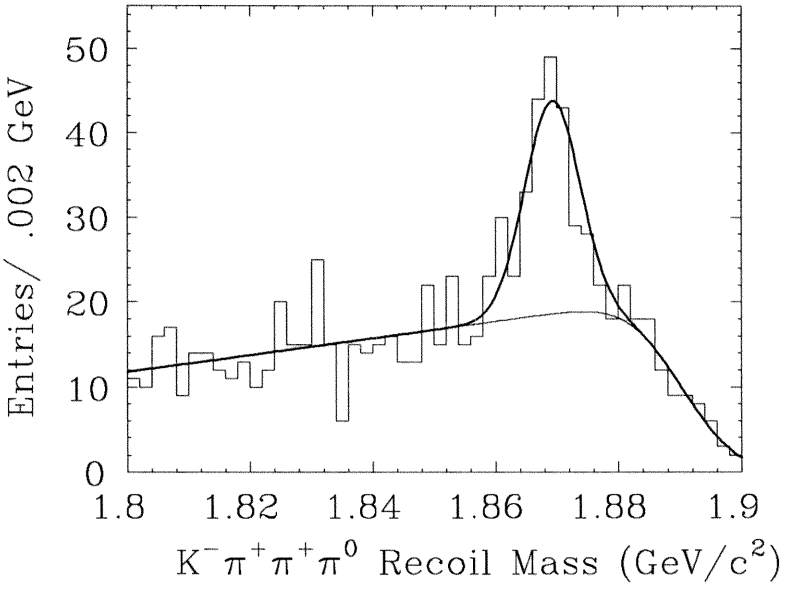

Figure 3.4 Signal for $D^+ \to K^-\pi^+\pi^+\pi^0$, with isolated shower requirement.

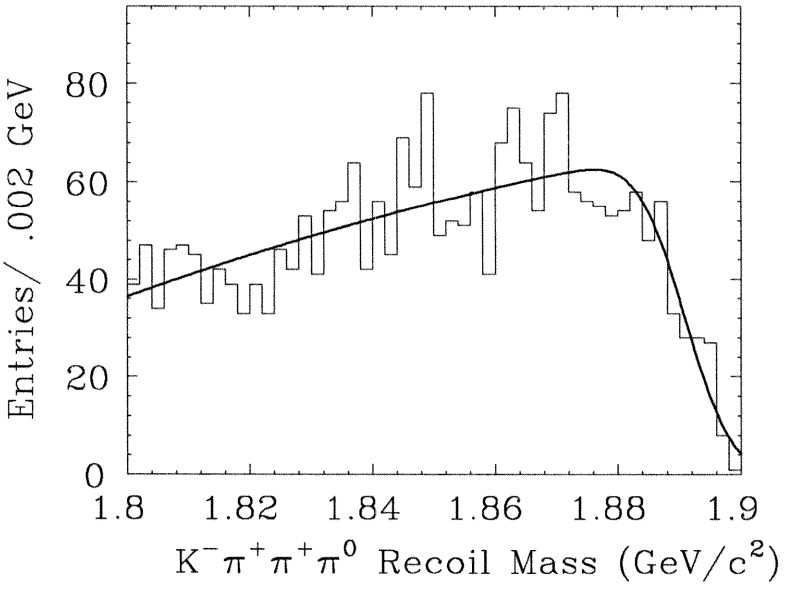

Figure 3.5 $K^-\pi^+\pi^+\pi^0$ Recoil Mass, Monte Carlo background.

The efficiency of the isolated shower requirement cannot be determined by Monte Carlo. It can, however, be directly obtained using the sample of 1600 $D^+ \rightarrow K^-\pi^+\pi^+$ events in the tag package. By measuring the fraction of $D^+ \rightarrow K^-\pi^+\pi^+$ events which pass this requirement, we obtain an efficiency of 0.549 ± 0.022, where the error is statistical only. This agrees with the value $0.61 \pm .13$ obtained from the fits to the plots in Fig. 3.3 and Fig. 3.4.

The sensitivity of this requirement to noise hits in the shower counter is minimized by only counting showers which have a relatively high energy. The sensitivity to showers which are "split-offs" from showers from nearby charged tracks is minimized by only counting showers which are relatively far from a charged track. The efficiency of this requirement may depend on the topology of the decay mode being reconstructed. For example, if one decay mode has more charged prongs than

another, there is a greater chance that the shower from one of the charged tracks will overlap with a photon in the recoil, reducing the average number of isolated showers.

To estimate the systematic error on the efficiency of the isolated shower requirement, we perform the following checks:

- Variations of the fit function used to obtain the number of $D^+ \to K^-\pi^+\pi^+$ events before and after the requirement, contributing 0.007 to the systematic error.

- In order to perform the resonant substructure analysis, we have generated a large number of Monte Carlo $D^+ \to \overline{K}^0\pi^+\pi^+\pi^-$ and $D^+ \to K^-\pi^+\pi^+\pi^0$ events, with the D^+ model for the recoil. Applying the isolated shower requirement to these Monte Carlo samples, we obtain for the efficiency 0.657 ± 0.003 and 0.642 ± 0.004 respectively. We take the difference between these values, 0.015, as an estimate of the systematic error due to the different track topologies.

- We apply the requirement to the $D^+ \to \overline{K}^0\pi^+$, $D^+ \to \overline{K}^0\pi^+\pi^+\pi^-$, and $D^+ \to \overline{K}^0\pi^+\pi^0$ tag samples, and find values for the efficiency consistent within statistical errors of about 0.07.

- We select $K^-\pi^+\pi^+$ tags in three kaon momentum bins, and determine the efficiency separately in each bin. We find values consistent within statistical errors of 0.03 to 0.05.

- We determine the efficiency for $D^+ \to K^-\pi^+\pi^+$ tags separately for each of the three data taking periods. Again, we find values consistent within statistical errors.

We obtain, combining the first two systematic errors and the statistical error in quadrature, an efficiency of 0.549 ± 0.028 for the isolated shower requirement.

Using phase-space-generated Monte Carlo events, we determine the efficiency for the rest of the analysis to be 11.8%. We find from the resonant substructure analysis in chapter 7 that the efficiency, relative to the efficiency for a phase space distribution, is 0.949.

For the following systematic errors, we use the same values as in Ref. 11:

- Photon detection efficiency (7%).
- Tracking efficiency (5%).
- Tails in the χ^2 distribution of the kinematic fits (10%).
- The absence of fiducial requirements (5%).
- Total integrated luminosity (5%).

We have separately determined the following systematic errors which are specific to this analysis:

- Variations of the recoil mass fit function (11%).
- Efficiency of the isolated photon requirement (5%).
- Relative efficiency (1%).

We obtain, using 9.56 pb^{-1} as the value for the integrated luminosity, $\sigma B = 242 \pm 36 \pm 48$ pb, in agreement with the value in Ref. 11, $\sigma B = 260 \pm 40 \pm 54$ pb. Using the value $\sigma_{D^+} = 4.2 \pm 0.6 \pm 0.3$ nb, we obtain $B(D^+ \to K^-\pi^+\pi^+\pi^0) = (5.8 \pm 1.2 \pm 1.2)\%$. A previous Mark III analysis found $B(D^+ \to K^-\pi^+\pi^+\pi^0) = (6.3^{+1.4}_{-1.3} \pm 1.2)\%$,[36] but this analysis was found to be flawed.[37,38] The E691 collaboration has published the value $B(D^+ \to K^-\pi^+\pi^+\pi^0) = (6.3 \pm 1.3 \pm 1.5)\%$.[39]

3.8 $D^0 \to \overline{K}^0\pi^+\pi^-\pi^0$.

The $\overline{K}^0\pi^+\pi^-\pi^0$ final state is not part of the tag package, so we must select the event combinations ourselves, as described above. We apply the following additional requirements:

- 3-C fit probability > 0.15.
- 2-C fit photon energy > 0.05 GeV.
- K_s decay length > 3 mm.
- Probability that the K_s momentum vector and vertex position vector align in the x-y plane > 0.01.

The recoil mass plot obtained, shown in Fig. 3.6, has 140 ± 28 signal events. For the fit, the mass and width of the signal were held fixed to 1.8645 and 0.0048 GeV, where the width was determined from Monte Carlo. To check that the background shape obtained in this plot is reasonable, we analyzed a set of Monte Carlo events where D^0 pairs were generated according to the model. The result is shown in Fig. 3.7, with the background shape from Fig. 3.6 superimposed on the Monte Carlo events.

Using phase-space-generated Monte Carlo events, we determine the efficiency for the analysis to be 2.4%. We find from the resonant substructure analysis in chapter 8 that the efficiency, relative to the efficiency for a phase space distribution, is 1.0.

For the following systematic errors, we use the same values as in Ref. 11:

- Photon detection efficiency (7%).

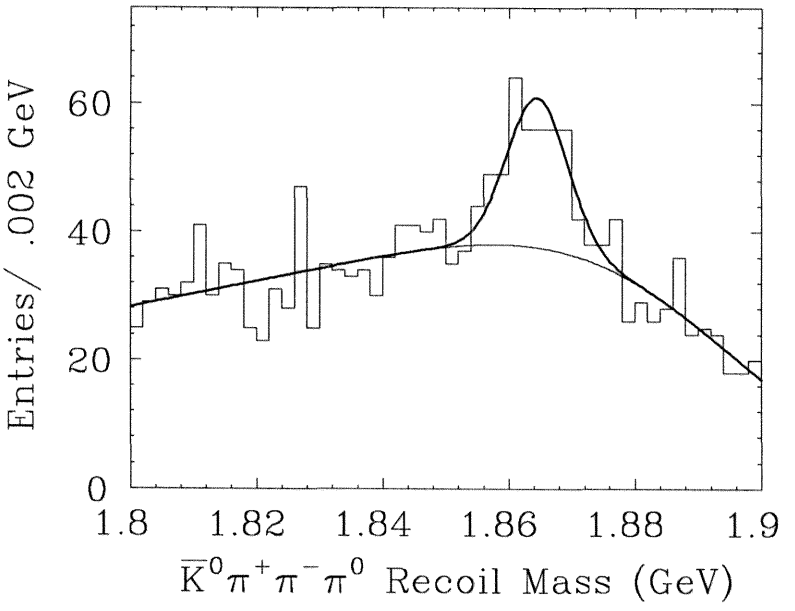

Figure 3.6 Signal for $D^0 \to \overline{K}^0\pi^+\pi^-\pi^0$.

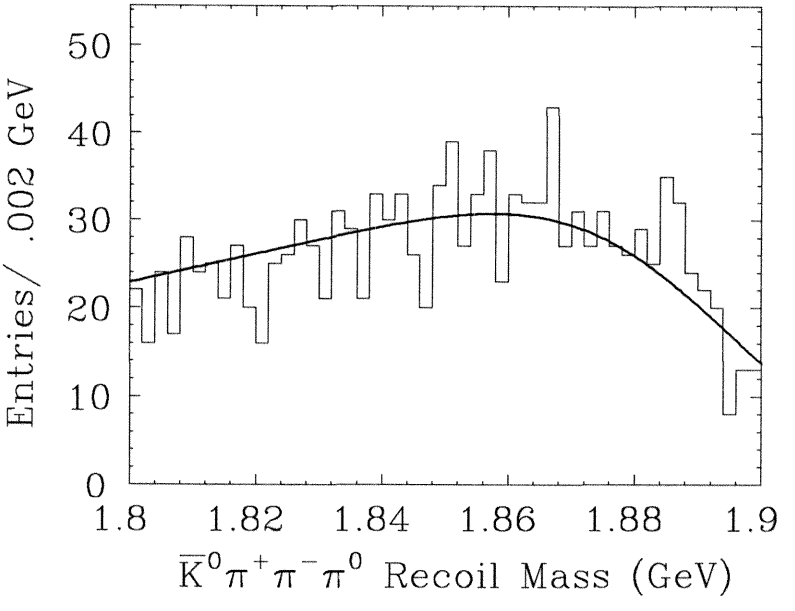

Figure 3.7 $\overline{K}^0\pi^+\pi^-\pi^0$ Recoil Mass, Monte Carlo background.

- Tracking efficiency (5%).
- Tails in the χ^2 distribution of the kinematic fit (10%).
- K_s vertex requirements (5 %).
- The absence of fiducial requirements (5%).
- Total integrated luminosity (5%).

We have separately determined the following systematic errors which are specific to this analysis:

- Variations of the recoil mass fit function (15%).
- Relative efficiency (1%).

We obtain, using 9.56 pb^{-1} as the value for the integrated luminosity, $\sigma B = 599 \pm 118 \pm 131$ pb, in agreement with the number in Ref. 11, $\sigma B = 666 \pm 113 \pm 153$ pb. Using the value $\sigma_{D^0} = 5.8 \pm 0.5 \pm 0.6$ nb, we obtain $B(D^0 \rightarrow \overline{K}^0\pi^+\pi^-\pi^0) = (10.3 \pm 2.2 \pm 2.5)\%$.

4
The Fitting Technique.

For each $D \to \overline{K}\pi\pi\pi$ final state, there are several two-body and three-body decay modes which can contribute. We determine the contribution of each decay mode using a maximum likelihood fit. Conceptually, the fitting technique is very simple, and is a straightforward extension of the techniques commonly used in three-body Dalitz plot fits. For each decay mode, we define a complex amplitude in the four-body phase space. These amplitudes overlap and interfere. We define a probability density function (p.d.f.) which consists of a coherent sum of these amplitudes, and fit to the data to determine the relative fractions and phases of these amplitudes.

In practice, this analysis is complex. The phase space is five-dimensional, and therefore difficult to visualize. The p.d.f. must take into account variations in efficiency throughout the phase space, and must be properly normalized. Amplitudes for many complicated decay chains must be derived. Finally, there are the difficult experimental questions of which amplitudes to include in the fit and which to leave out, and of how to determine the systematic errors. In the following sections, we discuss each of these points in detail.

4.1 The Phase Space.

The p.d.f., a function in the phase space defined by the 4-momenta of the decay products of the D candidate, provides a complete description of the decay.

To count the number of independent kinematic variables in this phase space, we start with the four 4-vectors with 16 components. Since the invariant mass of each is defined, there are only 12 independent components. Energy and momentum conservation provides four relationships between the components. Since the D is a pseudoscalar and has no preferred orientation, we subtract three for the three overall rotations. Thus, we find that the phase space is five-dimensional.

A wide variety of kinematic variables can be defined, such as 2-body and 3-body invariant masses, and helicity angles. Since we are analyzing the complete phase space, and not just a projection, we do not have to "choose" any five particular variables, but instead use whichever ones are convenient for each term in the p.d.f.

The Monte Carlo program randomly generates 4-vectors according to the density of states in the phase space; this distribution is called the phase space distribution. These 4-vectors may be used as generated to simulate events as produced, or they may be propagated through a detector simulation in order to simulate events as detected, accounting for detector efficiency.

The phase space is five-dimensional, but we can only visualize distributions in one or two-dimensional projections. The distribution due to an individual amplitude can be very striking if the appropriate projection is made. For example, if the amplitude involves a narrow resonance, it might show up as a peak in an invariant mass distribution. If the resonance is too broad to be distinct, the amplitude may still have a very distinct angular distribution. One emphasis of this thesis is to

illustrate the distributions of individual amplitudes using projections in judiciously chosen kinematic variables.

4.2 The Likelihood Function.

The likelihood function $\mathcal{L}$ is defined as

$$\mathcal{L} = \prod_{events} \mathcal{F} \tag{4.1}$$

where $\mathcal{F}$ is the p.d.f. The p.d.f. consists of a signal term $\mathcal{F}_S$ and a background term $\mathcal{F}_B$:

$$\mathcal{F} = \frac{R_{S/B}\mathcal{F}_S + \mathcal{F}_B}{R_{S/B} + 1}. \tag{4.2}$$

As discussed in the previous chapter, the $\overline{K}\pi\pi\pi$ peak is seen in the recoil mass plot, which is fit to a curve consisting of a Gaussian for the signal, and a smooth background. For each event we calculate the ratio of signal to background, $R_{S/B}$, as a function of recoil mass, using the curve fit to the recoil mass plot.

The Signal p.d.f.

The signal p.d.f. $\mathcal{F}_S$ consists of a coherent sum of complex amplitudes, weighted by the density of states in phase space and the detector efficiency. Each amplitude is individually normalized over phase space before taking into account detector efficiency, and $\mathcal{F}_S$ as a whole is normalized over phase space weighted by the detector efficiency:

$$\begin{aligned} \mathcal{F}_S &= \frac{1}{N_{\mathcal{F}_S}}\epsilon \left| \sqrt{f_1^M}\, e^{i\alpha_1} \frac{S_1}{\sqrt{N_1}} + ... + \sqrt{f_n^M}\, e^{i\alpha_n} \frac{S_n}{\sqrt{N_n}} \right|^2 \phi \\ &= \frac{1}{N_{\mathcal{F}_S}} \sum_{i=1}^{n} \sum_{j=1}^{n} \sqrt{f_i^M} \sqrt{f_j^M}\, \Re e \left(e^{i(\alpha_i - \alpha_j)} \frac{\epsilon S_i S_j^* \phi}{\sqrt{N_i N_j}} \right) \end{aligned} \tag{4.3}$$

where:

- S_i are complex amplitudes varying over phase space.
- ϵ is the detector efficiency as a function of location in phase space.
- ϕ is the 4-body phase space function.
- The fractions f_i^M and the phases α_i are varied in the fit to maximize the likelihood.
- N_i are the normalizations of the amplitudes over phase space weighted by ϕ:

$$N_i = \int_{phase\ space} S_i S_i^* \phi dV. \tag{4.4}$$

For the purpose of calculating these integrals numerically, a large number of Monte Carlo events are generated, and the normalizations are taken to be:

$$N_i = \sum_{MC\ generated} S_i S_i^*. \tag{4.5}$$

The sum is performed over all generated events, before the detector simulation.

- $N_{\mathcal{F}_S}$ is the overall normalization of the p.d.f.:

$$N_{\mathcal{F}_S} = \sum_{i=1}^{n} \sum_{j=1}^{n} \sqrt{f_i^M} \sqrt{f_j^M}\ \Re e \left(e^{i(\alpha_i - \alpha_j)} E_{ij} \right) \tag{4.6}$$

where

$$E_{ij} = \frac{1}{\sqrt{N_i N_j}} \int_{phase\ space} \epsilon S_i S_j^* \phi dV. \tag{4.7}$$

E_{ij} is calculated numerically by summing over reconstructed Monte Carlo events that pass all cuts.

$$E_{ij} = \frac{1}{\sqrt{N_i N_j}} \sum_{MC\ accepted} S_i S_j^* \tag{4.8}$$

The Background p.d.f.

The background p.d.f. is:

$$\mathcal{F}_B = \frac{1}{N_{\mathcal{F}_B}} \sum_{i=1}^{m} g_i^M \frac{\epsilon B_i \phi}{M_i}. \tag{4.9}$$

The B_i are functions which describe the resonant content of the background. They are similar to the S_i, except they do not interfere with each other. The fractions g_i^M are varied to fit to the events in the recoil mass plot that are outside the signal region. The normalizations M_i and $N_{\mathcal{F}_B}$ are evaluated with the same procedures used for $\mathcal{F}_S$.

4.3 Finding the Maximum of the Likelihood.

To find the maximum of the likelihood function, we minimize $-\ln \mathcal{L}$ using the general minimization program MINUIT.[40] The functions ϵ and ϕ do not depend on the f_i^M or α_i, and are factored out before the minimization. If we define $\mathcal{F}_S = \epsilon\phi S$ and $\mathcal{F}_B = \epsilon\phi B$, then

$$-\ln \mathcal{L} = -\sum_{\textit{signal events}} \ln\left(\frac{R_{S/B} S + B}{R_{S/B} + 1}\right) - \ln \epsilon\phi. \tag{4.10}$$

The term $\ln \epsilon\phi$ is a constant for the purpose of minimizing F and is neglected. We therefore never explicitly need to evaluate ϵ and ϕ; they are taken into account entirely by Monte Carlo techniques. MINUIT calculates an error matrix by making a quadratic approximation to the fit function around the minimum, and evaluating this quadratic where the value of the fit function increases by 0.5 relative to the minimum.[41]

4.4 The Normalization of the Fractions.

The minimization is performed by setting one fraction and one phase to a constant and letting the relative fractions and phases vary. The physical constraint is that the p.d.f. for the produced distribution of events before efficiency effects be normalized to one. This function is:

$$\mathcal{F}_P = \left| \sqrt{f_1^M}\ e^{i\alpha_1} \frac{S_1}{\sqrt{N_1}} + ... + \sqrt{f_n^M}\ e^{i\alpha_n} \frac{S_n}{\sqrt{N_n}} \right|^2 \phi. \tag{4.11}$$

To properly normalize $\mathcal{F}_P$ we rescale the MINUIT fractions f_i^M to obtain the physical fractions f_i:

$$f_i = \frac{f_i^M}{P} \tag{4.12}$$

where P is the integral of $\mathcal{F}_P$:

$$P = \sum_{i=1}^{n} \sum_{j=1}^{n} \sqrt{f_i^M} \sqrt{f_j^M}\ \Re e \left(e^{i(\alpha_i - \alpha_j)} N_{ij} \right) \tag{4.13}$$

and

$$N_{ij} = \frac{1}{\sqrt{N_i N_j}} \sum_{MC\ generated} S_i S_j^*. \tag{4.14}$$

Note that due to interference between the amplitudes,

$$\sum_{i=1}^{n} f_i \neq 1. \tag{4.15}$$

4.5 The Sum of a Subset of Amplitudes.

To obtain the sum of a subset of amplitudes, we have to sum the complex coefficients:

$$f_{sum} = \sum_{i}^{subset} \sum_{j}^{subset} \sqrt{f_i} \sqrt{f_j}\ \Re e \left(e^{i(\alpha_i - \alpha_j)} N_{ij} \right). \tag{4.16}$$

4.6 The Relative Efficiency.

One more useful quantity can be extracted from all this formalism, the *relative efficiency*. This is the average efficiency given the resonant structure relative to the efficiency for a phase space distribution. The relative efficiency is given by:

$$\epsilon_r = \frac{N_{\mathcal{F}_S}}{E_{kk}P} \tag{4.17}$$

where the kth amplitude is the phase space amplitude.

4.7 Making Projections.

We obtain projections of the p.d.f. by summing over reconstructed Monte Carlo events, weighting each event by

$$\frac{R_{S/B}S + B}{R_{S/B} + 1}. \tag{4.18}$$

since the events already have a $\epsilon\phi$ distribution, and accumulating these weights into histograms.

4.8 Notation.

The final states $D^0 \to K^-\pi^+\pi^+\pi^-$, $D^+ \to \overline{K}^0\pi^+\pi^+\pi^-$, and $D^+ \to K^-\pi^+\pi^+\pi^0$ all have two identical positive pions. The $\pi^+\pi^-$ or $\pi^+\pi^0$ combination with the higher mass is referred to as $(\pi^+\pi^-)_{\text{high}}$ or $(\pi^+\pi^0)_{\text{high}}$, the other as $(\pi^+\pi^-)_{\text{low}}$ or $(\pi^+\pi^0)_{\text{low}}$. The $\overline{K}^0\pi^+$ or $K^-\pi^+$ combination formed with the π^+ not used in $(\pi^+\pi^-)_{\text{high}}$ or $(\pi^+\pi^0)_{\text{high}}$ is referred to as $(\overline{K}^0\pi^+)_1$ or $(K^-\pi^+)_1$, the other as $(\overline{K}^0\pi^+)_2$ or $(K^-\pi^+)_2$. Alternatively, phase space may be divided according to high and low $\overline{K}\pi^+$ mass, with the notation $(K^-\pi^+)_{\text{high}}$, $(\pi^+\pi^-)_1$, etc.

For the $D^0 \to \overline{K}^0\pi^+\pi^-\pi^0$ final state, none of the pions are identical. Ideally, mass plots involving the charged pions would be divided according to the charge of the pion relative to the charge of the charmed quark. However, since we don't know the charge of the charmed quark for events in this final state, we continue to divide plots the same way as for the other final states, as if the charged pions were identical. For example, we will write $(\pi^+\pi^-)_{\text{high}}$ and $(K^-\pi^+)_1$.

For the final states with identical pions, the amplitudes are symmetrized. for the $D^0 \to \overline{K}^0\pi^+\pi^-\pi^0$ final state, the amplitudes are symmetrized in a non-coherent manner, as discussed in detail in chapter 8. Therefore, dividing the phase space in terms of high and low mass has no impact on the p.d.f., but is done simply for our convenience. Nonetheless, $(K^-\pi^+)_1$ and $(K^-\pi^+)_2$, for example, are independent kinematic variables; plotting them separately provides more information than a histogram with two entries per event. For example, the $\overline{K}^*$ peaks from two different amplitudes will have different heights in the different $K^-\pi^+$ plots.

4.9 Error Propagation.

To obtain the errors on the final fractions, we must propagate the error matrix according to equation (4.12), accounting for the errors on f_i^M and P. No propagation is necessary for the errors on the phases.

Starting with the standard error propagation formula, we obtain:

$$Var\ f_k = \sum_{i,j} \frac{\partial f_k}{\partial x_i}\frac{\partial f_k}{\partial x_j} Var(x_i, x_j) \tag{4.19}$$

where the set of variables x_i includes both the f_i^M and the α_i, and $Var(x_i, x_j)$ is

the MINUIT error matrix. Evaluating the derivatives, we obtain:

$$\frac{\partial f_i}{\partial f_j^M} = \delta_{ij}\frac{1}{P} - \frac{f_i^M}{P^2}\frac{\partial P}{\partial f_j^M} \tag{4.20}$$

$$\frac{\partial f_i}{\partial \alpha_j} = -\frac{f_i^M}{P^2}\frac{\partial P}{\partial \alpha_j} \tag{4.21}$$

$$\frac{\partial P}{\partial f_i^M} = N_{ii} + \frac{1}{f_i^M}\sum_{j\neq i}\sqrt{f_i^M}\sqrt{f_j^M}\,\Re e\left(e^{i(\alpha_i-\alpha_j)}N_{ij}\right) \tag{4.22}$$

$$\frac{\partial P}{\partial \alpha_i} = -2\Im m\left(\sum_{j\neq i}\sqrt{f_i^M}\sqrt{f_j^M}\,e^{i(\alpha_i-\alpha_j)}N_{ij}\right). \tag{4.23}$$

4.10 The Amplitudes.

We model each decay chain with a complex amplitude consisting of a Breit-Wigner for each resonance in the decay chain, times a form-factor for each vertex in the decay chain, times a matrix element depending on the spin and parity of the intermediate resonances and final decay products. These matrix elements are either Lorentz invariant matrix elements,[42] or helicity amplitudes.[43] The amplitudes are symmetrized for the final states with two identical pions.

Lorentz Invariant Amplitudes.

Lorentz invariant matrix elements are constructed by describing a decay in terms of sequential two-body vertices. Intermediate states may consist of resonances, or nonresonant states in which two particles are in a particular partial wave. The total matrix element is the product of the matrix elements for each vertex, which are constructed from the 4-momenta and polarization vectors of the in-going and two out-going states. The Lorentz invariant matrix elements used are listed in Table 4.1.

Table 4.1 Given a vertex $A \to B + C$, A, B, and C have 4-momenta p_A, p_B, and p_C respectively; $q_A = p_B - p_C$ is the difference between the outgoing momenta. Pseudo-scalars, scalars, vectors, axial vectors, and tensors are denoted by P, S, V, A, and T respectively.

Lorentz Invariant Amplitudes	
Mode	Amplitude
$D \to PP_1$, $P \to VP_2$, $V \to P_3P_4$	$p^\mu_{P_2}(g^{\mu\nu} - p^\mu_V p^\nu_V / M^2_V) q^\nu_V$
$D \to AP_1$, $A \to VP_2$ $V \to P_3P_4$	$p^\mu_{P_1}(g^{\mu\nu} - p^\mu_A p^\nu_A / M^2_A)(g^{\nu\sigma} - p^\nu_V p^\sigma_V / M^2_V) q^\sigma_V$
$D \to AP_1$, $A \to SP_2$, $S \to P_3P_4$	$p^\mu_{P_1}(g^{\mu\nu} - p^\mu_A p^\nu_A / M^2_A) q^\nu_A$
$D \to V_1V_2$, $V_1 \to P_1P_2$, $V_2 \to P_3P_4$ (V_1 and V_2 in relative S-wave.)	$q^\mu_{V_1}(g^{\mu\nu} - p^\mu_{V_1} p^\nu_{V_1} / M^2_{V_1})(g^{\nu\sigma} - p^\nu_{V_2} p^\sigma_{V_2} / M^2_{V_2}) q^\sigma_{V_2}$
$D \to V_1V_2$, $V_1 \to P_1P_2$, $V_2 \to P_3P_4$ (V_1 and V_2 in relative P-wave.)	$\epsilon_{\alpha\beta\gamma\delta} p^\alpha_D q^\beta_D q^\gamma_{V_1} q^\delta_{V_2}$
$D \to V_1V_2$, $V_1 \to P_1P_2$, $V_2 \to P_3P_4$ (Longitudinal D-wave.)	$q^\mu_{V_1}(g^{\mu\nu} - p^\mu_{V_1} p^\nu_{V_1} / M^2_{V_1}) p^\nu_{V_2}$ $\times\ q^\mu_{V_2}(g^{\mu\nu} - p^\mu_{V_2} p^\nu_{V_2} / M^2_{V_2}) p^\nu_{V_1}$
$D \to VS$, $V \to P_1P_2$, $S \to P_3P_4$	$p^\mu_S(g^{\mu\nu} - p^\mu_V p^\nu_V / M^2_V) q^\nu_V$
$D \to V_1P_1$, $V_1 \to V_2P_2$, $V_2 \to P_3P_4$	$\epsilon_{\alpha\beta\gamma\delta} p^\alpha_{V_1} q^\beta_{V_1} p^\gamma_{P_1} q^\delta_{V_2}$
$D \to TP_1$, $T \to VP_2$, $V \to P_3P_4$	$((p_{P_1} \cdot q_T) - (p_{P_1} \cdot p_T)(q_T \cdot p_T)/M^2_T)$ $\times\ \epsilon_{\alpha\beta\gamma\delta} p^\alpha_T q^\beta_T q^\gamma_V p^\delta_{P_1}$
Three-body nonresonant	Substitute $1/p^2$ for $1/M^2$.
Four-body nonresonant	Constant

There are two independent 4-momenta at each vertex, the momentum of the in-going particle, p, and the difference of the momenta of the outgoing particles, q. The polarization vectors of massive spin 1 particles with helicity λ are:[44]

$$\begin{aligned} \varepsilon^{(\lambda=\pm 1)} &= \mp(0,1,\pm i,0)\sqrt{2} \\ \varepsilon^{(\lambda=0)} &= (p,0,0,E)/M. \end{aligned} \tag{4.24}$$

The completeness relation is:

$$\sum_{\lambda} \varepsilon_{\mu}^{\lambda *} \varepsilon_{\nu}^{\lambda} = -g_{\mu\nu} + \frac{p_{\mu} p_{\nu}}{M^2}. \tag{4.25}$$

For a massive vector particle,

$$\varepsilon^{\mu} p_{\mu} = 0. \tag{4.26}$$

This sort of formalism has been extended to spin 2 particles.[45] These momentum and polarization 4-vectors are contracted with each other according to the spin and parity of the particles involved, and the orbital angular momentum of the vertex. The number of factors of q^{μ} in the matrix element for a vertex is proportional to the number of units of orbital angular momentum. The parity of the matrix element is even if the number of units of orbital angular momentum is even, otherwise it is odd. Each factor of q^{μ} or p^{μ} contributes a factor of -1 to the parity, each factor of ε^{μ} contributes a factor of $+1$, and the antisymmetric tensor $\epsilon^{\alpha\beta\gamma\delta}$ contributes a factor of -1.

Sometimes, an alternative form of the completeness relation is used, which differs from equation (4.25) when off the peak of a resonance:

$$-g^{\mu\nu} + p^{\mu} p^{\nu} / p^2. \tag{4.27}$$

This is also the form used for non-resonant decays when a subset of the final state particles are in a spin 1 state. This form has the property of being identical to the

helicity formalism even when off the peak of the resonance. For broad resonances, it is not obvious which form is more correct. The difference in the results obtained with the two forms is included as a systematic uncertainty.

As an example, we consider a vertex $V \to PP$, which has one unit of orbital angular momentum:

$$ME = \varepsilon^{\mu} q_{\mu} \tag{4.28}$$

For a vertex $V_1 \to V_2 P$, which also has one unit of orbital angular momentum, we have:

$$ME = \epsilon^{\alpha\beta\gamma\delta} p_{\alpha} q_{\beta} \varepsilon^1_{\gamma} \varepsilon^2_{\delta}. \tag{4.29}$$

To obtain the matrix elements in Table 4.1, matrix elements for each vertex are multiplied together to obtain the total matrix element. In the total matrix element, each polarization vector appears twice; the completeness relation may therefore be used. This procedure assumes that the couplings to the different helicities of the spin 1 resonance are identical. For example:

$$\begin{aligned} D &\to V_1 V_2 \quad \varepsilon_1 \cdot \varepsilon_2 \\ V_1 &\to P_1 P_2 \quad \varepsilon_1 \cdot q_1 \\ V_2 &\to P_3 P_4 \quad \varepsilon_2 \cdot q_2 \end{aligned} \tag{4.30}$$

Leading to:

$$ME = q_1 \cdot \varepsilon_1 \;\; \varepsilon_1 \cdot \varepsilon_2 \;\; \varepsilon_2 \cdot q_2. \tag{4.31}$$

Using the completeness relation, this equals the amplitude for $D \to V_1 V_2$ in Table 4.1.

Helicity Amplitudes.

The decay $D \to V_1 V_2$ may involve more than one helicity. The helicity formalism leads to three amplitudes $A_{1,1}$, $A_{-1,-1}$, and $A_{0,0}$. The measurement of longitudinal polarization of the K^* in semileptonic D decays[46] suggests that we fit the transverse amplitudes $A_{1,1}, A_{-1,-1}$ independently from the longitudinal amplitude, $A_{0,0}$.

We define the transverse amplitude as:

$$\begin{aligned} A_T &= A_{1,1} + A_{-1,-1} \\ &= \sin\theta_1 \sin\theta_2 \cos\phi \end{aligned} \tag{4.32}$$

and the longitudinal amplitude as:

$$\begin{aligned} A_L &= A_{0,0} \\ &= \cos\theta_1 \cos\theta_2 \end{aligned} \tag{4.33}$$

where θ_1 and θ_2 are the helicity angles of the two vectors, and ϕ is the angle between the two vector decay planes. These decay planes are defined by the direction of the vector and one of its decay products, measured in the D rest frame. In the case of $D \to \overline{K}^* \rho$, the helicity angle of the $\overline{K}^*$ is defined as the angle between the D and the kaon measured in the $\overline{K}^*$ rest frame; the helicity angle of the ρ is defined as the angle between the D and the π^- or π^0 measured in the ρ rest frame; the orientation of the decay plane of the ρ is defined by

$$\vec{p}(\pi^+) \times \vec{p}(\pi^{0,-}) \tag{4.34}$$

and that of the $\overline{K}^*$ by

$$\vec{p}(\pi) \times \vec{p}(K). \tag{4.35}$$

The $l = 1$ amplitude, in the helicity formalism, is:

$$\begin{aligned} A_{l=1} &= A_{1,1} - A_{-1,-1} \\ &= \sin\theta_1 \sin\theta_2 \sin\phi. \end{aligned} \tag{4.36}$$

If the three amplitudes, A_T, A_L, and $A_{l=1}$ are included in a fit, then any possible helicity state can be modeled.

Helicity Basis Versus L/S Basis for VV Decays.

We have seen that the decay $D \to VV$ may be described in terms of three helicity amplitudes; these form the helicity basis. They may also be described in terms of amplitudes for the three possible partial waves, S, P, or D; these form a basis called the L/S basis. These two bases both form a complete basis for VV decays, and the transformation from one to the other may be derived. The P-wave amplitude has already been defined in equation (4.36). There are similar relations for S and D-wave amplitudes. With our definitions of the helicity angles and the angle ϕ, we have:

$$A_{l=0} = A_T + A_L \tag{4.37}$$

$$A_{l=2} = \sqrt{1/6}A_T - \sqrt{4/6}A_L. \tag{4.38}$$

In some references, the relative signs of A_T and A_L are opposite from the ones defined here. The difference is due to the definitions of the orientations of the decay planes of the $\overline{K}^*$ and ρ.

Breit-Wigners.

When using Lorentz invariant matrix elements, a relativistic Breit-Wigner[47] is included for each intermediate resonance:

$$\frac{-1}{m^2 - m_0^2 + i\Gamma m_0} \tag{4.39}$$

In general, each decay vertex should be multiplied by a form-factor, which describes the dependence of the coupling at a vertex on the momentum of the decay.

Blatt-Weisskopf barrier penetration factors[48] are used for each p-wave vertex:

$$\sqrt{\frac{1+(Rp_{cm0})^2}{1+(Rp_{cm})^2}} \tag{4.40}$$

where p_{cm} is the momentum of the 2-body decay in the resonance rest frame. There is no precise value of R, but generally 1 fermi or 5 GeV^{-1} is used. Any variation of the results with R will be included as a systematic uncertainty.

If the helicity formalism is being used, only the angular distribution information is included in the matrix element, and the momentum dependencies must be put in by hand. In this case, the following Breit-Wigner is used:

$$\frac{-\sqrt{\Gamma m/p_{cm}}}{m^2-m_0^2+i\Gamma m_0} \tag{4.41}$$

For the 2-body $l=1$ decays $\overline{K}^* \to K\pi$ and $\rho \to \pi\pi$, the width takes the following form:

$$\Gamma = \Gamma_0 \frac{m_0}{m}\left(\frac{p_{cm}}{p_{cm0}}\right)^3 \frac{1+(Rp_{cm0})^2}{1+(Rp_{cm})^2} \tag{4.42}$$

The width for the $l=0$ decays of the a_1 and the $K_1(1400)$ are more complicated because these decays are only quasi-two-body and so there is no single value of p_{cm} to put into the formula for the width. The width instead has the form:[49]

$$\Gamma = \Gamma_0 \frac{\phi(m)}{\phi(m_0)}. \tag{4.43}$$

The function $\phi(m)$, basically the phase space for the s-wave quasi-two-body decay, involves an integration over the matrix element of the decay:

$$\phi(m) = \int |ME|^2 d\phi_3(p_{ijk}; p_i, p_j, p_k) \tag{4.44}$$

where ϕ_n = n-body phase space, and ME is the matrix element for the sequence

$A \to VP_1$, $V \to P_2P_3$, multiplied by the Breit-Wigner for the vector:

$$ME = \varepsilon_A \cdot (\varepsilon_V \; \varepsilon_V \cdot q_V \; BW(V) \; + \; \text{symmetrization}) \tag{4.45}$$

The completeness relation for ε_A can be used after the matrix element is squared. A simple expression for ME can be obtained by evaluating ME in the rest frame of A, and using equation (4.27):

$$|ME|^2 = |(\vec{p}(P_2)(1-\xi) - \vec{p}(P_3)(1+\xi))BW(V) \; + \; \text{symmetrization}|^2 \tag{4.46}$$

where

$$\xi = \frac{(m_2^2 - m_3^2)}{p_V^2} \tag{4.47}$$

and the $\vec{p}$ are 3-momenta in the rest frame of A.

$\phi(m)$ can easily be parametrized by taking our sample of generated Monte Carlo events and using the phase space recursion relation:

$$d\phi_4(P; p_i, p_j, p_k, p_l) = d\phi_3(p_{ijk}; p_i, p_j, p_k) d\phi_2(P; p_{ijk}, p_l) dm_{ijk}^2 \tag{4.48}$$

Using $\phi_2 = p_{ijk}/m_P$ and $dm^2 = 2mdm$ and dropping constant factors, we obtain:

$$\phi(m) = \sum_{MC \; in \; dm \; bin} \frac{|ME|^2}{|p_{ijk}| m_{ijk}}. \tag{4.49}$$

We make a histogram of m_{ijk}, weighting each event by $|ME|^2/|p_{ijk}|m_{ijk}$. We fit this histogram with a cubic polynomial which becomes our parametrization of $\phi(m)$. The histogram and fit for the a_1 are shown in Fig. 4.1, which may be compared with Figure 1b in Ref. 49. The histogram and fit for the $K_1(1400)$ are shown in Fig. 4.2.

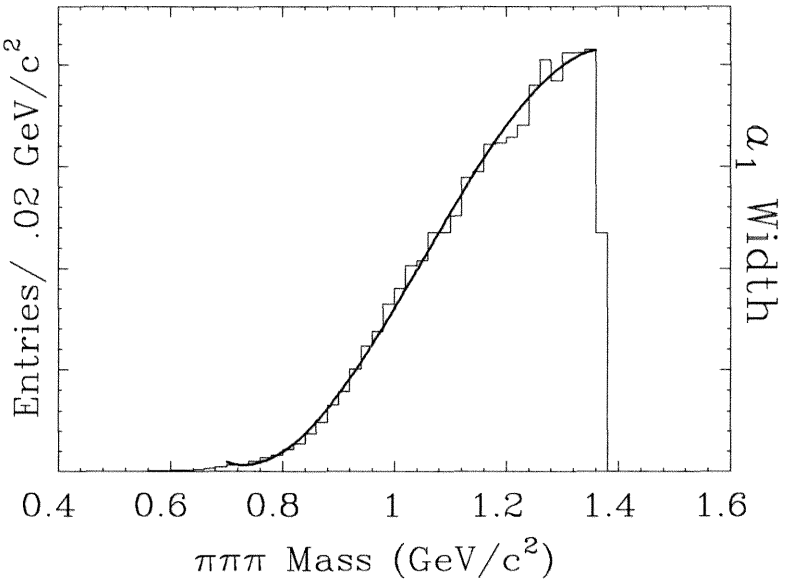

Figure 4.1 a_1 width versus mass.

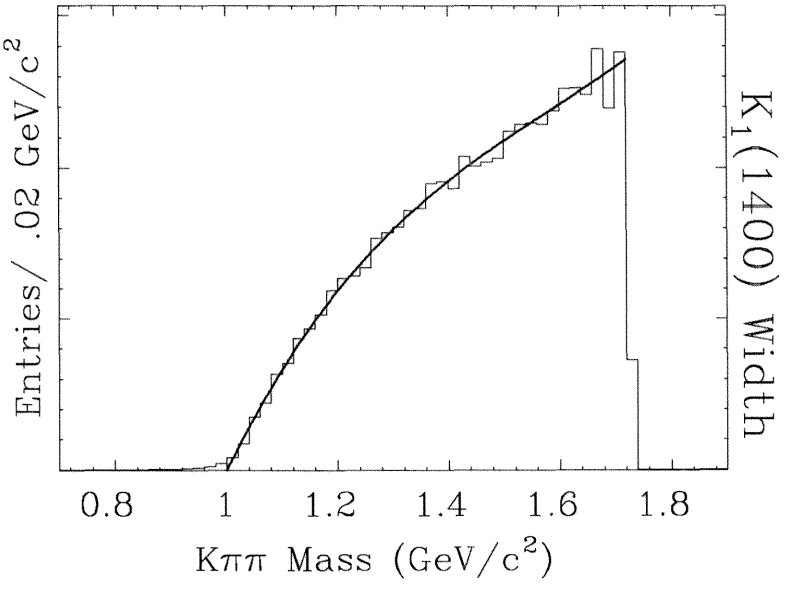

Figure 4.2 $K_1(1400)$ width versus mass.

4.11 The Decision on Which Amplitudes to Include in the Fit.

A very large number of decay modes can contribute to each final state; it is not practical to perform a fit that includes all possible decay modes simultaneously. Instead, we perform a number of fits assuming different combinations of partial waves and two-body modes. Only the lowest available partial waves yield significant contributions, and the fractions of two-body amplitudes and the four-body nonresonant amplitude remain consistent in the best fits. Nonresonant $\overline{K}\pi\pi$ and $K\rho\pi$ amplitudes also contribute. The fits are not always sensitive to the partial wave content of these three-body amplitudes.

Except for the very broad a_1 Breit-Wigner, The $\overline{K}a_1$ amplitudes are identical to the amplitudes for nonresonant $K\rho\pi$ in which the ρ and π are in a relative S-wave. Fits in which both of these amplitudes are included do not result in a significantly better likelihood; however, the fractions for each of these two amplitudes become highly uncertain, although their combined fraction remains well determined. This occurs because the relative phases for these amplitudes adjust so that there is nearly maximum constructive or destructive interference to an extent that depends very sensitively on the conditions of each particular fit. A systematic uncertainty for this effect would be both very large and difficult to quantify. Therefore, we make the assumption that this amplitude is zero, and do not include any systematic uncertainties for its possible existence, but retain the *caveat* that the presence of this one nonresonant amplitude can, only if its phase is adjusted to produce strong interference, have a large effect on the fraction of $\overline{K}a_1$. We find, however, that this assumption can be reasonably justified. Fits in which the $\overline{K}a_1$ amplitudes are replaced by the three-body amplitude result in a significantly poorer likelihood. The

differences in $-\ln \mathcal{L}$ will be specified in each case. Also, the fractions of $K\rho\pi$ in other partial waves are relatively small.

4.12 General Discussion of Systematic Errors and Upper Limits.

Systematic uncertainties from several sources were considered and estimated by performing many fits under varying conditions. The total systematic error for each fraction is obtained by summing the uncertainties from each source in quadrature. In this section, we discuss general methods used to estimate systematic errors and upper limits. Specific systematic errors and upper limits will be listed in later chapters.

Uncertainties Due to the Background Parametrization.

In the fits to the recoil mass plots, one of the parameters is the fraction of events in the signal. Uncertainties in $R_{S/B}$ are taken into account by allowing this fraction to vary within errors while minimizing $-\ln \mathcal{L}$. This slightly increases the errors returned by MINUIT.

The statistical errors in the fractions of the functions in $\mathcal{F}_B$ are taken into account by fitting $\mathcal{F}_S$ and $\mathcal{F}_B$ simultaneously. Again, this increases the errors returned by MINUIT slightly compared to fits in which $\mathcal{F}_B$ is fixed.

The systematic uncertainties due to varying the functions used for $\mathcal{F}_B$ are small. Even using only a constant term changes the results only slightly.

Uncertainties Due to the Form of the Completeness Relation.

For the central values of the fractions and phases, equation (4.25) is used for intermediate spin 1 resonances. A systematic uncertainty due to the theoretical

uncertainty on the parameterization of the amplitudes is obtained by performing fits in which equation (4.27) is used for some or all of the intermediate resonances.

Uncertainties Due to Varying the Parameter R in eq. (4.40).

A systematic uncertainty is included to characterize the variation of the results as the form-factors are varied. Several fits are performed in which the parameter R in eq. (4.40) is given different values for different resonances.

Uncertainties in the Parameters of the Intermediate Resonances.

Several fits were tried in which the masses and widths of the intermediate resonances were varied within their uncertainties. A systematic uncertainty in the fractions was assigned accordingly. The largest uncertainties are in the case of the a_1. We assume 1.26 GeV/c^2 for the mass of the a_1, and 0.4 GeV/c^2 for the width.[50] We include in the systematic uncertainties the effect of varying the mass between 1.2 and 1.3 GeV/c^2, and the width between 0.3 and 0.5 GeV/c^2.

Uncertainties Due to Monte Carlo Modeling.

For this analysis, it is very important that the Monte Carlo properly model the relative efficiency throughout the phase space. A systematic uncertainty due to this modeling is estimated by doing several fits with various cuts on two-body masses and track momenta. The regions cut out were treated as if the detector had zero efficiency. If there are differences in the relative efficiency between the Monte Carlo and the real detector, the fractions obtained from the fits will vary accordingly. There also is a variation due to statistics, so these estimates are conservative.

Uncertainties Due to Monte Carlo Statistics.

It is necessary to check that we have a statistically sufficient Monte Carlo sample for the normalizations. This is done by dividing the Monte Carlo sample into

several smaller samples and performing a fit with each sample. The amplitudes with narrow resonances such as a K^* have a larger uncertainty because a relatively small number of Monte Carlo events fall into the regions where these amplitudes are large. However, the uncertainties from Monte Carlo statistics are always relatively small.

Uncertainties Due to Detector Resolution.

The two-body mass resolutions are typically 5 MeV; however, the p.d.f. does not take this into account. Since the narrowest resonance, the K^*, (with the exception of the ω, for which the detector resolution is accounted for in the p.d.f.) is much broader than this resolution, any systematic uncertainty from this source should be small. This is checked by performing a fit on the data with the resolution artificially increased.

Uncertainties Due to the Possible Presence of Additional Amplitudes.

Several fits are tried, with extra two and three-body amplitudes. The details of which extra amplitudes are included are discussed for each case in later chapters.

Upper Limits.

Amplitudes which do not yield significant contributions remain small in all fits with good likelihood. Therefore, we can set meaningful upper limits. In addition to including the statistical errors in the calculation of the limit, we include any systematic variations in the fractions obtained in different fits. The details of which fits are considered are discussed for each case in later chapters.

4.13 Guidelines for Reproducing the Distributions in Phase Space.

Using the results for the fractions and phases of decay modes in later chapters, and the formalism in this chapter, the distributions of events in phase space may be reproduced.

The master equation to use is equation (4.11). The Lorentz-invariant amplitudes are shown in Table 4.1. The decay chains specified in later chapters must be carefully matched to these amplitudes. If two particles in the chain are switched, an erroneous minus sign may be introduced. For $\overline{K}^*\rho$ decays, the helicity amplitudes in equations (4.32) and (4.33) are used. It is important to use the correct definitions for the angles in these equations. Finally, the Breit-Wigners are given in equations (4.39) and (4.41).

5
$D^0 \to K^-\pi^+\pi^+\pi^-$.

The two-body decay modes that can contribute to the $K^-\pi^+\pi^+\pi^-$ final state include $K^-a_1^+$, $\overline{K}^{*0}\rho^0$, $K_1(1270)^-\pi^+$ and $K_1(1400)^-\pi^+$. There are two three-body modes which can contribute, $\overline{K}^{*0}\pi^+\pi^-$ and $K^-\rho^0\pi^+$.

The recoil mass plot for the $D^0 \to K^-\pi^+\pi^+\pi^-$ final state is shown in Fig. 5.1. There are 1281 ± 45 events above background. The average ratio of signal to background in the region of recoil mass from 1.854 to 1.876 GeV is 3.1. The branching ratio has previously been determined by Mark III to be $9.1 \pm 0.8 \pm 0.8\%$, as discussed in chapter 3. This final state is by far the one with the most statistical power.

Projections of the background p.d.f. $\mathcal{F}_B$ onto sideband events are shown in Fig. 5.2. $\mathcal{F}_B$ consists of about 80% phase space, with the remainder about equally consisting of $\overline{K}^{*0}\pi^+\pi^-$ and $K^-\rho^0\pi^+$. Projections of the total p.d.f. $\mathcal{F}$ onto events in the signal region are shown in Fig. 5.3. The solid lines, representing the projections of $\mathcal{F}$, are superimposed on histograms of the events. The dip near 0.5 GeV in the $(\pi^+\pi^-)_{\rm lo}$ mass plot is due to the rejection of $\pi^+\pi^-$ combinations which have a high probability of originating from a K_s decay.

For the events in the signal region, clear $\overline{K}^{*0}$ and ρ^0 peaks are visible and are well

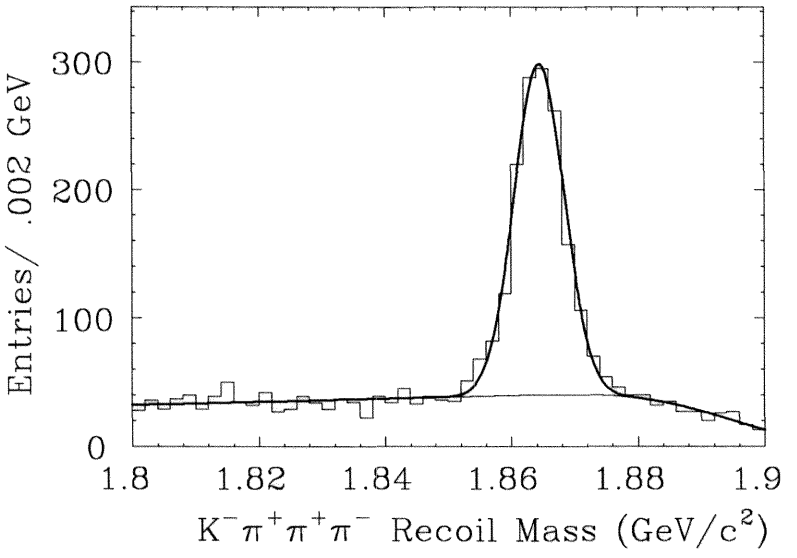

Figure 5.1 Signal for $D^0 \to K^-\pi^+\pi^+\pi^-$.

reproduced by the fit. A peak at the $K_1(1270)$ mass is visible in the $K^-(\pi^+\pi^-)_{\rm lo}$ mass plot.

The enhancement at low $K^-\pi^-$ mass is characteristic of the $K^-a_1^+$ amplitude, and is due to the longitudinal polarization of the a_1. We illustrate this effect in Fig. 5.4. The small vertical arrows indicate the polarization of the a_1 and ρ. The relative orbital angular momentum at each vertex is shown. To conserve angular momentum, the a_1 must be longitudinally polarized. Since the a_1 decays to $\rho\pi$ in an S-wave, the spin of the ρ is parallel to the spin of the a_1. Therefore, in the decay of the ρ, the π^- tends to be produced in a forward or backward direction with respect to the direction of the K^-, producing a distribution with an enhancement at low $K^-\pi^-$ mass.

The presence of the transverse $\overline{K}^{*0}\rho^0$ amplitude leads to angular correlations

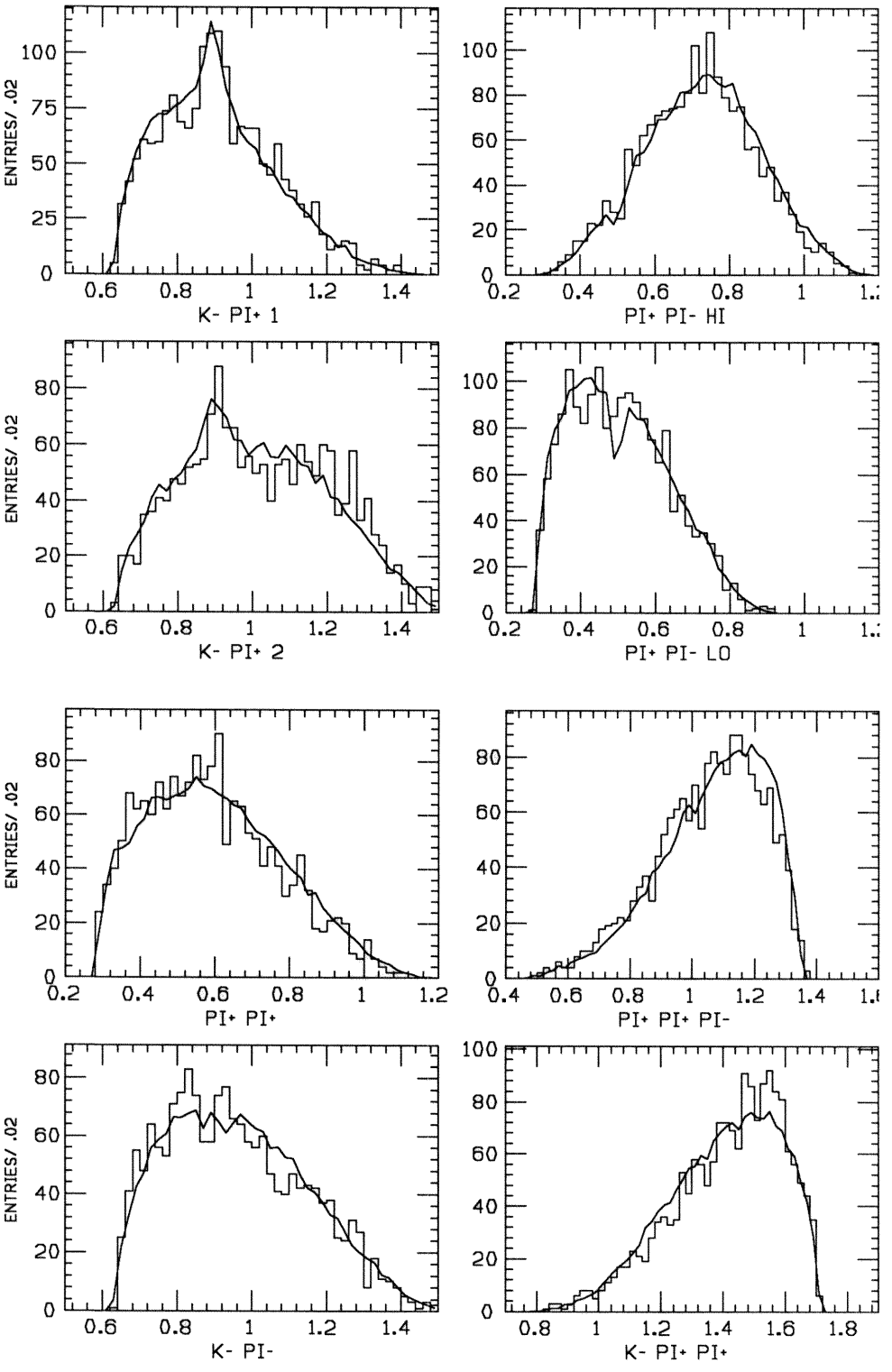

Figure 5.2 Projections of $\mathcal{F}_B$ onto events outside of the signal region.

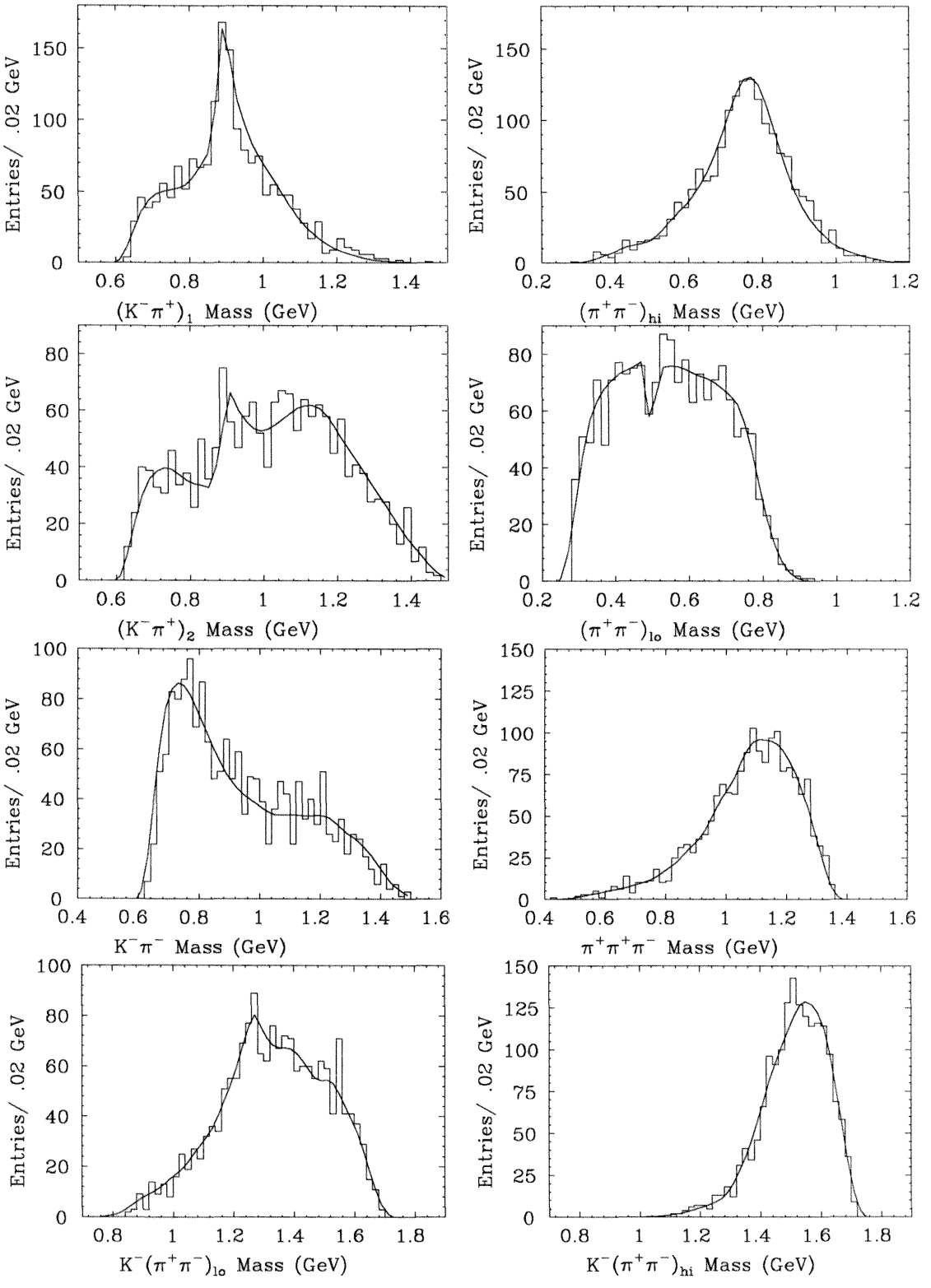

Figure 5.3 Projections of $\mathcal{F}$ onto events in the signal region.

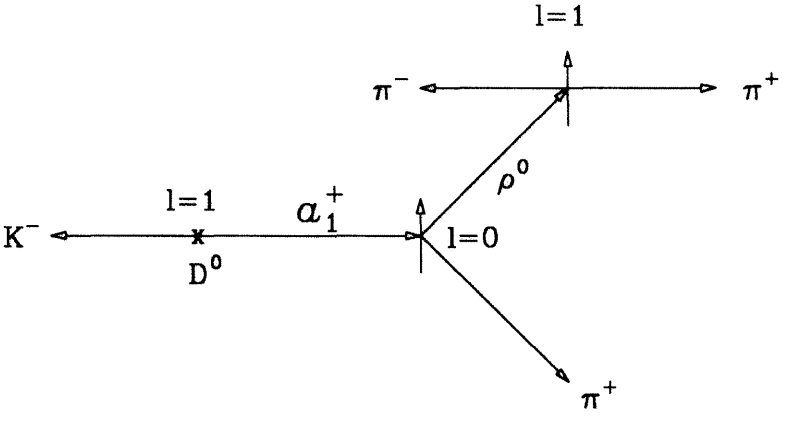

Figure 5.4 Illustration of $K^- a_1^+$ amplitude.

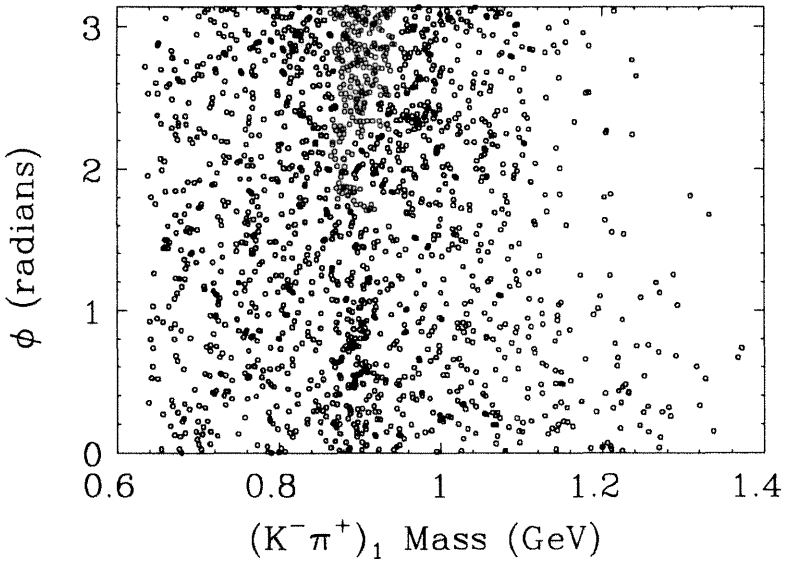

Figure 5.5 Illustration of the transverse polarization of the $\overline{K}^{*0}\rho^0$ amplitude.

Table 5.1 Results for $D^0 \to K^-\pi^+\pi^+\pi^-$.

Amplitude	Relative Fraction f_j	Phase α_j	Branching Ratio (%)[a]
4-Body Nonresonant	$0.242 \pm 0.025 \pm 0.06$	-1.07 ± 0.08	$2.2 \pm 0.3 \pm 0.6$
$\overline{K}^{*0}\rho^0$ Transverse (S-wave)	$0.142 \pm 0.016 \pm 0.05$	-1.39 ± 0.09	$1.9 \pm 0.3 \pm 0.7$
$K^- a_1(1260)^+$	$0.492 \pm 0.024 \pm 0.08$	0.0	$9.0 \pm 0.9 \pm 1.7$
$K_1(1270)^-\pi^+$	$0.066 \pm 0.019 \pm 0.03$	0.71 ± 0.25	$1.8 \pm 0.5 \pm 0.8$
$\overline{K}^{*0}\pi^+\pi^-$	$0.140 \pm 0.018 \pm 0.04$	3.07 ± 0.09	$1.9 \pm 0.3 \pm 0.6$
$K^-\rho^0\pi^+$	$0.084 \pm 0.022 \pm 0.04$	-0.30 ± 0.13	$0.8 \pm 0.2 \pm 0.4$

[a] Reference 55.

between $\overline{K}^{*0}$ and ρ^0 decays. We show an example in Fig. 5.5, which is a scatter plot of $(K^-\pi^+)_1$ mass vs ϕ, where ϕ is the angle between the $\overline{K}^{*0}$ and ρ^0 decay planes as seen from the D^0 rest frame, as discussed in chapter 4. In the $\overline{K}^{*0}$ band, an enhancement near ϕ=0 and a larger enhancement near $\phi = \pi$ are visible. The transverse $\overline{K}^{*0}\rho^0$ amplitude, which is proportional to $\cos\phi$, accounts for this distribution. Since the sign of this amplitude reverses from $\phi = 0$ to $\phi = \pi$, there is more constructive interference near $\phi = \pi$.

The results of the best fit found to the $D^0 \to K^-\pi^+\pi^+\pi^-$ final state are shown in Table 5.1. We included one $\overline{K}^{*0}\pi^+\pi^-$ amplitude in which the $\overline{K}^{*0}\pi^-$ system is in a pseudoscalar state, and one $K^-\rho^0\pi^+$ amplitude in which the $K^-\rho^0$ system is in an axial vector state. The fractions obtained for the three-body modes do not depend strongly on the relative partial waves assumed for the vector and two pseudoscalar mesons. In general, the best fits had one of the following amplitudes: $\overline{K}^{*0}\pi^+\pi^-$, where the $\overline{K}^{*0}\pi^-$ system is in a pseudoscalar state, or the $\pi^+\pi^-$ system is in a scalar state, or the $\overline{K}^{*0}\pi^+$ system is in an axial vector state; and one of the following amplitudes: $K^-\rho^0\pi^+$, where the $K\rho^0$ system is in an axial vector state,

Table 5.2 Upper limits for $D^0 \to K^-\pi^+\pi^+\pi^-$.

Amplitude	Branching Ratio (%)[a]
$\overline{K}^{*0}\rho^0$ Longitudinal (S-wave)	< 0.3
$\overline{K}^{*0}\rho^0$ (P-wave)	< 0.3
$K^-a_2(1320)^+$	< 0.6
$K^*(1415)^-\pi^+$	< 1.2
$K_1(1400)^-\pi^+$	< 1.2

[a] Reference 55.

or the $\rho^0\pi^-$ system is in a pseudoscalar state, or the $K^-\pi^+$ system is in a vector state.

The observation that in the helicity basis the $\overline{K}^{*0}\rho^0$ amplitude is purely transversely polarized implies that in the L/S basis the amplitude is a mixture of S-wave and D-wave. Transforming the result in Table 5.1 into the L/S basis, we find:

$$\begin{aligned} B(D^0 \to \overline{K}^{*0}\rho^0 \text{ S} - \text{wave}) &= 3.8 \pm 0.6 \pm 1.4\% \\ B(D^0 \to \overline{K}^{*0}\rho^0 \text{ D} - \text{wave}) &= 1.9 \pm 0.3 \pm 0.7\%. \end{aligned} \tag{5.1}$$

Although the branching ratios for each of these partial waves is large, there is a large amount of destructive interference between them, since the D-wave amplitude must completely cancel the longitudinal component of the S-wave amplitude in order for the total $\overline{K}^{*0}\rho^0$ amplitude to be purely transverse.

Table 5.2 contains upper limits for the branching ratios of several decay modes which do not yield significant contributions to this final state. The upper limit for each decay mode takes into account statistical errors, as well as any variations in the fractions obtained as the partial waves of the three-body decay modes are changed, or as amplitudes for other decay modes in Table 5.2 are included.

The decay chains to be compared with Table 4.1 are shown in Table 5.3. The

Table 5.3 $K^-\pi^+\pi^+\pi^-$ decay chains.

$D^0 \to K^- a_1^+$	$a_1^+ \to \rho^0\pi^+$	$\rho^0 \to \pi^-\pi^+$	
$D^0 \to K_1(1270)^-\pi^+$			
$K_1(1270)^- \to$	$\rho^0 K^-$	$\rho^0 \to \pi^+\pi^-$	$f_j = 0.020, \alpha_j = 0.71$
	$\overline{K}_0^*(1430)^0\pi^-$	$\overline{K}_0^{*0} \to K^-\pi^+$	$f_j = 0.018, \alpha_j = 0.75$
	$\overline{K}^{*0}\pi^+$	$\overline{K}^{*0} \to K^-\pi^+$	$f_j = 0.007, \alpha_j = 3.55$
$D^0 \to (\overline{K}^{*0}\pi^-)_P\pi^+$	$(\overline{K}^{*0}\pi^-)_P \to \overline{K}^{*0}\pi^-$	$\overline{K}^{*0} \to K^-\pi^+$	
$D^0 \to (\rho^0 K^-)_A\pi^+$	$(\rho^0 K^-)_A \to \rho^0 K^-$	$\rho^0 \to \pi^+\pi^-$	

Table 5.4 Fractions of the $K^-\pi^+\pi^+\pi^-$ final state as observed by different experiments.

Channel	Mark III	SLAC-LBL[a]	ACCMOR[b]	ARGUS[c]	E691[d]
$\overline{K}^{*0}$ X	$0.207 \pm 0.020 \pm 0.03$			0.39 ± 0.03	$0.26 \pm 0.04 \pm 0.03$
ρ^0 X	$0.855 \pm 0.032 \pm 0.03$			0.86 ± 0.10	$1.06 \pm 0.06 \pm 0.09$
$\overline{K}^{*0}\rho^0$	$0.142 \pm 0.016 \pm 0.05$	$0.1^{+0.11}_{-0.10}$	0.5 ± 0.2	0.35 ± 0.06	
$K^-\rho^0\pi^+$	$0.084 \pm 0.022 \pm 0.04$	$0.85^{+0.11}_{-0.22}$	0.2 ± 0.2	0.51 ± 0.08	
$K^- a_1^+$	$0.492 \pm 0.024 \pm 0.08$			0.51 ± 0.08[e]	
$\overline{K}^{*0}\pi^+\pi^-$	$0.140 \pm 0.018 \pm 0.04$	$0.0^{+0.2}_{-0.0}$	< 0.18	0.04 ± 0.04	
$K^-\pi^+\pi^+\pi^-$	$0.242 \pm 0.025 \pm 0.06$	$0.05^{+0.11}_{-0.05}$		0.11 ± 0.06	

[a] Reference 51. [b] Reference 52. [c] Reference 53. [d] Reference 54.

[e] In the ARGUS analysis, angular distributions of ρ^0 decays outside the $\overline{K}^{*0}$ bands were examined. The $K^-\rho^0\pi^+$ component was found to be consistent with being entirely $K^- a_1^+$.

breakdown for fractions and phases of the three decay modes of the $\overline{K}_1(1270)$ is also shown. The relative fractions of the three decay modes are constrained within errors to the Particle Data Group values of the branching ratios of the $\overline{K}_1(1270)$, times the appropriate isospin Clebsch-Gordan coefficients. The relative phases are allowed to vary.

Comparison With Results From Other Experiments.

In previous analyses,[51-54] the resonant substructure of $D^0 \to K^-\pi^+\pi^+\pi^-$ decays was measured by fitting one-dimensional mass plots to obtain the fraction of $\overline{K}^{*0}\rho^0$, inclusive $\overline{K}^{*0}$, inclusive ρ^0, and nonresonant four-body. The advantage of the approach used here is that the amplitudes provide a complete description of the decay modes in the five-dimensional phase space and all the information available in the event is used in the fit, making it possible to fit to a general set of amplitudes, include interference, and obtain fractions for exclusive decay modes. A comparison with results from other experiments is shown in Table 5.4. We calculate the total $\bar{K}^*$ and ρ content from our fits by summing the appropriate exclusive fractions and taking into account interference between the decay modes. From a similar calculation, we find that the sum of the two-body amplitudes is 76%.

Checks on the Goodness of the Fit.

To check that the method described here is self-consistent as implemented in our subroutines, we generate Monte Carlo events distributed according to the results of the fit in Table 5.1. This is done by a random number throw-away method, starting with a sample of phase space generated events. For each event, $x = S/S_{max}$ is calculated, where $\mathcal{F}_S = \epsilon\phi S$ (see chapter 4), and S_{max} is the maximum value of S in phase space. A random number between 0 and 1 is generated, and if the number is less than x, the event is kept. Fitting the resulting sample of events, the results are consistent with the input fractions and phases within statistical errors.

This work was done in collaboration with Allen Mincer.[56] Although our methods differ considerably in the details, we always found that we obtained the same results if we performed fits using the same amplitudes. This has provided a rigorous external check for both of us.

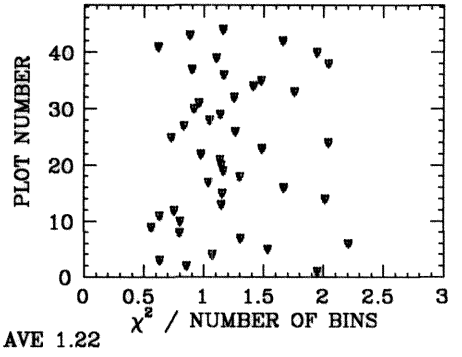

Figure 5.6 χ^2 from the fit to the data.

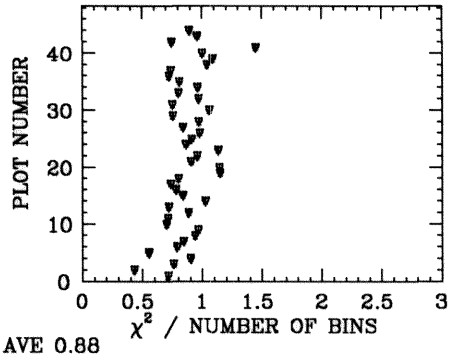

Figure 5.7 χ^2 from the fit to the Monte Carlo.

In addition to finding a maximum of the p.d.f., it is necessary to check that this maximum describes the data well. To do this, we plot 44 projections of the p.d.f. superimposed on histograms of the data and calculate χ^2 for each projection. The first 8 plots are the mass plots already shown; the others are plots of additional invariant masses and angular distributions. The χ^2 from the fit to the data are shown in Fig. 5.6, and the χ^2 from the fit to the Monte Carlo are shown in Fig. 5.7. Although the quality of the fit to the data isn't as good as that for the Monte Carlo, the χ^2 per degree of freedom is adequate.

Systematic Uncertainties.

Systematic uncertainties from the following sources are listed in Table 5.5:

Table 5.5 Systematic Uncertainties on the fractions.

Amplitude	A	B	C	D	E	F	G
4-Body Nonresonant	4.0	1.0	2.0	3.0	0.5	0.5	2.0
$\overline{K}^{*0}\rho^0$	0.2	3.0	0.5	2.0	1.0	0.5	2.0
$K^-a_1^+$	1.0	4.0	2.0	3.0	0.5	0.5	5.0
$K_1(1270)^-\pi^+$	0.8	1.0	1.0	2.0	0.5	0.5	2.0
$\overline{K}^{*0}\pi^+\pi^-$	1.0	1.0	1.0	2.0	0.5	0.5	3.0
$K^-\rho^0\pi^+$	1.0	1.0	1.0	3.0	0.5	0.5	3.0

A) Uncertainties due to changing the form of the propagator for intermediate spin 1 resonances.

B) Uncertainties due to varying the parameter R in the Blatt-Weisskopf form-factors.

C) Uncertainties due to uncertainties in the masses and widths of the intermediate resonances.

D) Uncertainties due to Monte Carlo modeling.

E) Uncertainties due to Monte Carlo statistics.

F) Uncertainties due to detector resolution.

G) Uncertainties due to the possible presence of additional amplitudes. This uncertainty includes any variations in the fractions obtained as the partial waves of the three-body decay modes are changed, or as amplitudes for decay modes in Table 5.2 are included.

6
$D^+ \to \overline{K}^0\pi^+\pi^+\pi^-$.

The two-body decay modes which can contribute to the $\overline{K}^0\pi^+\pi^+\pi^-$ final state include $\overline{K}^0 a_1^+$, $\overline{K}_1(1270)^0\pi^+$ and $\overline{K}_1(1400)^0\pi^+$. No $\overline{K}^*\rho$ mode can contribute to this final state. There are two three-body modes which can contribute, $K^{*-}\pi^+\pi^+$ and $\overline{K}^0\rho^0\pi^+$.

The recoil mass plot is shown in Fig. 6.1. There are 209 ± 20 events above background. The average ratio of signal to background in the region of recoil mass from 1.858 to 1.880 GeV is 1.6. The branching ratio has previously been determined by Mark III to be $B(D^+ \to \overline{K}^0\pi^+\pi^+\pi^-) = 6.6\pm1.5\pm0.5\%$, as discussed in chapter 3.

Although there are not as many events as for the $D^0 \to K^-\pi^+\pi^+\pi^-$ final state, the backgrounds are still reasonably low, and the resonant substructure is expected to be relatively simple. The main features of the resonant substructure of this final state can be seen in the scatter-plots in Fig. 6.2. The notable features are a K^{*-} band, with clusters at high and low $(\pi^+\pi^-)_2$ mass, and a ρ^0 band, with clusters at high and low $(\pi^+\pi^-)_{\text{high}}$ mass. In Fig. 6.3, these features are reproduced with Monte Carlo events generated according to the results of a fit to the data, and include contributions from $\overline{K}^0 a_1^+$, $\overline{K}_1(1400)^0\pi^+$, and four-body nonresonant decays.

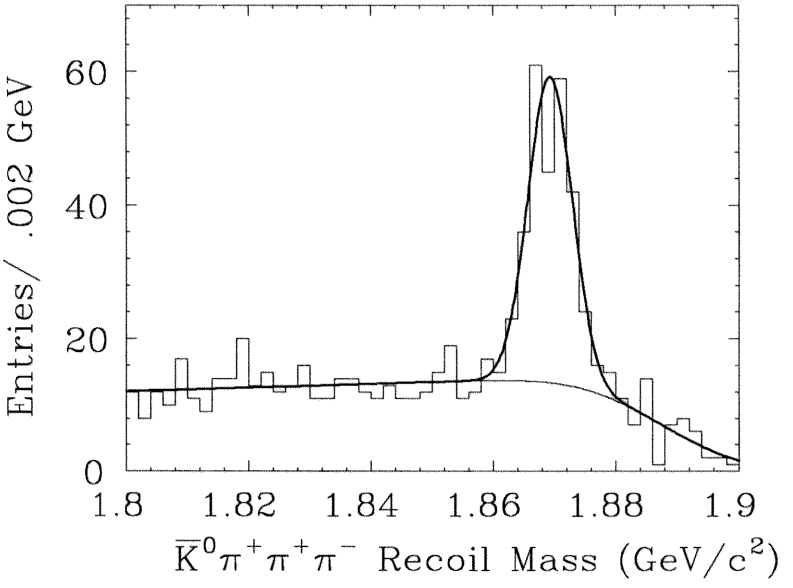

Figure 6.1 Signal for $D^+ \to \overline{K}^0\pi^+\pi^+\pi^-$.

These features can be understood with the aid of the diagrams in Figs. 6.4 and 6.5. They are analogous to the enhancements at low $K^-\pi^-$ mass in $D^0 \to K^-a_1^+$ decays. The small vertical arrows indicate the spins of the axial-vector mesons a_1 and $\overline{K}_1(1400)$, and the vector mesons ρ and $\overline{K}^*$. The relative orbital angular momentum at each vertex is shown. Because of the longitudinal polarization of the axial-vector mesons and the subsequent polarization of the vector mesons, the vector mesons tend to decay in a forward or backward direction with respect to the direction of the axial-vector meson, producing distributions with enhancements at low and high $K\pi$ mass in the case of the a_1 and with enhancements at low and high $\pi\pi$ mass in the case of the $\overline{K}_1(1400)$.

For $\overline{K}^0a_1^+$ decays, there are two decay chains:

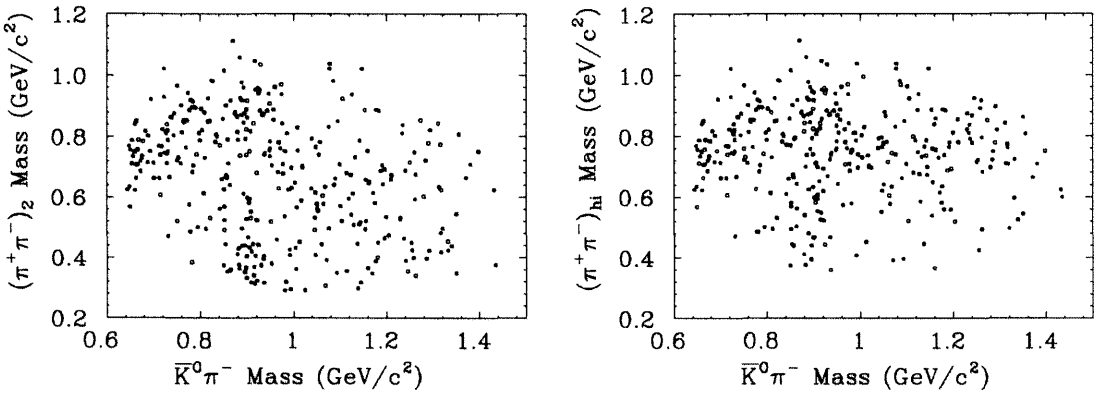

Figure 6.2 Scatter plots for data events.

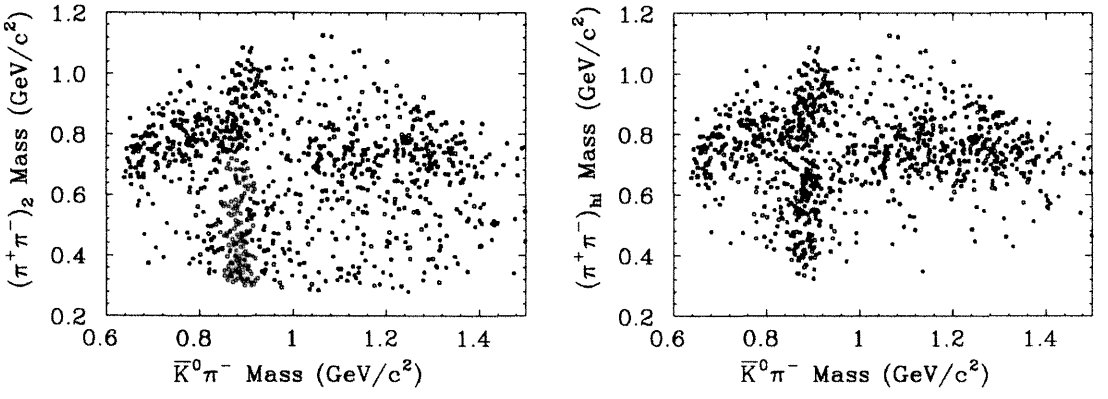

Figure 6.3 Scatter plots for mc events.

$$\begin{aligned} D^+ \to \overline{K}^0 a_1^+,\ a_1^+ \to \rho^0\pi_1^+,\ \rho^0 \to \pi_2^+\pi^- \\ \to \rho^0\pi_2^+,\ \rho^0 \to \pi_1^+\pi^- \end{aligned} \tag{6.1}$$

Since both decay chains produce enhancements at high and low $\overline{K}^0\pi^-$ mass, the effect is very clear. For the $\overline{K}_1(1400)^0\pi^+$, there are also two decay chains:

$$\begin{aligned} D^+ \to \overline{K}_1(1400)^0\pi_1^+,\ \overline{K}_1(1400)^0 \to K^{*-}\pi_2^+ \\ \to \overline{K}_1(1400)^0\pi_2^+,\ \overline{K}_1(1400)^0 \to K^{*-}\pi_1^+ \end{aligned} \tag{6.2}$$

However, in this case the effect is less clear, because the two possible decay chains do not produce the same distribution in one unique variable.

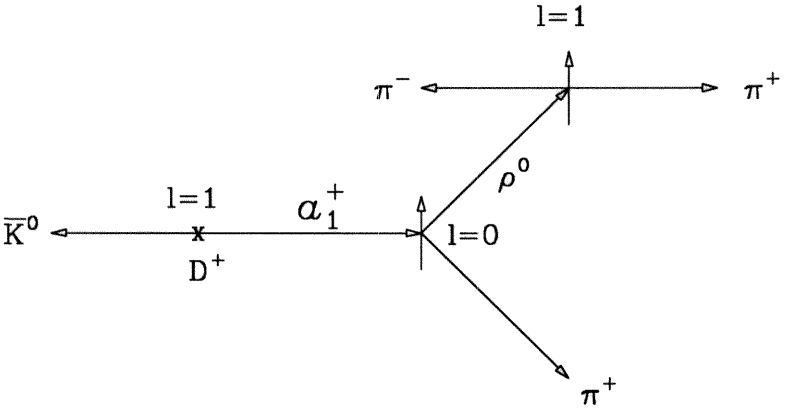

Figure 6.4 Illustration of $\overline{K}^0 a_1^+$ amplitude.

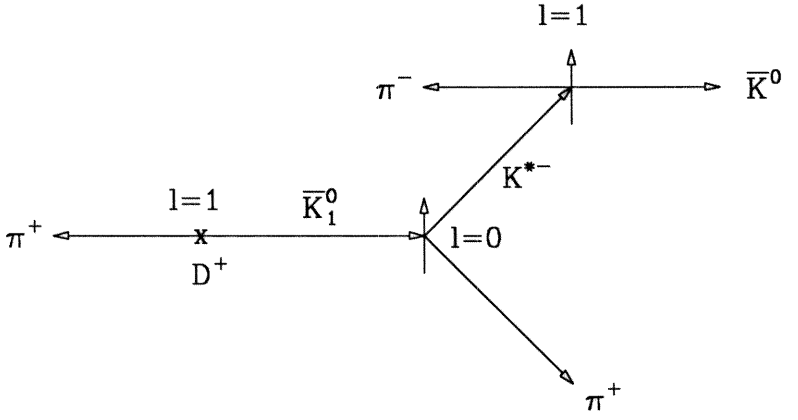

Figure 6.5 Illustration of $\overline{K}_1(1400)^0\pi^+$ amplitude.

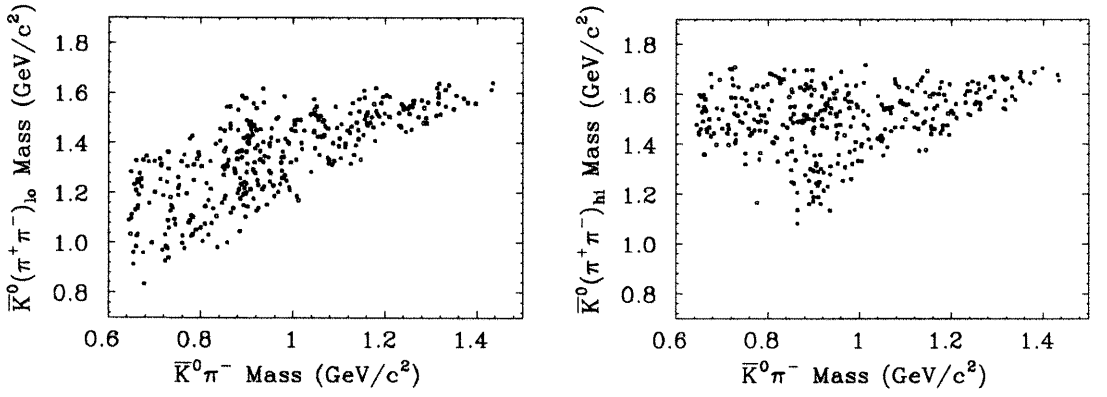

Figure 6.6 Scatter plots for data events.

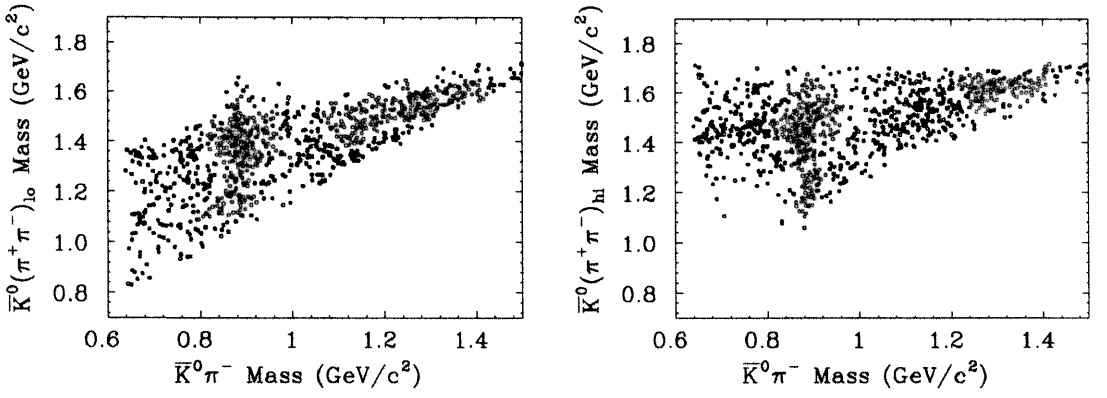

Figure 6.7 Scatter plots for mc events.

Although the $\overline{K}_1(1400)^0$ is very broad, with a width of 0.184 GeV/c^2, clustering of the K^{*-} band in the $\overline{K}_1(1400)^0$ regions is visible in the scatter-plots in Fig. 6.6. A cluster of K^{*-} events can also be seen extending into the low $\overline{K}^0(\pi^+\pi^-)_{\text{high}}$ region, in contrast to the rest of the plot. This cluster, a reflection of the $\overline{K}_1(1400)^0$ in the $\overline{K}^0(\pi^+\pi^-)_{\text{low}}$ plot, cannot be produced by any known amplitude other than the $\overline{K}_1(1400)^0\pi^+$ amplitude. Scatter plots of Monte Carlo data are shown in Fig. 6.7.

Projections of $\mathcal{F}_B$ onto sideband events are shown in Fig. 6.8. The fit in this case is exceptionally good. $\mathcal{F}_B$ consists of about 80% phase space, and 20% $\overline{K}^0\rho^0\pi^+$. Projections of $\mathcal{F}$ onto events in the signal region are shown in Fig. 12. $\mathcal{F}_B$ is also

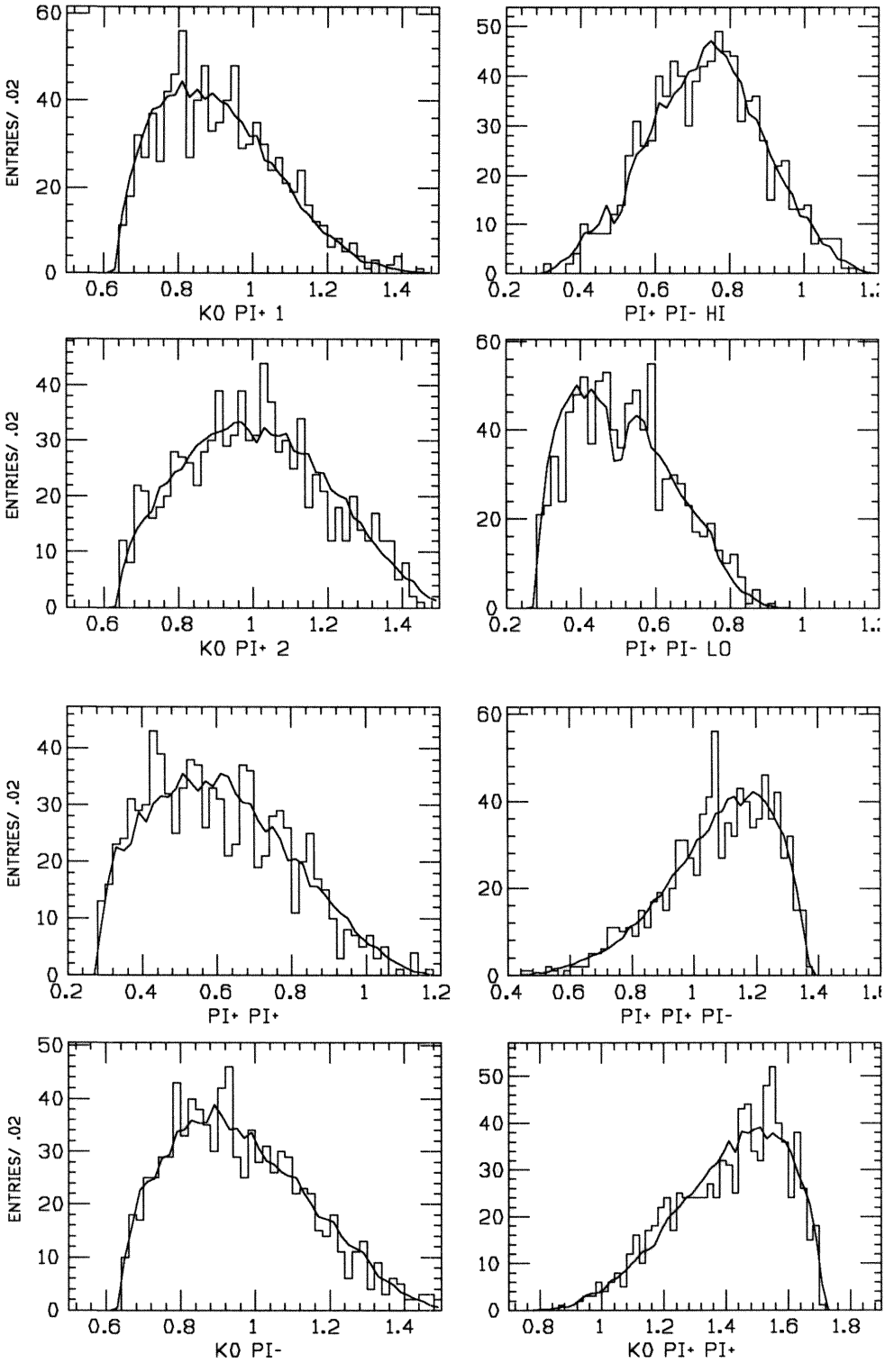

Figure 6.8 Projections of $\mathcal{F}_B$ onto sideband events.

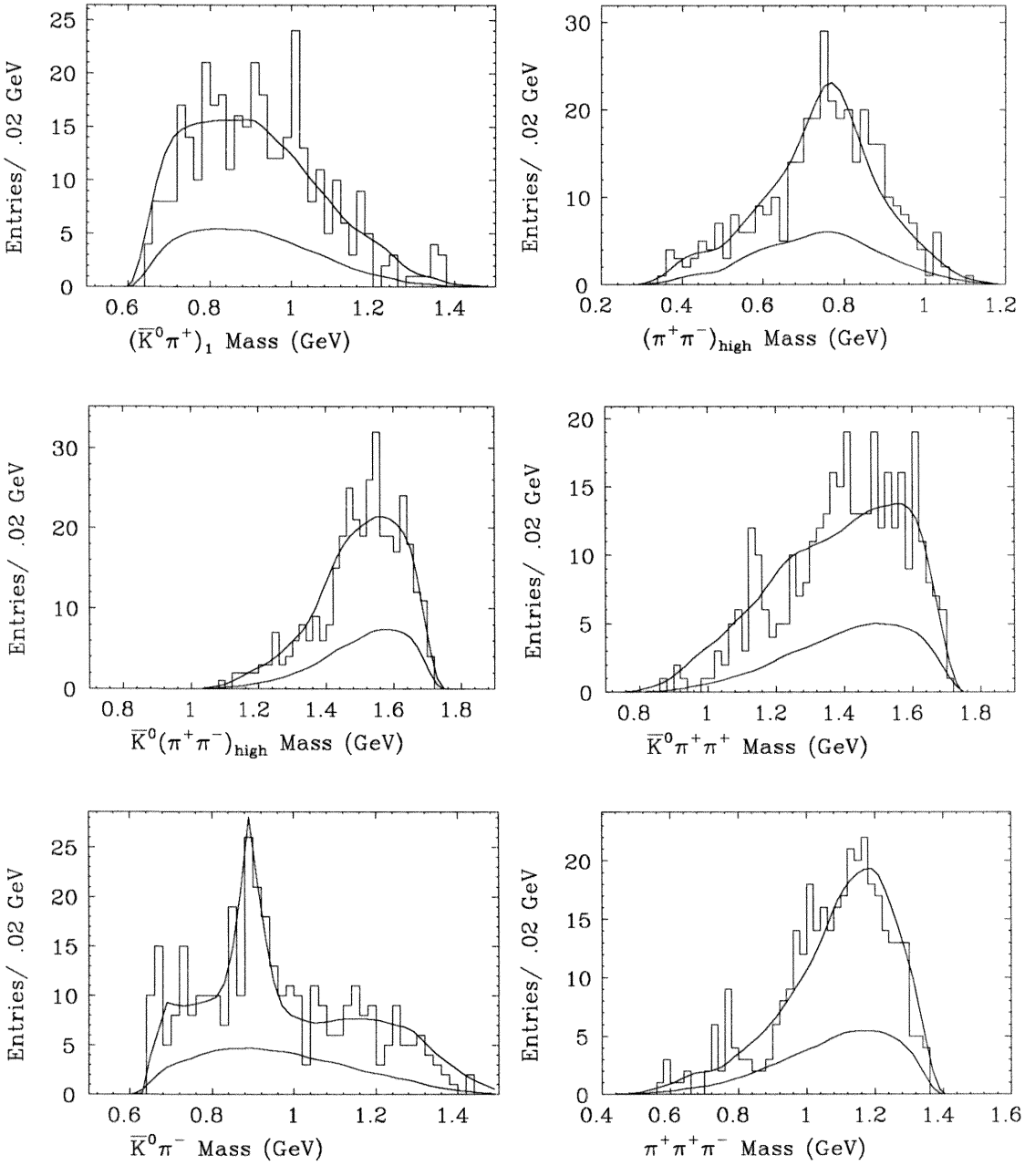

Figure 6.9 Projections of $\mathcal{F}_S$ onto events in the signal region.

Table 6.1 Results for $D^+ \to \overline{K}^0\pi^+\pi^+\pi^-$.

Amplitude	Fraction (%)	Phase	Branching Ratio (%)
4-Body Nonresonant	$17.0 \pm 5.6 \pm 10.0$	1.09 ± 0.28	$1.1 \pm 0.4 \pm 0.7$
$K^-a_1^+$	$53.9 \pm 5.7 \pm 7.0$	.0	$7.1 \pm 1.8 \pm 1.1$
$\overline{K}_1(1400)^0\pi^+$	$27.7 \pm 4.7 \pm 8.0$	-0.07 ± 0.32	$4.1 \pm 1.2 \pm 1.2$

Table 6.2 $\overline{K}^0\pi^+\pi^+\pi^-$ decay chains.

$D^+ \to \overline{K}^0 a_1^+$	$a_1^+ \to \rho^0\pi^+$	$\rho^0 \to \pi^-\pi^+$
$D^+ \to \overline{K}_1(1400)^0\pi^+$	$\overline{K}_1(1400)^0 \to K^{*-}\pi^+$	$K^{*-} \to \overline{K}^0\pi^-$

drawn, scaled down to the background level.

The results of the fit are shown in Table 6.1. Only three amplitudes are required to fit the major features of the resonant substructure. In contrast to the fits in the $D^0 \to K^-\pi^+\pi^+\pi^-$ final state, no three-body amplitude yields a significant contribution. As with the $D^0 \to K^-\pi^+\pi^+\pi^-$ mode, we assume that the three-body mode in which a ρ^0 and a π^+ are in an axial-vector state does not contribute. When this mode is added to a fit with $\overline{K}^0 a_1^+$, $-\ln\mathcal{L}$ improves by only 2.0. When the $\overline{K}^0\rho^0\pi^+$ amplitude is substituted for the $\overline{K}^0 a_1^+$ term, $-\ln\mathcal{L}$ gets worse by 22.7.

The decay chains, to be compared with Table 4.1, are shown in Table 6.2.

Fig. 6.10 is a plot of χ^2 for 44 different projections. The average χ^2 for these plots is 1.05, compared to 1.22 for the $D^0 \to K^-\pi^+\pi^+\pi^-$ fit. Although the $\overline{K}^0\pi^+\pi^+$ plot has a mysterious peak near 1.15, the χ^2 for this plot is 44.5 for 60 bins. No decay modes in the D Monte Carlo model cause such a background peak. No correlation was found between the events in the peak and a number of variables, such as beam-fit probability, $\overline{K}^0$ decay length, track momentum, other invariant

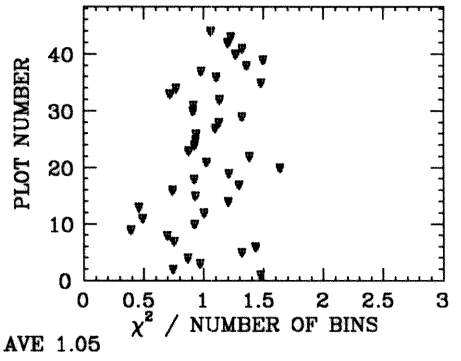

Figure 6.10 χ^2 from the fit to the data.

Table 6.3 Limits for $D^+ \to \overline{K}^0\pi^+\pi^+\pi^-$.

Amplitude	Branching Ratio (%)
$\overline{K}_1(1270)^0\pi^+$	< 1.1
$K^{*-}\pi^+\pi^+$	< 1.3
$\overline{K}^0\rho^0\pi^+$	< 0.4
$\overline{K}^*(1415)^0\pi^+$	< 0.7
$\overline{K}^0 a_2(1320)^+$	< 0.8

masses, etc. Also, performing the fit while excluding events below 1.25 GeV/c^2 in $\overline{K}^0\pi^+\pi^+$ mass yields consistent results. We conclude that the peak is consistent with being a statistical fluctuation.

Table 6.3 contains upper limits for several decay modes which do not yield significant fractions when included in the fits. The upper limit for each decay mode takes into account statistical errors, as well as any variations in the fractions obtained as amplitudes for other decay modes in Table 6.3 are included.

Systematic Uncertainties on the Fractions.

Systematic uncertainties from the following sources are listed in Table 6.4:

A) Uncertainties due to changing the form of the propagator for intermediate spin

Table 6.4 Systematic uncertainties for $\overline{K}^0\pi^+\pi^+\pi^-$.

$\overline{K}^0\pi^+\pi^+\pi^-$ Amplitude	A	B	C	D	E	F	G
4-Body Nonresonant	0.5	1.0	2.0	7.0	1.0	0.6	6.0
$K^-a_1^+$	1.0	1.0	2.0	4.0	1.0	0.6	5.0
$\overline{K}_1(1400)^0\pi^+$	0.5	1.0	1.0	3.0	1.0	0.6	7.0

1 resonances.

B) Uncertainties due to varying the parameter R in the Blatt-Weisskopf form-factors.

C) Uncertainties due to uncertainties in the masses and widths of the intermediate resonances.

D) Uncertainties due to Monte Carlo modeling.

E) Uncertainties due to Monte Carlo statistics.

F) Uncertainties due to detector resolution.

G) Uncertainties due to the possible presence of additional amplitudes. This uncertainty includes variations in the fractions obtained as amplitudes for decay modes in Table 6.3 are included.

7
$D^+ \to K^-\pi^+\pi^+\pi^0$.

The two-body decay modes which can contribute to the $\overline{K}^0\pi^+\pi^+\pi^-$ final state include $\overline{K}^{*0}\rho^+$, $\overline{K}_1(1270)^0\pi^+$ and $\overline{K}_1(1400)^0\pi^+$. No $\overline{K}a_1$ mode can contribute to this final state. There are three three-body modes which can contribute, $K^{*-}\pi^+\pi^+$, $\overline{K}^{*0}\pi^+\pi^0$ and $K^-\rho^+\pi^+$.

The recoil mass plot is shown in Fig. 7.1. There are 142 ± 21 events above background. The average ratio of signal to background in the region of recoil mass from 1.858 to 1.880 GeV is 0.74. The branching ratio has been determined in chapter 3 to be $B(D^+ \to K^-\pi^+\pi^+\pi^0) = 5.8 \pm 1.2 \pm 1.2\%$.

Limits on $\overline{K}_1(1270)^0\pi^+$ and $K^{*-}\pi^+\pi^+$ have been derived in the analysis of the $\overline{K}^0\pi^+\pi^+\pi^-$ final state above. We have confirmed that these amplitudes also yield insignificant fractions in the $K^-\pi^+\pi^+\pi^0$ final state. However, since our sensitivity to these amplitudes is much worse in this final state, we simply assume that these amplitudes do not contribute.

We have measured the branching ratio to $\overline{K}_1(1400)^0\pi^+$ in the analysis of the $\overline{K}^0\pi^+\pi^+\pi^-$ final state. This decay mode contributes an equal number of events to the $K^-\pi^+\pi^+\pi^0$ final state. We can therefore confirm this measurement. Using the

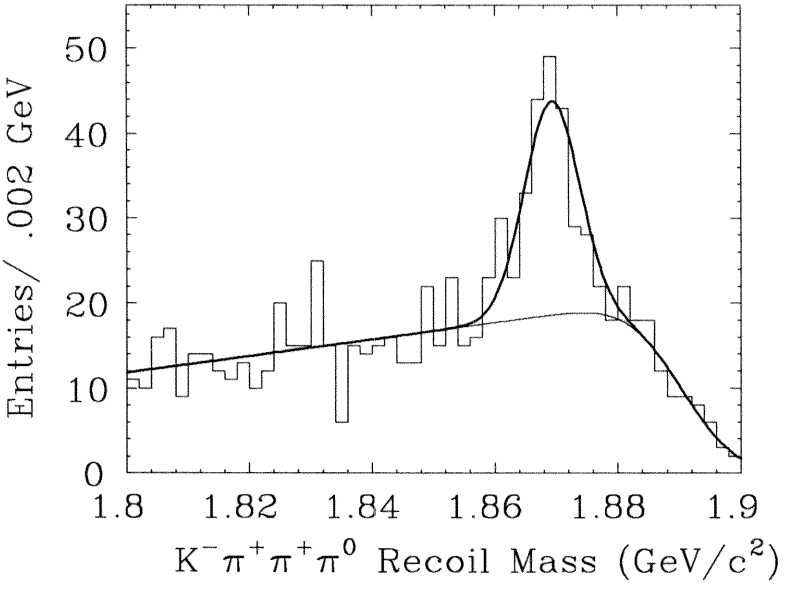

Figure 7.1 Signal for $D^+ \to K^-\pi^+\pi^+\pi^0$.

fraction measured in the $\overline{K}^0\pi^+\pi^+\pi^-$ final state and the values for σB derived in chapter 3, we expect the fraction of $\overline{K}_1(1400)^0\pi^+$ in the $K^-\pi^+\pi^+\pi^0$ final state to be 0.350 ± 0.086, where the error is statistical only. There are two different decay modes of the $\overline{K}_1(1400)^0$ which contribute to the $K^-\pi^+\pi^+\pi^0$ final state, as shown in the following equations, where the isospin factors are listed for each decay:

$$\begin{array}{ccccc} \overline{K}_1(1400)^0 & \to & \overline{K}^{*0}\pi^0 & \to & K^-\pi^+\pi^0 \\ & & -\sqrt{\frac{1}{3}} & & \sqrt{\frac{2}{3}} \end{array} \tag{7.1}$$

$$\begin{array}{ccccc} \overline{K}_1(1400)^0 & \to & K^{*-}\pi^+ & \to & K^-\pi^0\pi^+ \\ & & \sqrt{\frac{2}{3}} & & \sqrt{\frac{1}{3}} \end{array} \tag{7.2}$$

The isospin factors put constraints on both the relative fractions and relative phases of the amplitudes for these two processes. The fractions will be equal, and the phases will differ by π. These constraints are used in the fits.

Projections of $\mathcal{F}_B$ onto sideband events are shown in Fig. 7.2. There are large

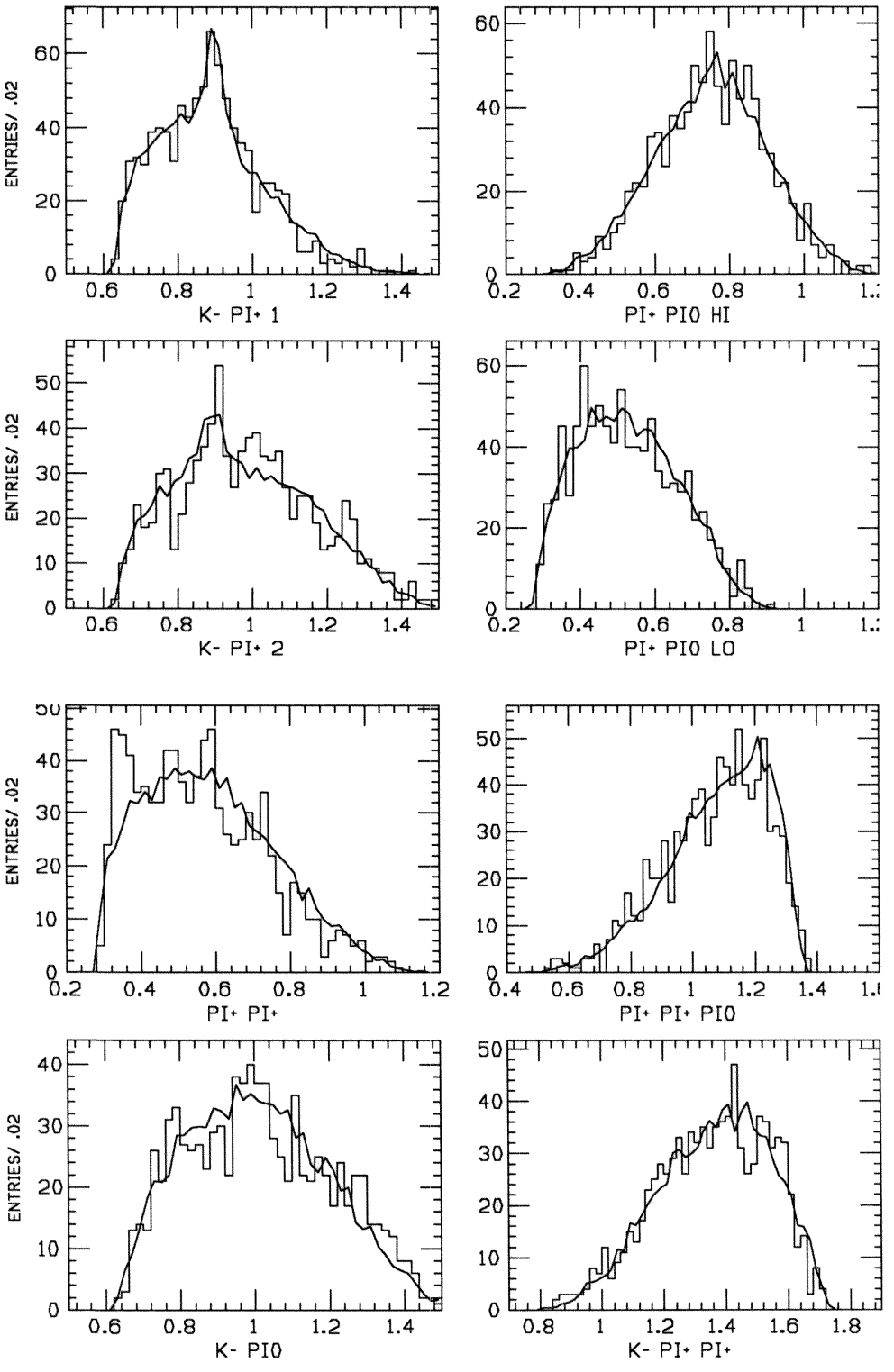

Figure 7.2 Projections of $\mathcal{F}_B$ onto sideband events.

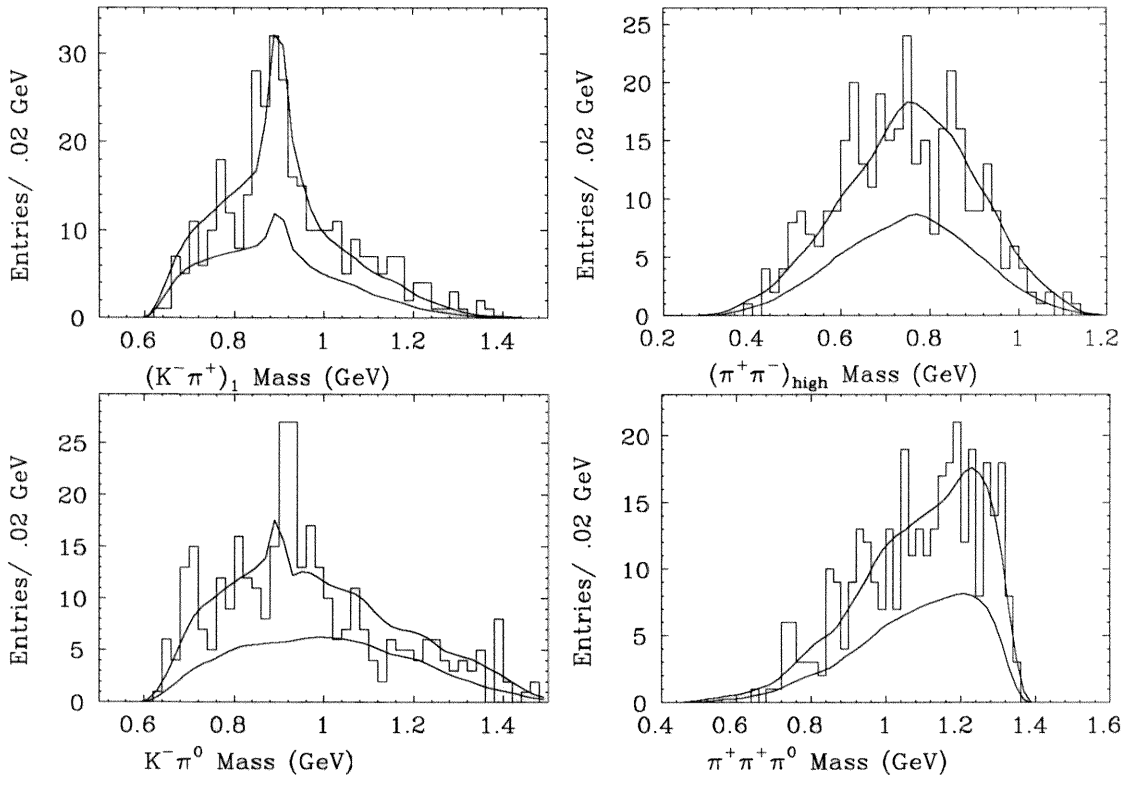

Figure 7.3 Projections of $\mathcal{F}_S$ onto events in the signal region.

corrections for resonant content in the sidebands. Projections of $\mathcal{F}$ onto events in the signal region are shown in Fig. 7.3. $\mathcal{F}_B$ is also drawn, scaled down to the background level. Large $\overline{K}^{*0}$ peaks are seen in the $K^-\pi^+$ mass plots. Although there is a large peak in $K^-\pi^0$ mass, it is too high in mass to fit a K^{*-} Breit-Wigner, and seems to be a fluctuation.

The results of the fit are shown in Table 7.1. The fraction of $\overline{K}_1(1400)^0\pi^+$ is 0.403 ± 0.097, in excellent agreement with the expected value. If the constraints on the relative fractions and phases of the two $\overline{K}_1(1400)^0\pi^+$ amplitudes are released, consistent results are obtained, and $-\ln\mathcal{L}$ improves by only 0.3.

The fraction for $\overline{K}^{*0}\rho^+$ is very large, 0.56 ± 0.08. In contrast to the $K^-\pi^+\pi^+\pi^-$ final state, both transverse and longitudinal helicities yield significant contributions.

Table 7.1 Results for $D^+ \to K^-\pi^+\pi^+\pi^0$.

Amplitude	Fraction (%)	Phase	Branching Ratio (%)
4-Body Nonresonant	$18.4 \pm 7.0 \pm 5.0$	0.86 ± 0.22	$1.1 \pm 0.5 \pm 0.4$
$\overline{K}^{*0}\rho^+$ Longitudinal	$25.1 \pm 7.3 \pm 7.0$	-0.27 ± 0.20	$2.2 \pm 0.8 \pm 0.8$
$\overline{K}^{*0}\rho^+$ Transverse	$29.2 \pm 3.7 \pm 6.0$	0.0	$2.5 \pm 0.6 \pm 0.7$
$\overline{K}^{*0}\rho^+$ Total	$55.5 \pm 7.7 \pm 11.0$		$4.8 \pm 1.2 \pm 1.4$
$\overline{K}_1(1400)^0\pi^+$	$40.3 \pm 9.7 \pm 8.0$	0.28 ± 0.15	$5.3 \pm 1.7 \pm 1.5$
$K^-\rho^+\pi^+$	$15.9 \pm 6.5 \pm 6.0$	0.67 ± 0.25	$0.9 \pm 0.4 \pm 0.4$

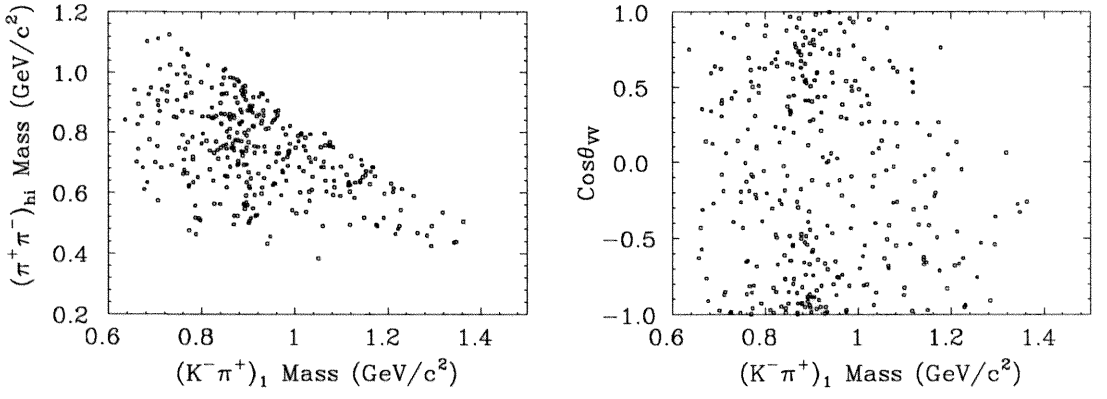

Figure 7.4 Illustration of $\overline{K}^{*0}\rho^+$ amplitude.

The fractions of the two helicities are consistent with being equal, and the relative phase is consistent with zero. This corresponds to the S-wave amplitude in the L/S basis discussed in chapter 4. Assuming this is true, the Lorentz-invariant amplitude for the total $\overline{K}^{*0}\rho^+$ assumes a very simple form when expressed in terms of three-momenta in the rest frame of the $\overline{K}^{*0}$:

$$A_{\overline{K}^{*0}\rho^+} = (\vec{p}_{K^-} - \vec{p}_{\pi_1^+}) \cdot (\vec{p}_{\pi^0} - \vec{p}_{\pi_2^+}) \tag{7.3}$$

where π_1^+ is the pion from the $\overline{K}^{*0}$. From this expression, we expect a distribution proportional to $\cos^2\theta_{VV}$, where θ_{VV} is the angle between the two three-vectors in the dot-product. Fig. 7.4 contains a scatter plot of $K^-\pi_1^+$ mass vs $\pi^+\pi^0_{\text{high}}$ mass.

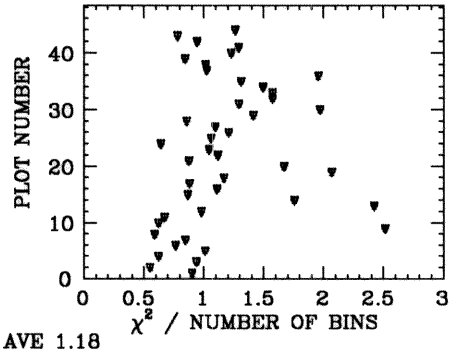

Figure 7.5 χ^2 for fits to data.

Table 7.2 Limits for $D^+ \to K^-\pi^+\pi^+\pi^0$.

Amplitude	Branching Ratio (%)
$\overline{K}^{*0}\rho^+$ P-wave	< 0.5
$\overline{K}^{*0}\rho^+$ Longitudinal (D-wave)	< 0.7
$\overline{K}^{*0}\pi^+\pi^0$	< 0.8

It is not obvious whether there is a cluster of $\overline{K}^{*0}$ events in the ρ^+ region, though there are definitely $\overline{K}^{*0}$ events outside the ρ^+ region. Also in Fig. 7.4, a scatter plot of $K^-\pi_1^+$ mass vs $\cos\theta_{VV}$ is more conclusive, and clearly shows the expected behavior of the $\overline{K}^{*0}\rho^+$ amplitude. The $\overline{K}^{*0}\rho^+$ amplitudes are highly preferred in the fits over any nonresonant $K^-\rho^+\pi^+$ amplitude, even when the $K^-\pi^+$ system is in a vector state.

There is also a significant fraction for nonresonant $K^-\rho^+\pi^+$, but only when the $K^-\rho^+$ system is in a pseudoscalar state, or the $K^-\pi^+$ system is in a scalar state.

Fig. 7.5 is a plot of χ^2 for 44 different projections. The average χ^2 for these plots is 1.18.

Table 7.2 contains upper limits for several decay modes which do not yield

Table 7.3 $K^-\pi^+\pi^+\pi^0$ decay chains.

$D^+ \to \overline{K}_1(1400)^0\pi^+$		
$\overline{K}_1(1400)^0 \to$	$\overline{K}^{*0}\pi^0$	$\overline{K}^{*0} \to K^-\pi^+$
	$K^{*-}\pi^+$	$K^{*-} \to K^-\pi^0$
$D^+ \to (\rho^+K^-)_A\pi^+$	$(\rho^+K^-)_A \to \rho^+K^-$	$\rho^+ \to \pi^+\pi^0$

Table 7.4 Systematic uncertainties for $K^-\pi^+\pi^+\pi^0$.

$K^-\pi^+\pi^+\pi^0$ Amplitude	A	B	C	D	E	F	G
4-Body Nonresonant	0.2	0.3	0.6	4.0	1.5	0.6	2.0
$\overline{K}^{*0}\rho^+$ Longitudinal	0.4	0.3	0.4	6.0	1.5	0.6	4.0
$\overline{K}^{*0}\rho^+$ Transverse	0.4	0.3	1.0	4.0	1.5	0.6	4.0
$\overline{K}^{*0}\rho^+$ Total	0.4	0.6	1.4	8.0	1.5	0.6	7.0
$\overline{K}_1(1400)^0\pi^+$	0.2	2.5	2.0	6.0	1.5	0.6	4.0
$K^-\rho^+\pi^+$	0.4	1.0	0.4	3.0	1.5	0.6	5.0

significant fractions when included in the fits. We have set a limit on the longitudinal component of the D-wave amplitude, for reasons to be discussed in chapter 9. The upper limit for each decay mode takes into account statistical errors, as well as any variations in the fractions obtained as the partial waves of the three-body decay mode are changed, or as amplitudes for other decay modes in Table 7.2 are included.

The decay chains, to be compared with Table 4.1 are listed in Table 7.3.

Systematic Uncertainties.

Systematic uncertainties from the following sources are listed in Table 7.4:

A) Uncertainties due to changing the form of the propagator for intermediate spin 1 resonances.

B) Uncertainties due to varying the parameter R in the Blatt-Weisskopf

form-factors.

C) Uncertainties due to uncertainties in the masses and widths of the intermediate resonances.

D) Uncertainties due to Monte Carlo modeling.

E) Uncertainties due to Monte Carlo statistics.

F) Uncertainties due to detector resolution.

G) Uncertainties due to the possible presence of additional amplitudes. This uncertainty includes any variations in the fractions obtained as the partial wave of the three-body decay mode is changed, or as amplitudes for decay modes in Table 7.2 are included.

8
$D^0 \to \overline{K}^0\pi^+\pi^-\pi^0$.

The quality of the data for the $\overline{K}^0\pi^+\pi^-\pi^0$ final state is relatively poor. The statistics are low, and the backgrounds high. In addition, in this analysis, we cannot tell if an individual $\overline{K}^0\pi^+\pi^-\pi^0$ candidate event is from a D^0 decay or a $\overline{D}^0$ decay. To deal with this problem, we form a total p.d.f. out of the p.d.f. for each hypothesis:

$$\mathcal{F}_S = \mathcal{F}_{D^0} + \mathcal{F}_{\overline{D}^0} \tag{8.1}$$

Compounding the problems with the data, there are a large number of decay modes that can contribute to this final state, as seen in Table 1.1, so that the resonant substructure is potentially very complex.

The recoil mass plot, shown in Fig. 8.1, has 140 ± 28 signal events. The average ratio of signal to background in the region of recoil mass from 1.854 to 1.876 GeV is 0.34. The branching ratio has been determined in chapter 3 to be $B(D^0 \to \overline{K}^0\pi^+\pi^-\pi^0) = 10.3 \ \pm 2.2 \ \pm 2.5\%$

In order to extract what information we can, we make the following set of simplifying assumptions, each of which has reasonable justifications:

- Several of the decay modes contributing to this final state have already been measured in the $K^-\pi^+\pi^+\pi^-$ final state. We constrain the relative

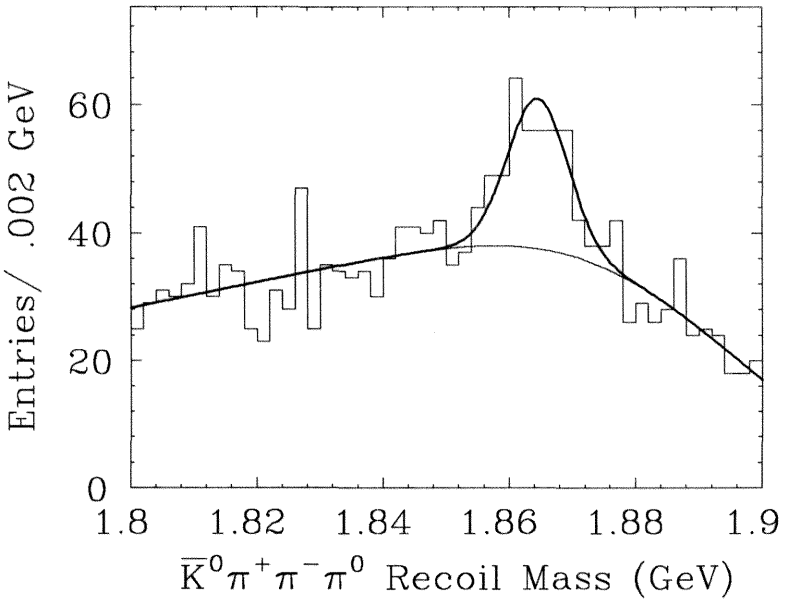

Figure 8.1 Signal for $D^0 \to \overline{K}^0\pi^+\pi^-\pi^0$.

fractions and phases of the amplitudes for $\overline{K}^{*0}\rho^0$ (transverse), $K_1(1270)^-\pi^+$, and $\overline{K}^{*0}\pi^+\pi^-$ to the values expected from these measurements. Careful isospin calculations are required to convert both the relative fractions *and* phases in one final state to those expected in another final state. The overall fraction of these amplitudes is allowed to vary, providing a consistency check. The relative fractions and phases are allowed to vary within errors.

- When an amplitude for $K_1(1400)^-\pi^+$ is included, the fraction is typically about 12 ± 7, consistent with zero. A more stringent upper limit was placed on this decay mode in the analysis of the $K^-\pi^+\pi^+\pi^-$ final state. Therefore, this amplitude is left out of the final fit. However, the variations in the fractions as this amplitude is included in the fit will be included in the systematic errors.

- When an amplitude for p-wave $K^{*-}\rho^+$ is included, the fraction is as large

as $20 \pm 7\%$. The stringent upper limits on p-wave $\overline{K}^{*0}\rho^0$ and $\overline{K}^{*0}\rho^+$ decays rule out the possibility of a fraction for p-wave $K^{*-}\rho^+$ above 9%, via the isospin relations, so we leave this amplitude out of the final fit. However, the variations in the fractions as this amplitude is included in the fit will be included in the systematic errors.

- When amplitudes for $\overline{K}_1(1270)^0\pi^0$ are included, the fraction is typically $18 \pm 9\%$, a 2σ effect. Given the measurement of $K_1(1270)^-\pi^+$, the upper limit on $\overline{K}_1(1270)^0\pi^+$, and the isospin relations, we can calculate a maximum plausible value for $\overline{K}_1(1270)^0\pi^0$. We estimate a 90% upper limit of 3.2% for $K_1(1270)^-\pi^+$, and use the previously derived upper limit of 1.1% for $\overline{K}_1(1270)^0\pi^+$. We assume a relative phase of π between $A_{1/2}$ and $A_{3/2}$ so that the interference is maximally destructive for $K_1(1270)^-\pi^+$ and constructive for $\overline{K}_1(1270)^0\pi^0$. We find that the fraction for $\overline{K}_1(1270)^0\pi^0$ cannot be more than 10%. We are clearly not sensitive to a fraction even this large, so we leave the amplitudes for $\overline{K}_1(1270)^0\pi^0$ out of the final fits. However, the variations in the fractions as this amplitude is included in the fit will be included in the systematic errors.

- There are five different types of three body amplitudes which can contribute to this final state, $\overline{K}^0\rho^0\pi^0$, $\overline{K}^0\rho^-\pi^+$, $\overline{K}^0\rho^+\pi^-$, $\overline{K}^{*0}\pi^+\pi^-$, and $K^{*-}\pi^+\pi^0$. Each of these comes in six different partial waves, assuming there is only one unit of angular momentum. We assume that none of these contribute in the final fit, but we do include them one at a time, to obtain the systematic errors on the other fractions.

A scatter-plot of $(K^-\pi^+)_1$ mass vs. $(\pi^+\pi^-)_{\text{high}}$ mass is in Fig. 8.2. There

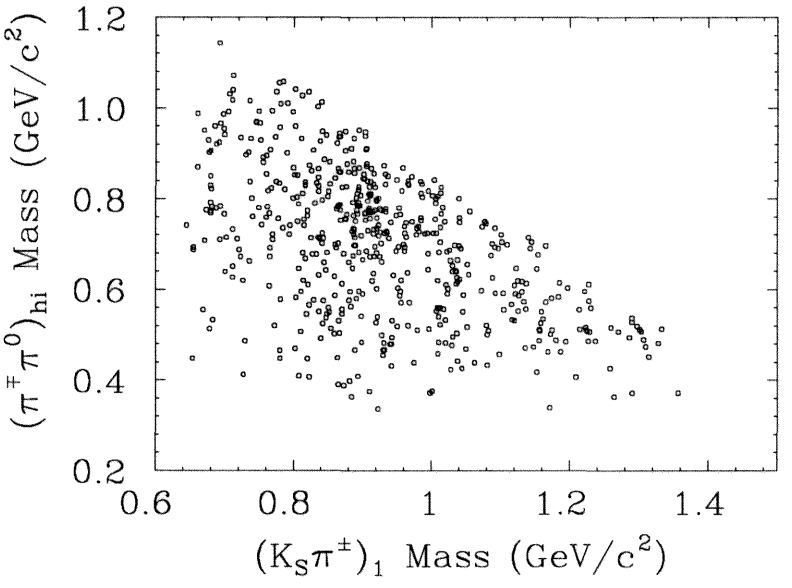

Figure 8.2 Scatter-plot of $(K^-\pi^+)_1$ mass vs. $(\pi^+\pi^-)_{\text{high}}$ mass.

appears to be a cluster of events in the $K^{*-}\rho^+$ region. None of the angular distributions associated with the three $K^{*-}\rho^+$ helicity amplitudes show any definite structure.

Projections of $\mathcal{F}_B$ onto sideband events are shown in Fig. 8.3. Projections of $\mathcal{F}$ onto events in the signal region are shown in Fig. 8.3. $\mathcal{F}_B$ is also drawn, scaled down to the background level. There is a $\overline{K}^*$ peak visible in the $(\overline{K}^0\pi^{\mp})_1$ mass plot and a strong ω peak visible in the $\pi^+\pi^-\pi^0$ mass plot. Also, there is a distinct absence of an enhancement at low $\overline{K}^0\pi^0$ mass, indicating that the $D^0 \to \overline{K}^0 a_1^0$ amplitude is small.

The results of the fit are shown in Table 8.1. The branching ratio for $K^{*-}\rho^+$, while reasonably large at about 6%, is very small compared to the BSW prediction of 21%. Unfortunately, the fits do not yield significant results on which helicity

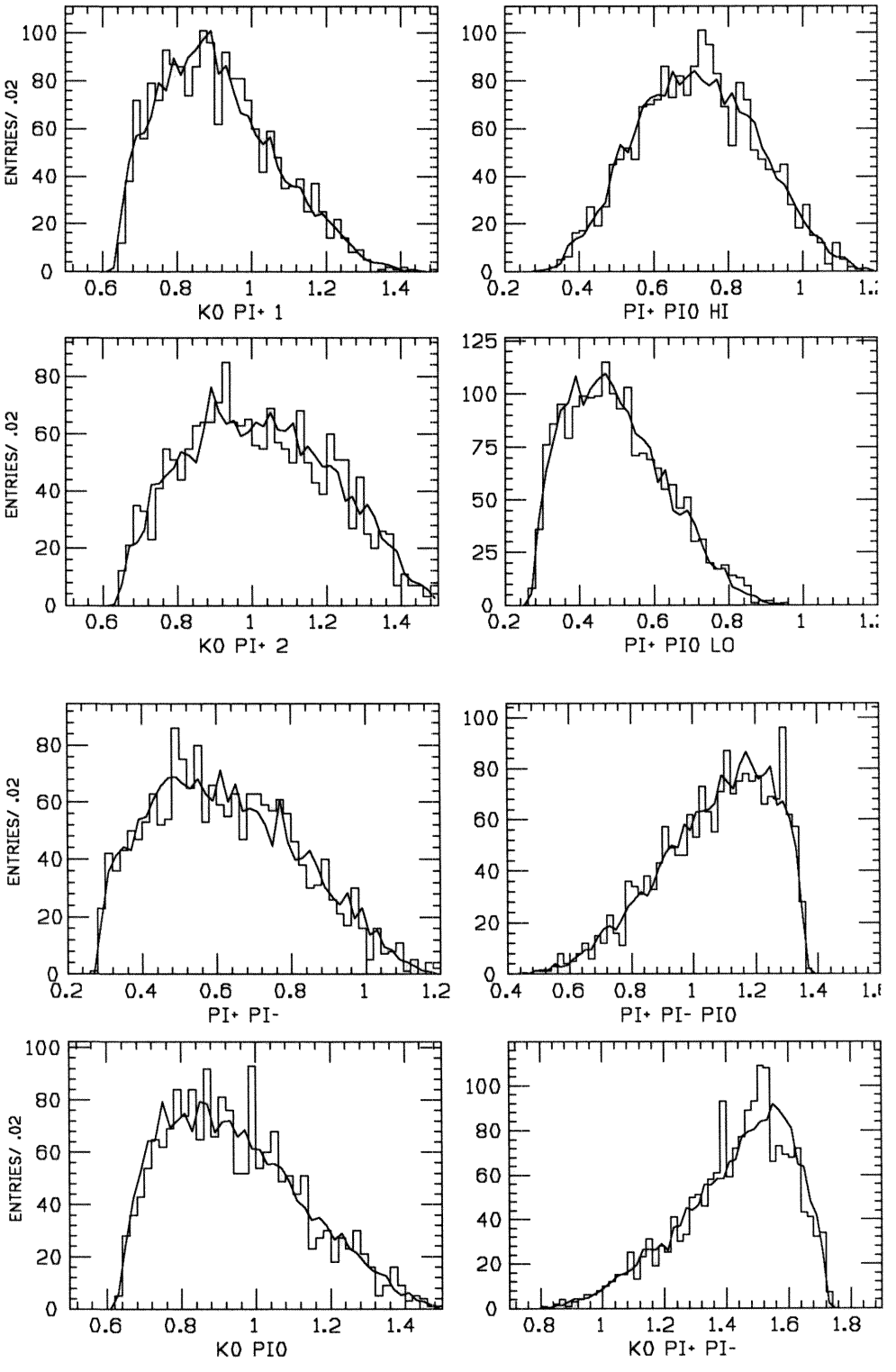

Figure 8.3 Projections of $\mathcal{F}_B$ onto sideband events.

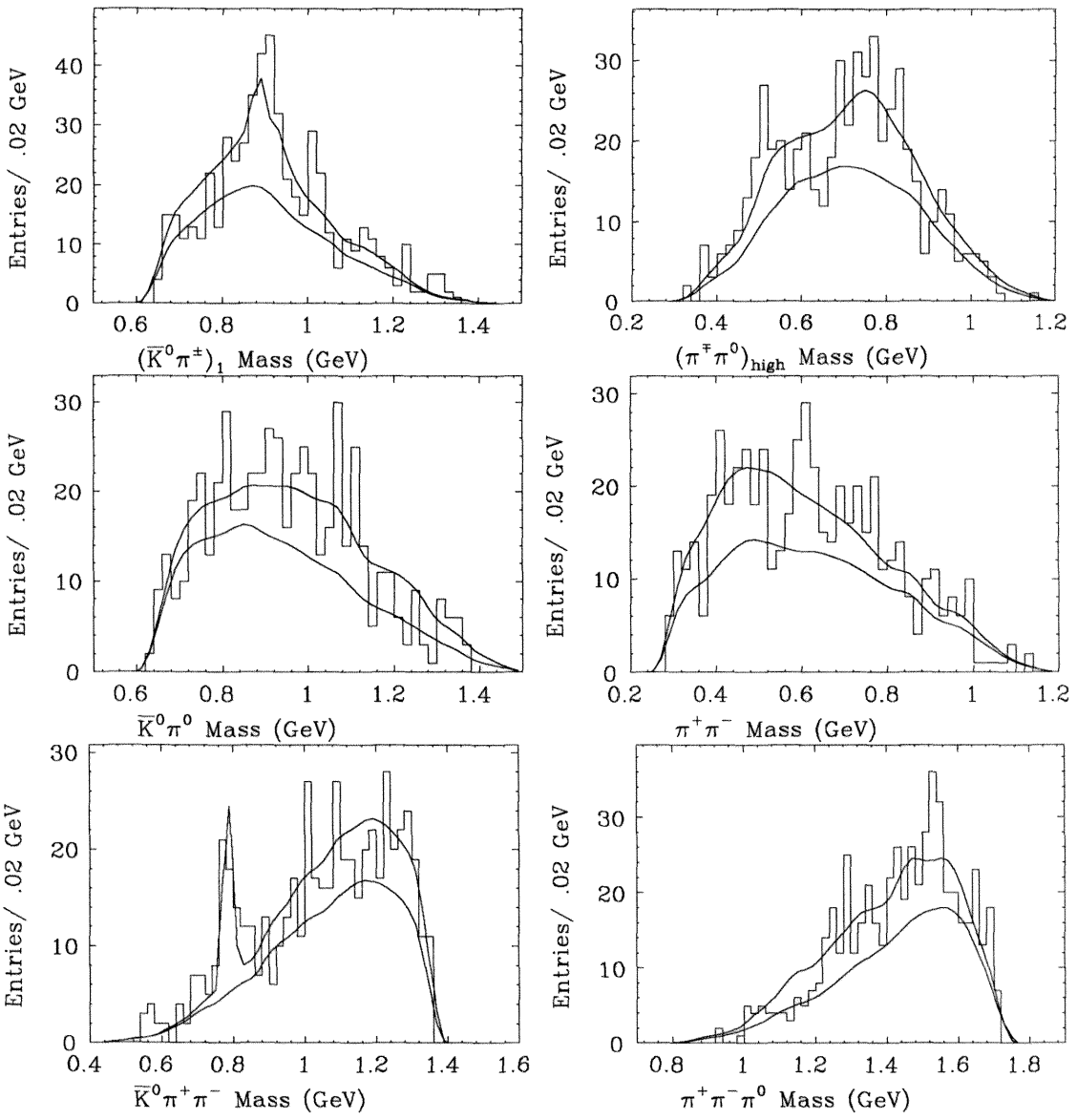

Figure 8.4 Projections of $\mathcal{F}_S$ onto events in the signal region.

amplitudes contribute to the $K^{*-}\rho^+$ signal. Reasonably stringent upper limits for $\overline{K}^0 a_1^0$ and $\overline{K}_1(1400)^0\pi^0$ are obtained, at least compared to the large branching ratios obtained for the other isospin versions of these decay modes. While the fractions for $\overline{K}^{*0}\rho^0$ (transverse), $K_1(1270)^-\pi^+$, and $\overline{K}^{*0}\pi^+\pi^-$ are not statistically significant, they are consistent with the results from the fit to the $K^-\pi^+\pi^+\pi^-$ final state.

Table 8.1 Results for $D^0 \to \overline{K}^0\pi^+\pi^-\pi^0$.

Amplitude	Fraction (%)	Phase	Branching Ratio (%)
4-Body Nonresonant	21.0 ± 14.7 ± 15.0	-0.45 ± 0.55	2.2 ± 1.6 ± 1.7
$K^{*-}\rho^+$ Longitudinal	19.3 ± 7.4	0	
$K^{*-}\rho^+$ Transverse	21.1 ± 12.0	5.16 ± 0.48	
$K^{*-}\rho^+$ Total	40.4 ± 12.5 ± 8.4		6.2 ± 2.3 ± 2.0
$\overline{K}^0 a_1^0$			< 1.9
$\overline{K}_1(1400)^0\pi^0$			< 3.7
$\overline{K}^0\omega$	19.5 ± 4.3 ± 1.4		2.25 ± 0.7 ± 0.6
$\overline{K}^{*0}\rho^0$ Transverse	4.2 ± 3.7		1.3 ± 1.2
$K_1(1270)^-\pi^+$	4.8 ± 1.5		1.0 ± 0.4
$\overline{K}^{*0}\pi^+\pi^-$	12.7 ± 7.0		3.9 ± 2.3

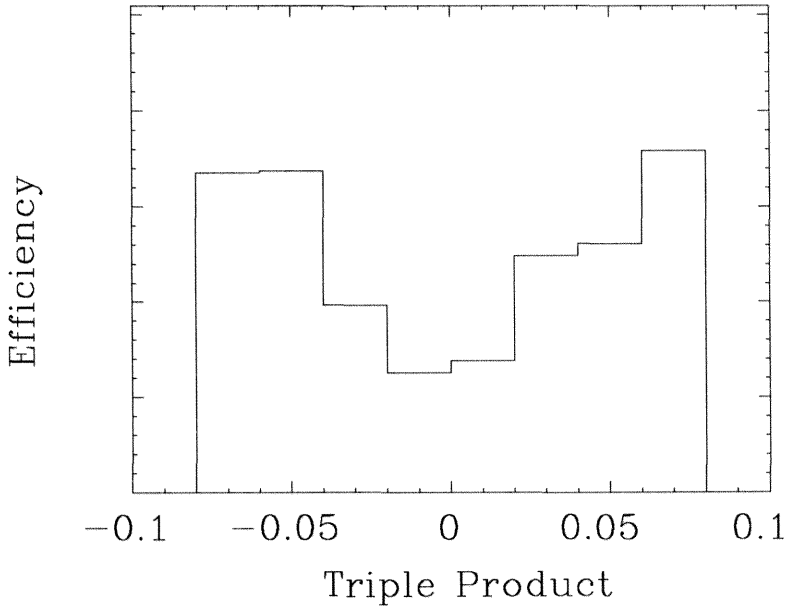

Figure 8.5 Efficiency as a function of $\overline{K}^0\omega$ amplitude.

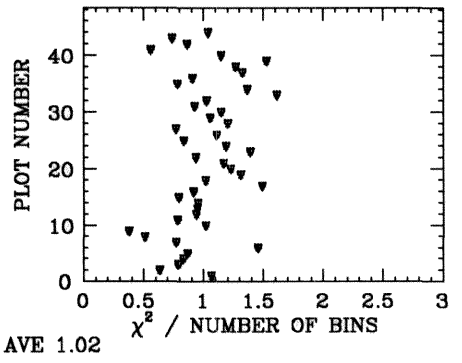

Figure 8.6 χ^2 for fits to data.

For the ω line-shape, a Breit-Wigner is convoluted with a Gaussian.[57] The resolution predicted by the Monte Carlo is 8.7 MeV/c^2. Interference between the $\overline{K}^0\omega$ amplitude and other amplitudes is ignored. To obtain the $\overline{K}^0\omega$ amplitude, we simply evaluate the following triple product, where the 3-momenta are evaluated in the ω frame:

$$A_{\overline{K}^0\omega} = \vec{p}_K \cdot (\vec{p}_{\pi^+} \times \vec{p}_{\pi^-}) \tag{8.2}$$

The branching ratio obtained for $\overline{K}^0\omega$ is smaller than in previous Mark III analyses, which obtained values above 3%. The branching ratio for $\overline{K}^0\omega$ obtained in Ref. 11, adjusted for the new D^0 production cross-section in Ref. 37, is $3.2 \pm 1.4 \pm 0.9\%$. One possible explanation is that the efficiency is highest where the $\overline{K}^0\omega$ amplitude is highest, so the branching ratio will be overestimated if this isn't accounted for. Fig. 8.5 shows the efficiency as a function of the value of this triple product.

Fig. 8.6 is a plot of χ^2 for 44 different projections. The average χ^2 for these plots is 1.02.

The systematic error on the fraction of $\overline{K}^0\omega$ includes 0.8% for the variations among different fits, 1% for the Monte Carlo statistics, and 0.5% for the variation as different values for the resolution in $\pi^+\pi^-\pi^0$ mass are assumed for the

ω line-shape. The systematic errors for the other modes account for the variations of the fractions as different three-body amplitudes are included, as well as the $\overline{K}_1(1270)^0\pi^+$, $\overline{K}_1(1400)^0\pi^+$, and P-wave $\overline{K}^{*0}\rho^+$ amplitudes. The errors due to changing the parametrizations of Breit-Wigners or amplitudes are relatively small, since none of the statistically significant amplitudes involve very broad intermediate resonances. The determination of the errors due to Monte Carlo modelling is dominated by the large statistical errors.

9
Conclusions.

In this thesis we have measured the resonant substructure of four $D \to \overline{K}\pi\pi\pi$ final states, obtaining branching ratios and limits for several two, three, and four-body decay modes. In this chapter we gather together the results from all the final states, perform an isospin decomposition on several two-body decay modes, discuss form-factors in $D \to \overline{K}^*\rho$ decays, and summarize our conclusions.

9.1 Isospin Decompositions.

Isospin decomposition for $D \to \overline{K}a_1$ decays.

We have obtained measurements of the branching ratios for $K^-a_1^+$ and $\overline{K}^0a_1^+$ and a stringent upper limit on $\overline{K}^0a_1^0$. This last mode is proportional to the parameter a_2 in the BSW model, and is therefore expected to be small in the absence of isospin phase shifts. Given the large branching ratios for the first two decay modes, isospin phase shifts could have made the branching ratio for $\overline{K}^0a_1^0$ large. The upper limit, therefore, is very useful for putting limits on the effects of isospin phase shifts and eliminating this one source of ambiguity when comparing the measurements with the models.

Table 9.1 $\overline{K}a_1$ Branching Ratios (%).

$\lvert A_{1/2}/A_{3/2}\rvert = 3.0 \pm 0.6$, $\cos\delta = 1.1 \pm 0.4$		
Mode	Measurement	BSW
$K^-a_1^+$	$9.0 \pm 0.9 \pm 1.7$	5.0
$\overline{K}^0 a_1^0$	$0.43 \pm 0.99, < 1.9$	(0.5)
$\overline{K}^0 a_1^+$	$7.1 \pm 1.8 \pm 1.1$	3.8

Table 9.2 $\overline{K}a_1$ Branching Ratios (%), with the constraint $\cos\delta < 1$.

$\lvert A_{1/2}/A_{3/2}\rvert = 3.0 \pm 0.5$, $\cos\delta > 0.52$		
Mode	Measurement	BSW, assuming $\cos\delta = 0.52$
$K^-a_1^+$	8.8 ± 1.7	4.3
$\overline{K}^0 a_1^0$	0.7 ± 0.4	1.2
$\overline{K}^0 a_1^+$	7.0 ± 2.1	3.8

As discussed in chapter 1, BSW have made predictions for $K^-a_1^+$ and $\overline{K}^0 a_1^+$. Using these two predictions, we can calculate, via the isospin relations, what the prediction for $\overline{K}^0 a_1^0$ should be. We list the measurements and predictions, along with the isospin decomposition, in Table 9.1. We define $\delta = \delta_{1/2} - \delta_{3/2}$. We combine statistical and systematic errors in quadrature to obtain the total errors on the branching ratios, which we then propagate to obtain the errors on the isospin quantities. The ratio of isospin amplitudes is 3.0, which is similar to that found in PP and PV decays. The measured branching ratios are somewhat higher than the predictions.

Since $\cos\delta$ obviously cannot be greater than 1, we recalculate the branching ratios with the constraint that $\cos\delta < 1$. This is done by defining a χ^2:

Table 9.3 $\overline{K}^*\rho$ Branching Ratios (%).

$\lvert A_{1/2}/A_{3/2}\rvert = 3.4 \pm 0.9$, $\cos\delta = 0.4 \pm 0.4$			
Mode	Measurement	BSW	BSW, $\cos\delta = 0.4 \pm 0.4$
$K^{*-}\rho^+$	$6.2 \pm 2.3 \pm 2.0$	21	17 ± 1.4
$\overline{K}^{*0}\rho^0$	$1.9 \pm 0.3 \pm 0.7$	2.0	6 ± 1.4
$\overline{K}^{*0}\rho^+$	$4.8 \pm 1.2 \pm 1.4$	17	17

$$\chi^2 = \sum_{\overline{K}a_1 \text{ modes}} \frac{(BR_{\text{new}} - BR_{\text{old}})^2}{\sigma_{BR}^2} \tag{9.1}$$

where BR_{old} are the measurements in Table 9.1 and BR_{new} are the recalculated values, and σ_{BR} are the errors on the branching ratios in Table 9.1, where the statistical and systematic errors are combined in quadrature. The recalculated values are obtained by minimizing χ^2 subject to the constraint. We also obtain a 90% CL lower limit on $\cos\delta$ of 0.52. The results are in Table 9.2. The numbers for $K^-a_1^+$ and $\overline{K}^0a_1^+$ aren't greatly affected, but the errors on $\overline{K}^0a_1^0$ are much reduced. Also, we have recalculated the BSW predictions assuming $\cos\delta = 0.52$.

Isospin Decomposition for $D \to \overline{K}^*\rho$ Decays.

We have obtained measurements of the branching ratios for all three $\overline{K}^*\rho$ modes. BSW have made predictions for all these modes. We list the measurements and predictions, along with the isospin decomposition, in Table 9.3. We also list the BSW predictions, recalculated with the measured value of the isospin phase shift. Again, the ratio of isospin amplitudes is in the range found for PP and PV modes.

The branching ratio for $\overline{K}^{*0}\rho^0$ was first reported in Ref. 58, and was found to be in good agreement with the predicted value. Now that the other two $\overline{K}^*\rho$ modes have been measured, and isospin phase shifts have been taken into account, we find

Table 9.4 Limits on P-wave $\overline{K}^*\rho$ Branching Ratios (%).

Mode	Limits
$K^{*-}\rho^+$	< 1.5
$\overline{K}^{*0}\rho^0$	< 0.3
$\overline{K}^{*0}\rho^+$	< 0.5

that the predictions for $\overline{K}^*\rho$ are actually much greater than the measured values.

We find that the $\overline{K}^{*0}\rho^0$ mode is completely transversely polarized. In terms of the L/S basis, this mode is a mixture of S and D-wave amplitudes such that the longitudinal components of these two amplitudes cancel. We have placed an upper limit on the P-wave component. For the $\overline{K}^{*0}\rho^+$ mode, we find an equal mixture of transverse and longitudinal polarization, consistent with a pure S-wave amplitude. We have placed limits on the P and D-wave components. For the $K^{*-}\rho^+$ mode, we do not have very good sensitivity, but both polarizations seem to be present. A detailed study of polarization in this mode would enable us to perform an isospin decomposition individually for each partial wave, and confirm the observation of a large D-wave component in $\overline{K}^{*0}\rho^0$. In Table 9.4, we summarize the upper limits on P-Wave $\overline{K}^*\rho$ decays. The limit on P-wave $K^{*-}\rho^+$ is obtained using the other two $\overline{K}^*\rho$ modes and the isospin relations.

Isospin Decomposition for $D \to \overline{K}_1(1270)\pi$ Decays.

We have obtained a measurement of the branching ratio for $K_1(1270)^-\pi^+$, and a limit for $\overline{K}_1(1270)^0\pi^+$. Using these two numbers, the best we can do is put a lower limit on the ratio of isospin amplitudes. We estimate a 90% CL lower limit of 0.73% for $K_1(1270)^-\pi^+$. Using the upper limit on $\overline{K}_1(1270)^0\pi^+$, and assuming maximum constructive interference between the isospin amplitudes for $K_1(1270)^-\pi^+$, we

Table 9.5 $\overline{K}_1(1270)\pi$ Branching Ratios (%).

$\lvert A_{1/2}/A_{3/2}\rvert > 2.0$	
Mode	Measurement
$K_1(1270)^-\pi^+$	$1.8 \pm 0.5 \pm 0.8$
$\overline{K}_1(1270)^0\pi^0$	< 2.0
$\overline{K}_1(1270)^0\pi^+$	< 1.1

Table 9.6 $\overline{K}_1(1400)\pi$ Branching Ratios (%).

$\lvert A_{1/2}/A_{3/2}\rvert < 4.3$	
Mode	Measurement
$K_1(1400)^-\pi^+$	< 1.2
$\overline{K}_1(1400)^0\pi^0$	< 3.7
$\overline{K}_1(1400)^0\pi^+$	$4.1 \pm 1.2 \pm 1.2$

obtain the smallest plausible value of the ratio of isospin amplitudes. The results are summarized in Table 9.5. The limit on $\overline{K}_1(1270)^0\pi^0$ is derived from the results for the other two $\overline{K}_1(1270)\pi$ modes and the isospin relations.

Isospin Decomposition for $D \to \overline{K}_1(1400)\pi$ Decays.

We have obtained a measurement of the branching ratio for $\overline{K}_1(1400)^0\pi^+$, and limits for $K_1(1400)^-\pi^+$ and $\overline{K}_1(1400)^0\pi^0$. The best we can do is put an upper limit on the ratio of isospin amplitudes. We estimate a 90% CL lower limit of 1.9% for $\overline{K}_1(1400)^0\pi^+$. Using the two upper limits, we obtain the largest plausible value of the ratio of isospin amplitudes. The results are summarized in Table 9.6.

Summary of Isospin Decompositions.

In Table 9.7 we gather the results on the isospin decompositions from this thesis, together with previous results discussed in chapter 1. As discussed in chapter 1, the

Table 9.7 Isospin Decompositions.

Mode	$\lvert A_{1/2}/A_{3/2}\rvert$	δ	$\cos\delta$
$\overline{K}\pi$	3.67 ± 0.27	$77° \pm 11°$	0.2 ± 0.2
$\overline{K}\rho$	3.12 ± 0.4	$0° \pm 26°$	$1.0^{+0.0}_{-0.1}$
$\overline{K}^*\pi$	3.22 ± 0.97	$84° \pm 13°$	0.1 ± 0.2
$\overline{K}a_1$	3.0 ± 0.5	$-59° < \delta < 59°$	> 0.52
$\overline{K}^*\rho$	3.4 ± 0.9	$66° \pm 30°$	0.4 ± 0.4
$\overline{K}_1(1270)\pi$	> 2.0		
$\overline{K}_1(1400)\pi$	< 4.3		

Table 9.8 Branching Ratios for Three-body Decay Modes.

Amplitude	Branching Ratio (%)
$D^0 \to \overline{K}^{*0}\pi^+\pi^-$	$1.9 \pm 0.3 \pm 0.6$
$D^0 \to K^-\rho^0\pi^+$	$0.8 \pm 0.2 \pm 0.4$
$D^+ \to K^-\rho^+\pi^+$	$0.9 \pm 0.4 \pm 0.4$

hadronic widths of the PP and PV modes in D^0 and D^+ decays reflect the lifetime difference of the D^0 and D^+, and leads to a ratio of isospin amplitudes of 3.0 to 3.5. For VV and PA decays, we find ratios in the same range. Thus, these decay modes also reflect the lifetime difference of the D mesons, and confirm that an understanding of this difference requires an understanding of two-body decay modes.

9.2 Three and Four Body Decay Modes, and Upper Limits.

Although we find that about 75% of $D \to \overline{K}\pi\pi\pi$ decays are from two-body decay modes, there are still significant three and four-body contributions. These

Table 9.9 Branching Ratios for Four-body Decay Modes.

Amplitude	Branching Ratio (%)
$D^0 \to K^-\pi^+\pi^+\pi^-$	$2.2 \pm 0.3 \pm 0.6$
$D^0 \to \overline{K}^0\pi^+\pi^-\pi^0$	$2.2 \pm 1.6 \pm 1.7$
$D^+ \to \overline{K}^0\pi^+\pi^+\pi^-$	$1.1 \pm 0.4 \pm 0.7$
$D^+ \to K^-\pi^+\pi^+\pi^0$	$1.1 \pm 0.5 \pm 0.4$

Table 9.10 Upper Limits.

Amplitude	Branching Ratio (%)
$D^0 \to \overline{K}^{*0}\rho^0$ Longitudinal (S-wave)	< 0.3
$D^0 \to \overline{K}^{*0}\rho^0$ P-wave	< 0.3
$D^+ \to \overline{K}^{*0}\rho^+$ P-wave	< 0.5
$D^+ \to \overline{K}^{*0}\rho^+$ Longitudinal D-wave	< 0.7
$D^+ \to \overline{K}_1(1270)^0\pi^+$	< 1.1
$D^0 \to K_1(1400)^-\pi^+$	< 1.2
$D^0 \to K^-a_2(1320)^+$	< 0.6
$D^+ \to \overline{K}^0a_2(1320)^+$	< 0.8
$D^0 \to K^*(1415)^-\pi^+$	< 1.2
$D^+ \to \overline{K}^*(1415)^0\pi^+$	< 0.7
$D^+ \to K^{*-}\pi^+\pi^+$	< 1.3
$D^+ \to \overline{K}^{*0}\pi^+\pi^0$	< 0.8
$D^+ \to \overline{K}^0\rho^0\pi^+$	< 0.4

contributions may contain two-body decays involving very broad resonances or tails of resonances above threshold.

The three-body decays $\overline{K}^*\pi\pi$ and $\overline{K}\rho\pi$ with significant contributions are listed in Table 9.8. Since the spin of the vector mesons in these decays is one, there must also be one unit of orbital angular momentum to conserve total angular momentum. Thus, there are several possible partial waves available for these three-body decays.

Table 9.11 Form-factors in the BSW model.

	$D \to \overline{K}^*$	$D \to \rho$
$A_1(0)$	0.88	0.78
$A_2(0)$	1.15	0.92
$V(0)$	1.23	1.23

Table 9.12 Branching ratios (%) in BSW model, using form-factors from E691.

Mode	Measurement	BSW, $\cos\delta = 0.4 \pm 0.4$
$K^{*-}\rho^+$	$6.2 \pm 2.3 \pm 2.0$	7.5 ± 2.1
$\overline{K}^{*0}\rho^0$	$1.9 \pm 0.3 \pm 0.7$	2.5 ± 0.9
$\overline{K}^{*0}\rho^+$	$4.8 \pm 1.2 \pm 1.4$	6.0 ± 1.7

We are not sensitive to the details of the partial wave content.

There are very distinctive four-body contributions, listed in Table 9.9. For these amplitudes, all the final state mesons are assumed to be in relative S-waves.

We have also been able to establish upper limits for several decay modes, collected together in Table 9.10.

9.3 Form-factors.

The role of form-factors in semileptonic and hadronic decays is described in detail in chapter 1. In the model of BSW, the matrix element in equation (1.9) applies to both semileptonic and hadronic decays. The decays $D^0 \to K^{*-}\rho^+$ and $D^+ \to \overline{K}^{*0}e^+\nu$ both involve the same $D \to \overline{K}^*$ form-factors. As discussed in chapter 1, a study by the E691 collaboration of $D^+ \to \overline{K}^{*0}e^+\nu$ decays has suggested that the values of the form-factors are not predicted correctly by the models, as shown in Table 1.3.

While the decay $D^0 \to K^{*-}\rho^+$ involves $D \to \overline{K}^*$ form-factors, the decay $D^0 \to \overline{K}^{*0}\rho^0$ involves $D \to \rho$ form-factors, and the decay $D^+ \to \overline{K}^{*0}\rho^+$ involves both $D \to \overline{K}^*$ and $D \to \rho$ form-factors. The values of these form-factors as calculated in the BSW model are shown in Table 9.11. These values are the ones used for the predictions in Table 9.3. If we substitute the E691 measured values into the BSW model, we obtain the results listed in Table 9.12. We have assumed that the $D \to \rho$ form-factors are equal to the $D \to \overline{K}^*$ form-factors. These results are much closer to the measured values than the predictions in Table 9.3. Thus, the disagreement of the predictions from the data may be due to problems with the form-factor predictions rather than with the factorization hypothesis. Conversely, if factorization is a good hypothesis, we confirm the E691 results.

We can gain information on these form-factors from our studies of $D \to \overline{K}^*\rho$. While we do not have enough information on polarization in $D^0 \to K^{*-}\rho^+$, and the mode $D^0 \to \overline{K}^{*0}\rho^0$ is dominated by FSI, the decay $D^+ \to \overline{K}^{*0}\rho^+$ is theoretically relatively simple, as summarized in Table 1.7. This mode is unaffected by isospin phase shifts, and inelastic FSI should be small because they must proceed through the exotic $I = 3/2$ channel. Also, there is a possibility of weak annihilation only for D^0 decays. We therefore concentrate on the D^+ mode in this discussion of form-factors. The disadvantage of this decay mode is that it involves a subtraction of two terms, equation (1.36), the first proportional to the $D \to \overline{K}^*$ form-factors, and the second the $D \to \rho$ form-factors.

Taking the product of the hadronic currents in equations (1.9) and (1.37), we find that the matrix element for a VV decay has three distinct terms. The first is

Table 9.13 Partial wave breakdown for $\overline{K}^*\rho$ decays in BSW model.

	Amplitude			Width, 10^{10}sec^{-1}
	S-wave	P-wave	D-wave	Total
$K^{*-}\rho^+$	$6.3a_1$	$-1.3a_1$	$0.9a_1$	$34.05a_2^1$
$\overline{K}^{*0}\rho^0$	$4.5a_2$	$-0.9a_2$	$0.6a_2$	$18.45a_2^2$
$\overline{K}^{*0}\rho^+$	$6.3a_1 - 6.4a_2$	$-1.3a_1 + 1.3a_2$	$0.9a_1 - 0.9a_2$	$34.59(a_1 - 1.04a_2)^2$

an S-wave term, proportional to the form-factor $A_1(q^2)$:

$$\varepsilon_1 \cdot \varepsilon_2 \tag{9.2}$$

The second is a P-wave term, proportional to the form-factor $V(q^2)$:

$$\epsilon_{\alpha\beta\gamma\delta} P^\alpha q^\beta \varepsilon_1^\gamma \varepsilon_2^\delta \tag{9.3}$$

The third is the longitudinal component of a D-wave term, proportional to the form-factor $A_2(q^2)$:

$$(\varepsilon_1 \cdot q)(\varepsilon_2 \cdot q) \tag{9.4}$$

The breakdown of the BSW predictions for $\overline{K}^*\rho$ for these three terms is shown in Table 9.13. We see that in the BSW model, the S-wave term is dominant, in agreement with our observation in $D^+ \to \overline{K}^{*0}\rho^+$ decays. However, it is notable that the decay mode $\overline{K}^{*0}\rho^0$ is transversely polarized, and thus is not a pure S-wave in the L/S basis, but rather a combination of S and D-wave. A large D-wave contribution would not be consistent with the factorization hypothesis.

In our study of polarization in $D^+ \to \overline{K}^{*0}\rho^+$ decays, we found that the data is well described by an S-wave amplitude as in equation (9.2). Limits were set on P-wave and longitudinal D-wave amplitudes. With these results, and *assuming*

factorization, we can place the following constraints on the form-factors:

$$\begin{aligned} 7.18a_1A_1(0)_{D\to\overline{K}^*} + 8.38a_2A_1(0)_{D\to\rho} &= 2.4 \pm 0.4 \\ 1.06a_1V(0)_{D\to\overline{K}^*} + 1.40a_2V(0)_{D\to\rho} &< 0.7 \\ 0.84a_1A_2(0)_{D\to\overline{K}^*} + 1.05a_2A_2(0)_{D\to\rho} &< 0.8 \end{aligned} \tag{9.5}$$

Using $a_1 = 1.2$ and $a_2 = -0.5$ and the E691 values for the $D \to \overline{K}^*$ form-factors, we obtain:

$$\begin{aligned} A_1(0)_{D\to\rho} &= 0.46 \pm 0.17 \\ V(0)_{D\to\rho} &< 3.7 \\ A_2(0)_{D\to\rho} &< 2.4. \end{aligned} \tag{9.6}$$

9.4 Conclusions.

We have measured the resonant substructure of four $D \to \overline{K}\pi\pi\pi$ final states. We have found that these final states are dominated by two new classes of two-body decay modes, VV and PA. We have measured branching ratios for $\overline{K}a_1$, $\overline{K}^*\rho$, $\overline{K}_1(1270)\pi$, and $\overline{K}_1(1400)\pi$ decay modes. For the $\overline{K}a_1$ and $\overline{K}^*\rho$ decay modes, we have measured all three isospin combinations. This has allowed us to determine the effects of isospin phase shifts on the branching ratios and eliminate this source of ambiguity when comparing with the model of Bauer, Stech, and Wirbel. The branching ratios for the $\overline{K}a_1$ modes are somewhat larger than the predictions, while the branching ratios for the $\overline{K}^*\rho$ decay modes are a factor of three smaller than predicted.

We have doubled the number of measured branching ratios for Cabibbo allowed D^+ decays. We have extended, from one third to two thirds, the fraction of the hadronic widths of the D mesons accounted for by two-body decays. It was shown

in chapter 1 that the widths for PP and PV decay modes of the D^0 and D^+ are proportional to the total hadronic widths of the D^0 and D^+. We find the same is true for $\overline{K}a_1$ and $\overline{K}^*\rho$ decays. We find that the widths for $\overline{K}_1(1270)\pi$ and $\overline{K}_1(1400)\pi$ also are consistent with being proportional to the total hadronic widths, although we have not measured all three isospin combinations. Thus, we confirm the hypothesis that an understanding of the lifetime difference of the charm mesons depends on an understanding of two-body decays.

We have obtained detailed information on helicity distributions in $\overline{K}^*\rho$ decays. In agreement with the BSW model, we find that the S-wave term is dominant for $D^+ \rightarrow \overline{K}^{*0}\rho^+$ decays. However, for $D^0 \rightarrow \overline{K}^{*0}\rho^0$ decays, we find a significant D-wave component, in contradiction with the factorization approach. However, in D^0 decays, there are possibly large effects from final state interactions and weak annihilation. Assuming factorization, and using the results on $D^+ \rightarrow \overline{K}^{*0}\rho^+$ decays, we have placed constraints on $D \rightarrow \overline{K}^*$ and $D \rightarrow \rho$ form-factors.

A recent analysis by the E691 collaboration has measured $D \rightarrow \overline{K}^*$ form-factors for the decay $D^+ \rightarrow \overline{K}^{*0}e^+\nu$. The results are not in agreement with theoretical models. If factorization is valid, these form-factors also apply to $D^0 \rightarrow K^{*-}\rho^+$ decays. The BSW predictions for $\overline{K}^*\rho$ decays are three times larger than the branching ratios measured in this thesis. If we substitute the form-factors measured by E691 into the BSW model and assume that the $D \rightarrow \overline{K}^*$ and $D \rightarrow \rho$ form-factors are equal, we obtain good agreement with our measured values. Thus, our results for the branching ratios of the $D \rightarrow \overline{K}^*\rho$ decay modes, compared with results for semileptonic decays, indicate that factorization is a good approximation within experimental errors and that the main source of theoretical uncertainty is in the predictions of form-factors.

References

1. D.G. Hitlin, *Proc. 1987 Int. Sym. on Lepton and Photon Interactions at High Energies, Hamburg, 27-31 July, 1987.* Eds. W. Bartel and R. Ruckl. (North-Holland, 1988) p. 179.
2. P.E. Karchin, To appear in *Proc. 1988 Int. Sym. on Lepton and Photon Interactions at High Energies.*
3. R.H. Schindler *et al.*, Phys. Rev. **D24**, 78 (1981).
4. D.J. Summers *et al.*, Phys. Rev. Lett. **52**, 410 (1984).
5. J. Adler *et al.*, Phys. Lett. **196B**, 107 (1987).
6. J.C. Anjos *et al.*, Phys. Rev. Lett. **60**, 897 (1988).
7. G.P. Yost *et al.* (Particle Data Group), Phys. Lett. **204B**, 1 (1988).
8. Z. Bai *et al.*, SLAC-PUB-5191, 1990.
9. R.M. Baltrusaitis *et al.*, Phys. Rev. Lett. **56**, 2140 (1986);
10. J. Adler *et al.*, Phys. Rev. Lett. **60**, 89 (1988);
11. J. Hauser, Ph.D. thesis, California Institute of Technology, 1985 (unpublished).

12. For a review, see: N. Isgur, *Heavy Quark Physics,* edited by P.S. Drell and D.L. Rubin (American Institute of Physics, New York, 1989).

13. B. Grinstein, N. Isgur, D. Scora, and M.B. Wise, Phys. Rev. D **39** 799, (1989).

14. M. Bauer, B. Stech and M Wirbel, Z. Phys. C **29** 637, (1985).

15. F. J. Gilman and R. L. Singleton, Phys. Rev. D **41** 142, (1990).

16. J. Adler *et al.*, Phys. Rev. Lett. **62**, 1821 (1989).

17. J.C. Anjos *et al.*, Phys. Rev. Lett. **62**, 1587 (1989).

18. J. M. Izen, SLAC-PUB-4573, 1988 (unpublished).

19. J.C. Anjos *et al.*, Phys. Rev. Lett. **62**, 722 (1989).

20. R. Morrison, Presented at Aspen Center for Physics, January 16, 1990.

21. R. Ruckl, *Habilitationsschrift*, Universitat Munchen, 1984 (unpublished).

22. For a review, see M.A. Shifman, Int. J. Mod. Phys. A **3**, 2769 (1988).

23. M. Bauer, B. Stech and M. Wirbel, Z. Phys. C **34**, 103 (1987). Revised values of $a_1 = 1.2$ and $a_2 = -0.5$ are taken from B. Stech, preprint HD-THEP-87-18, 1987 (unpublished). The prediction for $B(D^0 \to K^- a_1^+)$ is from a private communication with B. Stech.

24. A.J. Buras, J.M. Gerard and R. Ruckl, Nucl. Phys. **B262**, 204 (1985).

25. D. Hitlin, private communication.

26. B.Yu. Blok and M.A. Shifman, Yad. Fiz. **45**, 841 (1987) [Sov. J. Nucl. Phys. **45**, 522 (1987)].

27. J.C. Anjos *et al.*, Phys. Rev. Lett. **62**, 125 (1989).

28. We adopt the convention that reference to a state implies reference to its charge conjugate.

29. D. Bernstein *et al.*, Nucl. Instrum. Methods **226**, 301 (1984).

30. J. Roehrig *et al.*, Nucl. Instrum. Methods **226**, 319 (1984).

31. J.S. Brown *et al.*, Nucl. Instrum. Methods **221**, 503 (1984).

32. W. Toki *et al.*, Nucl. Instrum. Methods **219**, 479 (1984).

33. R. Fabrizio *et al.*, Nucl. Instrum. Methods **227**, 220 (1984).

34. J.J. Thaler *et al.*, IEEE Trans. Nucl. Sci. **NS-30**, 236 (1983).

35. J.J. Becker *et al.*, Nucl. Instrum. Methods **235**, 502 (1985).

36. R.M. Baltrusaitis *et al.*, Phys. Rev. Lett. **56**, 2140 (1986);

37. J. Adler *et al.*, Phys. Rev. Lett. **60**, 89 (1988);

38. G. Gladding, private communication.

39. J. C. Anjos *et al.*, Phys. Lett. B, **223**, 267 (1989).

40. F. James and M. Roos, CERN Internal Report D506 (1977); F. James and M. Roos, Computer Phys. Comm. **10**, 343 (1975).

41. To obtain the error matrix, we use a corrected version of the subroutine EMATX from W. Lockman.

42. H. M. Pilkuhn, *Relativistic Particle Physics*, (Springer-Verlag, New York, 1979) p. 174.

43. J. D. Richman, Ph.D. thesis, California Institute of Technology, 1985 (unpublished).

44. F. Halzen and A. D. Martin, *Quarks and Leptons*, (John Wiley and Sons, New York, 1984) p. 139.

45. S. Gasiorowicz, *Elementary Particle Physics*, (John Wiley and Sons, New York, 1966) p. 432.

46. J.C. Anjos *et al.*, Phys. Rev. Lett. **62**, 722 (1989).

47. J. D. Jackson, Nuovo Cimento Vol. XXXIV, N. 6, 1645 (1964).

48. Blatt and Weisskopf, *Theoretical Nuclear Physics*, (Wiley, New York, 1952) p. 361.

49. M. G. Bowler, Phys. Lett. B, **182**, 400 (1986).

50. M. G. Bowler, Phys. Lett. B, **209**, 99 (1988).

51. M. Piccolo *et al.*, Phys. Lett. **70B**, 260 (1977).

52. R. Bailey *et al.*, Phys. Lett. **132B**, 237 (1983).

53. P. Kim, Ph.D. thesis, University of Toronto, 1987 (unpublished).

54. J.C. Anjos *et al.*, contributed paper, International Conference on Energy Physics, Munich, 1988.

55. Branching ratios were calculated using $B(D^0 \rightarrow K^-\pi^+\pi^+\pi^-) = .091 \pm .008 \pm .008$ and $B(D^+ \rightarrow \overline{K}^0\pi^+\pi^+\pi^-) = .066 \pm .015 \pm .015$ from ref 37 and the branching ratios of the intermediate resonances to the final state being studied.

56. A. Mincer, Mark III memo, 7/17/1989 (unpublished).

57. W.S. Lockman, Santa Cruz Institute for Particle Physics preprint SCIPP 89/08, p. 59.

58. J. Adler *et al.*, SLAC-PUB-5130 (submitted to Phys. Rev. Lett.).